BERGISCHE
UNIVERSITÄT
WUPPERTAL

Bergische Universität Wuppertal
Fakultät 4 - Mathematik und
Naturwissenschaften

Faint signatures in IceCube

Dissertation zur Erlangung des Doktorgrades
doctor rerum naturalium
(Dr. rer. nat.)

Der Fachgruppe Physik vorgelegt von
Timo Stürwald
im November 2024

Gutachter:

Herr Prof. Dr. Klaus Helbing, Bergische Universität Wuppertal

Frau Dr. Anna Pollmann, Universität Chiba

Abstract

Free fractionally charged particles are predicted in several extensions of the Standard Model of particle physics. They could have been produced in the early universe, in violent astrophysical processes or as a result of cosmic ray interactions in the upper atmosphere. Multiple experiments have searched for such particles with no evidence thus far.

The IceCube Neutrino Observatory is a Cherenkov detector instrumenting a cubic kilometer of deep antarctic ice, suitable to search for particles carrying a fraction of the elementary charge. A previous IceCube analysis has shown a reduced trigger efficiency for particles with a charge of e/3 compared to higher analyzed charges. Due to the quadratic dependence of photon production processes on the charge, significantly less photons are emitted with a decreasing charge, resulting in faint tracks as a characteristic signature for these particles. The Faint Particle Trigger was developed to enhance the detection efficiency for faint signatures. It incorporates single isolated hits in the trigger decision, which are not used by the standard triggers that work on correlated hit pairs. The FPT was successfully deployed at South Pole and improves significantly the trigger efficiency for a broad range of charges, while increasing the event rate by a factor 1.004. This includes a relative improvement by a factor of 1.55 for a charge of e/3, compared to the standard triggers.

The consecutively developed Faint Particle Filter further reduces the trigger rate of 100 Hz to approximately 8 Hz while keeping 85% of the triggered events for a charge of e/3. Implications by the Faint Particle Trigger and Filter are discussed.

Zusammenfassung

Freie Teilchen mit gebrochenzahliger Ladung werden in mehreren Erweiterungen des Standardmodells der Teilchenphysik vorhergesagt. Sie könnten im frühen Universum, in hochenergetischen astrophysikalischen Ereignissen oder als Produkte von Wechselwirkungen kosmischer Strahlung in der oberen Atmosphäre entstanden sein. Viele verschiedene Experimente haben nach diesen Teilchen gesucht und bisher wurde keins gefunden.
Das IceCube Neutrino Observatorium ist ein Cherenkov-Licht Detektor, der aus mehr als 5000 optischen Modulen besteht, die im tiefen antarktischen Eis eingefroren sind. Der Detektor kann Teilchen mit gebrochenzahliger Ladung nachweisen. Eine frühere Analyse, die nach Teilchen mit einer Ladung zwischen $\frac{1}{3}e$ bis $\frac{2}{3}e$ unter der Annahme eines isotropen Flusses in der Nähe des Detektors gesucht hat, hat eine signifikante Reduzierung der Triggereffizienz für Teilchen mit einer Ladung von $\frac{1}{3}e$ festgestellt. Der Grund dafür ist, dass die Standardtrigger nur korrelierte Trefferpaare (HLC Treffer) analysieren und nicht isolierte Einzeltreffer (SLC Treffer). Aufgrund der quadratischen Abhängigkeit der produzierten Photonen zur Ladung des Teilchens produzieren Teilchen mit einer Ladung von $\frac{1}{3}e$ dominant SLC Treffer. Deshalb wurde der "Faint Particle Trigger" unter der Verwendung von Signalevents mit mindestens zehn Signaltreffern entwickelt. Dieser analysiert für seine Entscheidung auch SLC Treffer. Vier Schnittvariablen wurden entwickelt, die Detektorrauschen und zu helle Signaturen entfernen. Dies führt zu einer relativen Verbesserung der Triggereffizien bei einer Ladung von $\frac{1}{3}e$ von 1.55. Die Ereignisrate in IceCube wird dabei um einen Faktor von 1.004 erhöht und der Trigger hat eine Rate von ungefähr 100 Hz.
Der "Faint Particle Trigger" wurde am 28. November 2023 erfolgreich am IceCube Experiment in Betrieb genommen. Die Triggerrate besteht aus einigen Hertz an Detektorrauschen und wird von atmosphärischen Myonen dominiert. Um die Rate weiter zu senken, wurde

der "Faint Particle Filter" entwickelt, der die Triggerrate auf ungefähr 8 Hz reduziert und 85% der getriggerten Ereignisse von Teilchen mit einer Ladung von $\frac{1}{3}e$ durchlässt.
Die relativen Verbesserungen auf Trigger- und Filterlevel wurden für Simulationen von Ladungen, bis zu der tiefesten simulierten Ladung von $\frac{1}{33}e$, analysiert. Dafür wurden neue Ereignisse simuliert und auch die mit weniger als zehn Signaltreffern analysiert. Die Resultate zeigen das IceCube zwischen einer Ladung von $\frac{1}{5}e$ und $\frac{1}{10}e$ signifikant an Triggereffizienz verliert. Des Weiteren zeigt ein direkter Vergleich zur vorherigen Analyse relative Verbesserung von 1.42 und 1.82 auf Trigger- und Filterlevel für eine Ladung von $\frac{1}{3}e$. Der selbe Vergleich wurde für ein anisotropes Szenario durchgeführt. In diesem Szenario wird jedes simulierte Ereignis mit einer Überlebenswahrscheinlichkeit gewichtet, die von seiner Masse, Energie und dem durch die Erde zurückgelegten Weg abhängt.
Zuletzt wurden erwartete Ereignisraten für ein bestimmtes Modell berechnet, das Flüsse von Teilchen mit gebrochenzahliger Ladung prognostiziert. Diese ersten Berechnungen unterliegen einer großen Unsicherheit und deuten darauf hin, dass die kleinste Ladung, für die in IceCube analysierbare Anzahlen an Ereignissen zu erwarten sind, eine Ladung zwischen $\frac{1}{5}e$ und oberhalb von $\frac{1}{10}e$ ist.

Contents

Abstract **i**

Zusammenfassung **ii**

List of Tables **ix**

List of Figures **xiv**

List of Acronyms **xv**

1 Introduction **1**

2 Theory **3**

2.1 The standard model of particle physics 4

2.1.1 Bosons 4

2.1.2 Fermions 5

2.1.3 Interactions 5

2.2 Beyond the standard model 6

2.3 Fractionally charged particles 7

2.3.1 Summary of searches 8

2.4 Millicharged particles from the atmosphere 9

2.5 Light production processes 11

2.5.1 Cherenkov effect 11

2.5.2 Ionization 12

2.5.3 Pair production 13

2.5.4 Photonuclear interaction . . . 13
2.5.5 Bremsstrahlung . . . 13
2.5.6 Energy losses for fractionally charged particles . . . 14
2.6 Survival probability for fractionally charged particles . . . 16
2.7 Cosmic rays . . . 20
2.7.1 Extensive Air showers . . . 21

3 The IceCube Neutrino Observatory 23
3.1 The Antarctic ice . . . 24
3.2 IceCube . . . 24
3.3 DeepCore . . . 25
3.4 The Digital Optical Module . . . 25
3.4.1 Dark Noise . . . 26
3.5 Triggering . . . 27
3.6 Transmission and filtering . . . 29
3.6.1 Transmission and filtering until 2023 . . . 29
3.6.2 Transmission and filtering from 2023 on . . . 29
3.7 Neutrino signatures . . . 30

4 Simulation 33
4.1 Signal simulation . . . 33
4.1.1 Event generation . . . 33
4.1.2 Event propagation . . . 33
4.1.3 Detector simulation . . . 34
4.1.4 Processing and Filtering . . . 35
4.1.5 Effective area . . . 35
4.2 FCP properties . . . 37

5 The Faint Particle Trigger 41
5.1 Faint Particle Trigger DC version . . . 42
5.1.1 Sliding time window . . . 42
5.1.2 Cut 1: Number of hits . . . 44

5.1.3 Cut 2: Number of Doubles . . . 45
5.1.4 Cut 3: Directional consistency of Doubles . . . 47
5.1.5 Cut 4: SLC fraction . . . 51
5.1.6 Variation of the time window separation parameter . . . 53
5.1.7 Summary of cuts and results . . . 53
5.2 Faint Particle trigger full detector and IC79 versions . . . 55
5.2.1 Input hit rate reduction . . . 55
5.2.2 Isolated DOMs, all hits and IC79 versions . . . 57
5.3 Comparison of all Faint Particle Trigger versions . . . 59

6 Tests and deployment of the Faint Particle Trigger 61
6.1 The South Pole Test System . . . 61
6.2 Test runs at the South Pole System . . . 63
6.3 The Faint Particle Trigger rate trend . . . 67

7 The Faint Particle Filter 69
7.1 The Faint Particle Filter algorithm . . . 70
7.1.1 Input to the Faint Particle Filter . . . 70
7.1.2 The only FPT branch . . . 71
7.1.3 Multiple triggers/DC branch . . . 72
7.1.4 NChannel vs. #HLC Cut in DC . . . 74
7.1.5 NChannel vs. #HLC cut in IC . . . 75
7.1.6 IceHive and CoincSuite . . . 76
7.1.7 Cleaning and reconstruction . . . 79
7.2 Faint Particle Filter results . . . 80
7.3 Faint Particle Filter test runs . . . 81

8 Improvements by the Faint Particle Trigger and Filter 84
8.1 Simulation sets and comparison levels . . . 84
8.1.1 Simulation sets . . . 84
8.1.2 Trigger level . . . 85
8.1.3 Online Filter level . . . 85

8.1.4 Filter level 86
8.2 Trigger efficiency comparison for various masses 87
8.3 Effective area comparison 89
8.3.1 Effective area in the isotropic scenario 89
8.3.2 Effect of the survival probability on the zenith distribution 91
8.3.3 Effective area for the non-isotropic scenario 92
8.4 Expected event rates for the MCP model 94

9 Conclusion and Outlook **97**

A Appendix A **99**

B Appendix B **107**

C Appendix C **111**

D Appendix D **117**

Bibliography **132**

Acknowledgements **133**

List of Tables

5.1 Relative improvements for neutrino simulation 54
5.2 Full detector version (isolated DOMs) parameters 57
5.3 Comparison of FPT versions 60

6.1 FPT trigger parameters 64
6.2 Test runs and FRT data FPT rates 64

7.1 Relative improvements for GeV neutrino simulation 80

8.1 Simulation parameter 85

A.1 FPT full detector version (all hits) parameters 104
A.2 FPT IC79 version parameters 105

List of Figures

2.1 The Standard Model of particle physics 3
2.2 Upper flux limits for FCP for multiple experiments 8
2.3 Schematic view of a millicharged particle produced in the atmosphere. . . 9
2.4 Atmospheric flux prediction for millicharged particles 10
2.5 Schematic view of the Cherenkov effect 12
2.6 Feynman diagrams for energy losses 14
2.7 Energy loss processes comparison for a fixed FCP mass 15
2.8 Energy loss processes comparison for a fixed FCP charge 16
2.9 Survival probability for a FCP with a mass of 1 TeV and ε of 1/3 18
2.10 50% survival probability contours for FCPs with $\varepsilon = 1/3$ 18
2.11 50% survival probability contours for FCPs with m= 10 GeV 19
2.12 The Cosmic Ray energy spectrum 21
2.13 Schematic view of an extensive air shower 22

3.1 The IceCube Neutrino Observatroy 23
3.2 Schematic top and side view of IceCube and DC 24
3.3 Schematic view of a DOM 25
3.4 Noise components 27
3.5 IceCube filtering and transmission 29
3.6 Schematic view of charged current neutrino topologies 31

4.1 Schematic view of the FCP event generation 34
4.2 Simulated FCP 38

4.3 SLC fraction for FCP 39

5.1 Faint Particle Trigger concept 41
5.2 Sliding time window 42
5.3 The number of hits in the time window 44
5.4 Hit pair velocity distribution 46
5.5 Number of Doubles in the time window 47
5.6 Directional clustering of Doubles for one example event 48
5.7 Bin sizes for directional clustering of Doubles 49
5.8 Maximum zenith vs. azimuth bin count for FCP and Detector Noise . . . 50
5.9 SLC fraction distribution for FCP and FRT data 51
5.10 SLC fraction cut optimization 52
5.11 Variation of the time window separation s 53
5.12 Summary of Cuts 54
5.13 Isolated DOMs method 57
5.14 Summary of cuts for the FD (all hits) version 60

6.1 SLC fraction comparison (FRT data and SPTS) 62
6.2 CPU utilization of the trigger system 63
6.3 #Hits and SLC fraction for test run data. 66
6.4 Trigger length for test run data 67
6.5 FPT rate for the first 11 months of operation 68

7.1 Faint Particle Filter overview 69
7.2 Simulated muon triggered by the FPT 70
7.3 Only FPT branch rate after NoiseEngine 73
7.4 Only FPT branch FCP after NoiseEngine 73
7.5 NChannel vs. #HLC cut for FCP 74
7.6 NChannel vs. #HLC cut in DC 75
7.7 NChannel vs. #HLC cut in IC 76
7.8 Time differences of mixed FCP and muon simulation 77
7.9 Performance comparison of TriggerSplitter and IceHive 78

7.10 Schematic view of the reconstruction chain 79
7.11 Faint Particle Filter results 81
7.12 FPF variable distributions for test data 83

8.1 Trigger efficiency comparison for various masses and charges 87
8.2 Averaged effective area for the isotropic scenario 89
8.3 Relative changes for the isotropic scenario 91
8.4 Effect of the survival probability on the cosine zenith distribution 92
8.5 Relative improvements for the non-isotropic scenario 93
8.6 Relative changes for the non-isotropic scenario 94
8.7 Effective area and expected event rate for ε of 1/5 96

A.1 Δt for Detector Noise hit pairs 99
A.2 Δd for Detector Noise hit pairs 100
A.3 Bin size of 50° for directional clustering of Doubles 101
A.4 Maximum zenith vs. azimuth bin count for FRT data 101
A.5 FPT full detector version (isolated DOMs) cut variables 102
A.6 SLC fraction cut optimization full detector (isolated DOMs) 103
A.7 FPT full detector version (all hits) cut variables 104
A.8 FPT IC79 cut variables 105
A.9 Summary of cuts for the IC79 version 106

B.1 Hit pair velocity and Doubles comparison (FRT and SPTS) 108
B.2 Azimuth and Zenith comparison (FRT and SPTS) 109
B.3 Trigger variables for test run data 110

C.1 FCP mixed with a high energy muon 111
C.2 Only FPT branch ν_e signal efficiency after NoiseEngine 112
C.3 FPT branch $\nu_{e,A}$ and $\nu_{e,C}$ signal efficiency after NoiseEngine 113
C.4 FPT branch $\nu_{\mu,A}$ and $\nu_{\mu,B}$signal efficiency after NoiseEngine 114
C.5 FPT branch $\nu_{\tau,A}$ and $\nu_{\tau,B}$signal efficiency after NoiseEngine 115
C.6 FPF zenith and azimuth distributions for test data 116

D.1 Averaged effective area for the isotropic scenario including the FPF . . . 117
D.2 Relative improvements for the isotropic scenario by the FPF 118
D.3 Averaged effective area for the non-isotropic scenario including the FPF . 118
D.4 Relative improvement for the non-isotropic scenario by the FPF 119
D.5 Effect of the survival probability on the zenith distribution 120
D.6 Effective area and expected event rate for ε of 1/3 121
D.7 Effective area and expected event rate for ε of 1/10 122

List of Acronyms

ADC Analog to Digital Converter

ATWD Analog Transient Waveform Digitizer

BSM Beyond the Standard Model

CC Charged Current

CR Cosmic Ray

DAQ Data Acquisition

DC DeepCore

DOM Digital Optical Module

FADC Fast Analog to Digital Converter

FCP Fractionally Charged Particle

FPF Faint Particle Filter

FPT Faint Particle Trigger

FRT Fixed Rate Trigger

GUT Grand Unified Theory

HLC Hard Local Coincidence

ICL IceCube Lab

LED Light Emitting Diode

MCP Millicharged Particle

Msps Mega-samples per second

NC Neutral Current

PnF online Processing and Filtering

PMT Photomultiplier Tube

PROPOSAL PROpagator with optimal Precision and Optimized Speed for All Leptons

RTV Room Temperature Vulcanizing

SMT Simple Multiplicity Trigger

SPS South Pole System

SPTS South Pole Test System

SM Standard Model

SLC Soft Local Coincidence

1

Introduction

Within the Standard Model (SM) of particle physics quarks, carrying a fraction of the elementary charge, always appear in composite objects carrying an integer charge, due to color confinement. Free Fractionally Charged Particles (FCPs) only appear in several extensions of the SM, with different charge predictions. The theoretical motivation, previous searches and properties of such particles are summarized in chapter 2.

The IceCube detector is a cubic kilometer neutrino detector consisting of more than 5000 Digital Optical Modules (DOMs) in the deep antarctic ice. The detector and corresponding simulation framework used to simulate FCPs are explained in chapter 3 and chapter 4.

A search for particles with charges between $\frac{1}{3}e$ to $\frac{2}{3}e$ in a broad mass range, assuming an isotropic flux of FCP near the detector, was previously conducted with IceCube. It was found that the trigger efficiency significantly decreases for charges of $\frac{1}{3}e$, compared to higher analyzed charges. This shortcoming is explainable by the fact that the IceCube standard triggers base their decisions on correlated hit pairs, so called Hard Local Coincidence (HLC) hits. Due to the quadratic dependence of the charge of the non-negligible light production processes, the lower charged particles dominantly produce isolated hits, so called Soft Local Coincidence (SLC) hits.
This initiated the development of the new Faint Particle Trigger (FPT), using simulation of high quality[1] FCPs with a charge of $\frac{1}{3}e$, that also analyzes the SLC hits. Four cut variables were constructed to remove detector noise and too bright signatures, which are discussed

[1] FCPs simulation that produce a sufficient amount of signal hits to be reconstructable

in chapter 5. The trigger analyzes all hits of the DeepCore (DC) sub-array and significantly improves the signal efficiency by a factor of 1.55. The FPT rate is approximately 100 Hz and increases the event[2] rate in IceCube by a factor of 1.004.
The test of the FPT algorithm at the South Pole Test System (SPTS) and test data runs with the IceCube detector before the final deployment at 28 November 2023 are discussed in chapter 6.

The FPT rate consists of a few Hz of noise contribution and is dominated by atmospheric muons. The rate is further reduced to approximately 8 Hz, while keeping 85% of the triggered FCP events, with the newly developed Faint Particle Filter (FPF). The FPF splits events in two branches, where the first one focuses on removing detector noise contributions in events that are dim in the entire detector. The second branch removes events that are bright in the detector and only produce a few outlier hits in DC, appearing as dim signatures to the FPT.

The improvements at trigger and filter level are discussed in chapter 8 for a broader range of simulated charges down to $\frac{1}{33}e$, using newly simulated events that do not satisfy a specific quality cut. It is found that IceCube significantly looses detection efficiency between charges of $\frac{1}{5}e$ to $\frac{1}{10}e$. A direct comparison to the previous IceCube analysis is done, resulting in relative improvements of 1.42 and 1.82 for a charge of $\frac{1}{3}e$ at trigger and filter level respectively. Furthermore, the same comparison is conducted for a non-isotropic scenario in which each event is weighted by a survival probability dependent on the mass, energy and path length traversed through the earth to reach the detector.
Lastly, a Millicharged Particle (MCP) model dependent estimation on the number of expected events in IceCube per year at trigger and filter level is calculated. These first estimates, which are subject to large uncertainties, indicate that for the analyzed charges, the lowest charge for which a sufficient amount of events is expected is $\frac{1}{5}e$.

[2] An event can consist of multiple triggers that fired close in time

2

Theory

In this chapter the SM of particle physics and extensions that include free FCP are introduced. Furthermore, the light production processes and the passage of these particles through the Earth are discussed. This is followed by the introduction to extensive air showers, initiated by Cosmic Ray (CR) interactions in the upper atmosphere.

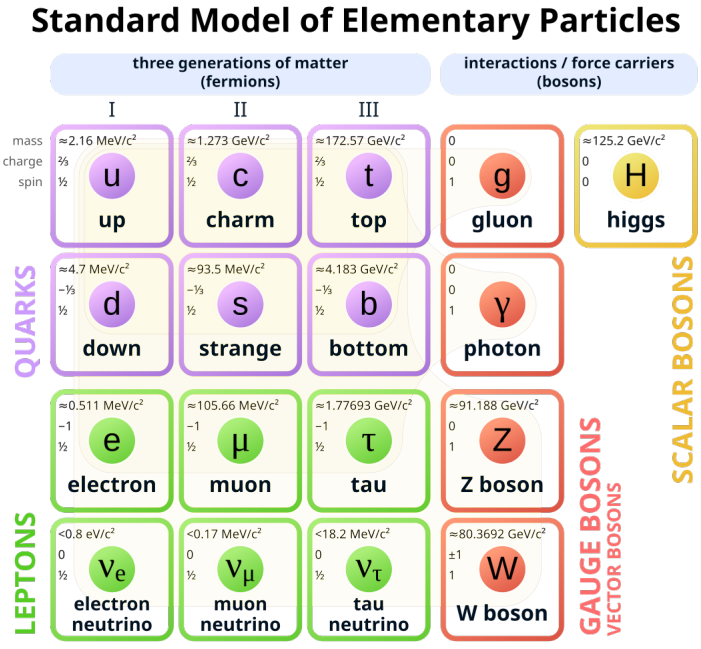

Figure 2.1: The Standard Model of particle physics
The standard model of particle physics, showing three generations of quarks and leptons, along with the fundamental bosons. Taken from [1].

2.1 The standard model of particle physics

The SM of particle physics is a Yang-Mills theory [2] developed in the latter half of the 20th century. Through an interplay of theoretical predictions and experimental findings, relativistic quantum field theories for three of the four fundamental forces were formulated. Elementary particles are categorized into fermions, which carry half-integer spin and constitute matter, and bosons, which carry integer spin and serve as force carriers, mediating interactions among fermions (see Figure 2.1). Extensive discussions and calculations can be found in the literature [3–6].

2.1.1 Bosons

The mathematical description of the SM is a gauge theory for which the Lagrangian is invariant under local symmetry transformation. Important Lie groups describing these symmetries include the U(N) and SU(N) groups, consisting of N^2 and N^2-1 generators, respectively. The standard model is a non-abelian gauge group invariant under $SU(3)_C \times SU(2)_L \times U(1)_Y$ local symmetry transformation. The local symmetries introduce in total 12 gauge bosons corresponding to the 12 generators of the gauge groups. These are 8 gluon fields from the $SU(3)_C$ group, the massless W_1, W_2, W_3 fields from the $SU(2)_L$ group and the massless B field from the $U(1)_Y$ group. Particles are excited states of the fields, which are defined at all points in spacetime.

The Brout-Englert-Higgs mechanism is a process by which particles acquire mass via spontaneous symmetry breaking and was independently found by three groups [7–9] in 1964. It predicted a massive scalar field, the Higgs boson, which was experimentally confirmed in 2012 [10].

In the 1960s, theoretical work by Sheldon Glashow, Abdus Salam, and Steven Weinberg established the unified description of electromagnetic and weak interactions through the electroweak theory. This theory predicted that after spontaneous symmetry breaking, the weak interaction would be mediated by three massive vector bosons (Z, $W^{\pm}$) and a

massless photon γ responsible for mediating the electromagnetic force [3, 11, 12].

$$\begin{pmatrix} \gamma \\ Z^0 \end{pmatrix} = \begin{pmatrix} \cos\theta_W & \sin\theta_W \\ -\sin\theta_W & \cos\theta_W \end{pmatrix} \begin{pmatrix} B \\ W_3 \end{pmatrix}$$
$$W^{\pm} = \frac{1}{\sqrt{2}}(W_1 \pm iW_2)$$

The $W^{\pm}$ are linear combinations of W_1 and W_2 fields and the photon and Z bosons linear combinations of W_3 and the B fields. θ_W is the Weinberg angle and the bosons of the weak interaction now carry the familiar masses.

2.1.2 Fermions

Fermions are described by Weyl fields with left or right-handed chirality combined in a Dirac spinor. Four of these for the up (charge of $\frac{2}{3}e$) and down quark (-$\frac{1}{3}e$) and electron (charge of e) and electron neutrino (neutral) are present in the SM. The two additional generations are copies of the original fields resulting in the (u,d) (c,s) and (t,b) quarks. Furthermore the lepton generation come in pairs resulting in (e,ν_e), (μ,ν_μ) and (τ,ν_τ). The difference between the generations are the masses of the fields. Why this is limited to three is not understood.

2.1.3 Interactions

The strong interaction, mediated by massless gluons is effective up to distances of approximately 1 fm, binding the constituents of nucleons. Only quarks are subject to the strong force. This interaction is mediated by gluons, with color charge as the conserved quantity. Color charge is carried by quarks and gluons, enabling gluon self-interactions. This results in confinement, meaning quarks always combine into color-neutral particles and cannot propagate freely. Consequently, no free fractionally charged particles appear in the SM.
The electromagnetic interaction is mediated by the massless photon, with an infinite range that decreasing distance. This interaction occurs between charged particles, which either repel or attract each other.
The weak force is responsible for flavor changing processes within the quark and lepton

families. It can be mediated in a Charged Current (CC) interaction by the charged W bosons or in a Neutral Current (NC) interaction via the neutral Z boson. Neutrinos interact solely via the weak force. Due to the large boson masses it is a short ranged force of about 10^{-18} m. This interaction is chiral, distinguishing between left- and right-handed fermions, with $W^{\pm}$ bosons only coupling exclusively to left-handed particles for reasons yet unknown.

2.2 Beyond the standard model

The SM is tested with high precision. Nevertheless, it can not explain all observed phenomena which indicate the need for Beyond the Standard Model (BSM) physics.
The SM is not compatible with the theory of general relativity and thus does not account for gravity. Furthermore, neutrinos are massless in the SM which is falsified by observed neutrino oscillations [13], which imply that at least two neutrinos have non-zero mass.
The SM also lacks a mechanism to explain the observed matter-antimatter asymmetry [14] indicating BSM physics.
The ΛCDM model is the most widely accepted cosmological model for explaining the structure and evolution of the universe. According to this model, baryonic matter constitutes only about 16% of the universe's total matter content [15], with the remainder accounted for by cold dark matter. The existence of cold dark matter is supported by measurements of galaxy rotation curves [16, 17] and gravitational lensing effects [18]. In the ΛCDM model, total energy is composed of approximately 5% baryonic matter, 26% dark matter, and 69% dark energy [19].
The unexplained quantization of charge within the SM can be addressed by Grand Unified Theory (GUT), which unify the electroweak and strong force at high energies [20]. Those theories predicting the quantization of charge imply the existence of magnetic monopoles [21], which were first predicted in a GUT [22] in 1974. Despite extensive searches [23], no magnetic monopole has been discovered so far.
The searches for FCP (discussed in section 2.3) and magnetic monopoles searches are connected, because the discovery of one could potentially exclude or limit the predictions of the other. Both searches explore the fundamental nature of charge.

2.3 Fractionally charged particles

In the SM, all charges appear as multiples of the d-quark's charge. Although quarks have fractional charges, they always combine into color-singlet composite particles with integer charges. This empirical rule of charge quantization lacks a theoretical basis within the SM. Therefore, while free fractionally charged particles are not explicitly forbidden by the theory, they do not naturally occur and are instead proposed in several extensions of the SM. Observation of such a particle would provide evidence for BSM physics.

The Georgi-Glashow model, a GUT that unifies the electroweak and strong interactions, was introduced in 1974. It organizes the SM fermions into the sum of a 5-dimensional fundamental representation and a 10-dimensional representation [24]. This model introduces 12 new bosons, effectively two types with three different flavors, which can also be charge-conjugated. As these bosons mediate interactions between quarks and leptons, they carry non-integer charges. The X has a charge of $\frac{4}{3}e$ and the Y of $\frac{1}{3}e$. This specific GUT allows proton decay, which conflicts with experimental results on the protons lifetime [25]. Extensions of this model predict particles with charges of $\frac{1}{3}e$ and $\frac{2}{3}e$ [26]. In more complex symmetry groups as SU(7) [27], SU(8) [28], SO(14) [29] and SO(18) [30] fractionally charged particles appear as well. These particles could have been produced in the early universe, in violent astrophysical events or in cosmic ray interactions in the upper atmosphere [31].

A previous IceCube analysis searched for well motivated charges of $\frac{1}{3}e$, $\frac{1}{2}e$ and $\frac{2}{3}e$, in a mass range between 10 GeV to 100 TeV, without focusing on a specific production scenario [32]. The assumptions on the potential signal are that these behave leptonically like muons, have a long lifetime and will not rapidly decay in the detector and they follow an energy spectrum with spectral index γ of 2[1].

An additional assumption was an isotropic flux near the detector, which creates tension within parts of the scanned parameter space due to the propagation through the earth of these particles. This is further discussed in section 2.6.

[1] spectrum defined as in Equation 2.4

2.3.1 Summary of searches

FCP searches have been conducted at fixed target [33], collider [34–36], and telescope experiments with no evidence for such particles [31]. The former two search for the production of FCP in collisions. The latest LHC result searching for FCP at a center of mass energy of 13 TeV in CMS data sets an upper limit of 95% confidence level for particles up to a mass of 640 GeV (60 GeV) for charges of $\frac{2}{3}e$ ($\frac{1}{3}e$) [36].

An upper limit comparison of model independent searches from telescopes can be seen in Figure 2.2. The sensitivity is quantified by an incoming flux close to the detector. Since the LSD [37], MACRO [38], and Kamiokande [39] detectors did not consider mass dependence in their analyses, their results are represented as straight lines. An unpublished MACRO result [40] is not included in this comparison. The assumptions underlying these limits are consistent with those made in the last IceCube analysis. The IceCube results showed a sensitivity that is approximately ten times stronger in parts of the parameter

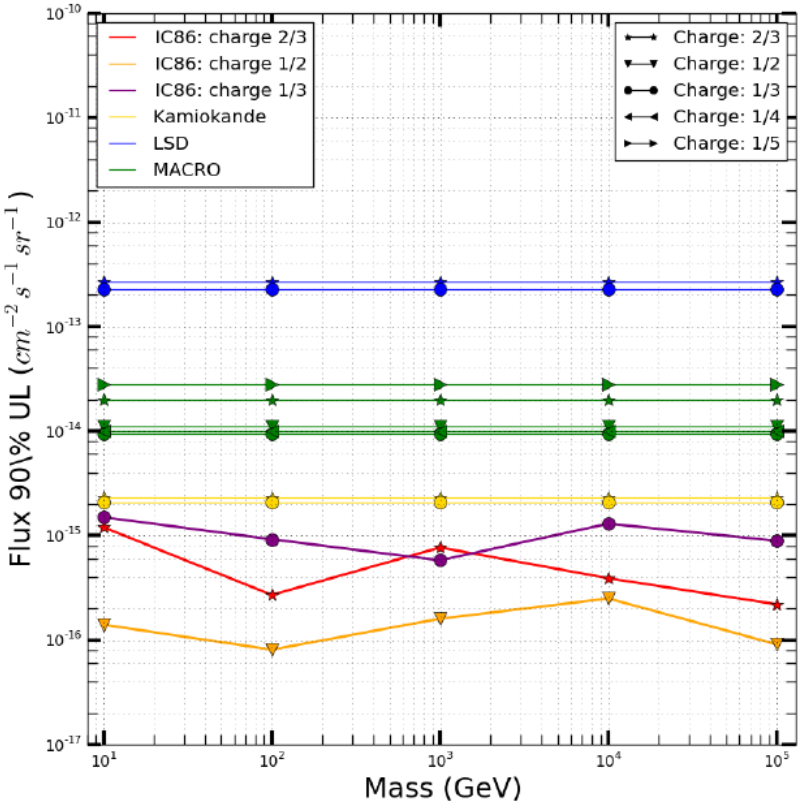

Figure 2.2: Upper flux limits for FCP for multiple experiments
Comparison of the upper limits on the FCP flux from multiple detectors. The IC86 lines correspond to the unpublished limits from [32]. Taken from [32].

space. The weakest IceCube limits were primarily observed for particles with a charge of $\frac{1}{3}e$ due to significantly lower trigger efficiency at this charge compared to higher charges [32]. The development of the FPT explained in chapter 5 is based around simulation of charges of $\frac{1}{3}e$.

2.4 Millicharged particles from the atmosphere

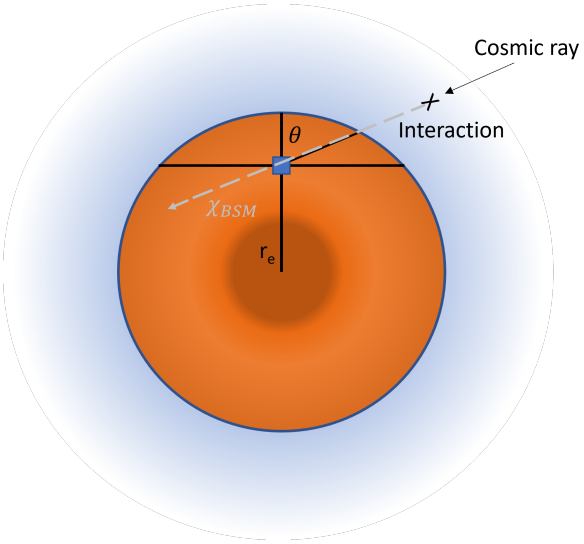

Figure 2.3: Schematic view of a millicharged particle produced in the atmosphere. *The cosmic ray interaction results in the production of heavy mesons or an intermediate virtual photon or Z. These can decay to MCP reaching the detector.*

In recent years, the production mechanisms of MCPs in the atmosphere have been studied [41–43], as visualized in Figure 2.3. These particles are referred to as MCPs, as the parameter space being explored includes charges that are much smaller than the elementary charge. The anomalous charge is typically denoted by ε, which is also used frequently throughout this thesis.

$$\varepsilon = \frac{q_{BSM}}{e}$$

MCPs are motivated by dark matter models. They are produced by the kinetic mixing of a new gauge boson satisfying a U'(1) symmetry and the photon [44, 45].
Large-volume detectors, such as IceCube, can search for multiple scattering signatures of MCPs, with IceCube's sensitivity estimated to cover masses above approximately 5 GeV [41]. However, a model-dependent search specifically for MCPs has not yet been

conducted in IceCube. Flux predictions for MCPs, as shown in Figure 2.4, indicate two primary atmospheric production processes relevant to IceCube's detectable mass range. The first process involves the decay of neutral mesons produced by high-energy CRs collisions with atmospheric nuclei (explained in section 2.7). For the parameter space relevant to IceCube, the Υ meson (m = 9.4 GeV) is the dominant contributor. MCPs must have a mass below half of the meson's mass, allowing the Υ to decay directly into a pair of MCPs [43].

The second process is the Drell-Yan production mechanism, which becomes significant for MCPs masses above 4.7 GeV, as seen in Figure 2.4. This mechanism produces MCPs pairs through the decay of a virtual γ/Z, produced by quark/anti-quark parton scattering [43].

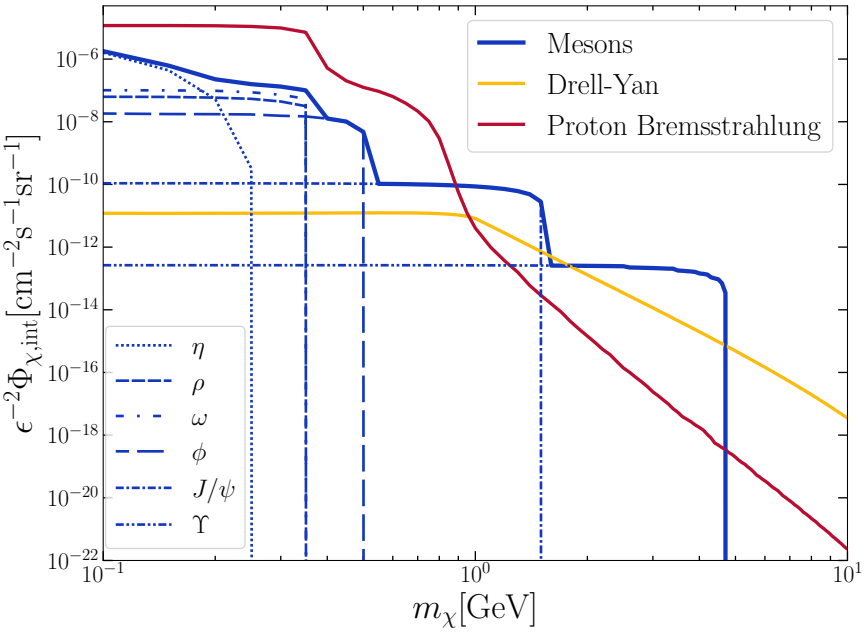

Figure 2.4: Atmospheric flux prediction for millicharged particles
Predicted integrated flux of MCP separated in different production scenarios. Taken from [43].

The uncertainty in the MCPs flux is primarily driven by the chosen cosmic-ray and hadronic interaction models used to calculate the production rates of mesons [41]. The largest source of uncertainty arises from the hadronic interaction model, leading to variations in the MCPs flux ranging from 16% to 68% [41]. These flux predictions are utilized in section 8.4 to calculate expected event rates in IceCube for different charges. The uncertainties in the flux predictions themselves are not accounted for in this thesis, which would be done in a dedicated analysis. The provided numbers are a first estimate to search for the lowest

charge that IceCube could be sensitive for under this model.

2.5 Light production processes

The particles considered in this thesis carry a fractional charge and are significantly more massive than a muon. Their detection in IceCube depends on the production of photons in ice, which occurs through various mechanisms, as explained below.
The dominant mechanism for light production is the Cherenkov effect, whereby these particles emit photons directly. Additionally, photons can be produced both directly and indirectly through processes such as ionization, pair production, photo-nuclear interactions, and bremsstrahlung. The mass dependence of these processes enters the equations in a non-trivial manner, which is analyzed further insubsection 2.5.6.

2.5.1 Cherenkov effect

The Cherenkov effect occurs when a charged particle travels through a dielectric medium at a speed greater than the speed of light in that medium, as illustrated in Figure 2.5 [46]. The speed of light in a given medium is expressed as $c_m = \frac{c_0}{n}$, where c_0 is the speed of light in vacuum and n the refractive index of the material. As the particle travels through the medium, it polarizes the material, inducing a net polarization due to its speed. When the medium de-excites, it emits coherent radiation known as Cherenkov radiation. The Cherenkov angle, which depends on the refractive index, can be derived from Huygens' principle [47], resulting in an angle of approximately $\theta \approx 41\ ^\circ$ for ice:

$$\cos(\theta) = \frac{1}{\beta n}$$

The wavelength dependent photon emission per path is given by the Frank-Tamm formula [48]:

$$\frac{d^2N}{dx\,d\lambda} = 2\alpha z^2 \frac{1}{\lambda^2}\left(1 - \frac{1}{n^2(\lambda)\cdot\beta^2}\right) \tag{2.1}$$

Here α is the fine structure constant, z the charge of the particle, λ the wavelength and β is the fraction of the speed of light in vacuum that the particle travels at. The $\frac{1}{\lambda^2}$ factor results in dominant emission in the ultraviolet UV region of the spectrum. Due to the quadratic dependence on charge, the particles considered in this thesis emit fewer Cherenkov photons than muons. Furthermore, the mass (m) of the particle does not affect the number of emitted Cherenkov photons.

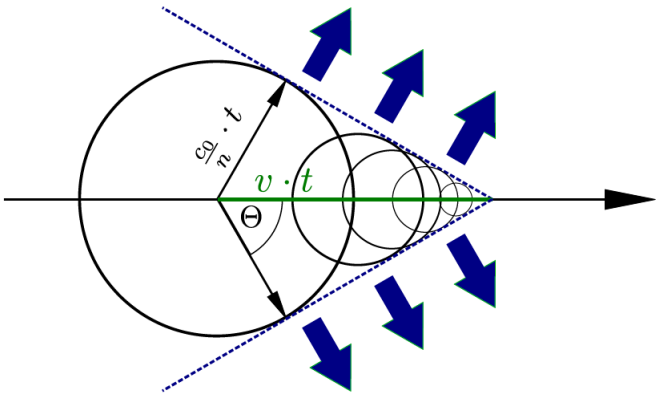

Figure 2.5: Schematic view of the Cherenkov effect
Schematic view of the Cherenkov effect, resulting in the photon emission under the Cherenkov angle θ. Taken from [49].

2.5.2 Ionization

The Bethe-Bloch equation describes the mean rate of energy loss of charged heavy particles and is shown in Equation 2.2 [15]. This is the process of charged particles passing through a medium transferring energy to an electron of the atom. This energy transfer can result in the release of a free electron, which may produce Cherenkov light if it receives a sufficient amount of energy, along with the ionization of the atom.

$$\left\langle -\frac{dE}{dx} \right\rangle = Kz^2 \frac{Z}{A} \frac{1}{\beta^2} \left[\frac{1}{2} \ln \left(\frac{2m_e c^2 \beta^2 \gamma^2 W_{\max}}{I^2} \right) - \beta^2 - \delta(\beta\gamma) \right] \tag{2.2}$$

- K: $K \approx 4\pi N_A r_e^2 m_e c^2$.

W_{max} the maximum energy transfer in a single collision, z is the charge of the incident particle, I the mean excitation energy of atoms and $\delta(\beta\gamma)$ the density correction term accounting for the polarization of the medium at high velocities.

The charge dependence is quadratically in the energy loss by ionization. This is also visible in the Feynman diagram in Figure 2.6, where the FCP has one vertex contributing to the amplitude matrix element.

2.5.3 Pair production

Pair production describes the production of an electron positron or muon anti-muon pair [2] when a virtual photon is radiated of the primary particle in the field of an atomic nucleus. The cross-section formula and further information about all parameters can be found in the corresponding paper [50]: The cross-section shows a quadratic dependence on the charge, which is also seen in the Feynman diagram in Figure 2.6.

2.5.4 Photonuclear interaction

In the process of photonuclear interaction hadrons are produced, by the inelastic scattering of a lepton with an atomic nucleus via a virtual photon exchange. This interaction is illustrated in the Feynman diagram shown in Figure 2.6. The diagram indicates a quadratic dependence of charge on the cross-section, a relationship that is also detailed in the corresponding parametrization [50].

2.5.5 Bremsstrahlung

Bremsstrahlung describes the process by which a charged particle loses energy in the electric field of another charged particle, resulting in the emission of a photon. The cross-section can be parameterized as the sum of an elastic component and two inelastic components [51]. The cross section shows a z^4 dependence and is suppressed by m^2 of the particles mass. The z^4 dependence is also visible in the corresponding Feynman diagram in Figure 2.6 where the FCP shows two vertices. For the simulation conducted in this thesis this makes bremsstrahlung a negligible light production process.

[2] The cross-section for muon pair production is estimated to be $2 \cdot 10^4$ times lower than for electron pair production [50] and the process is not considered in the simulation in this thesis.

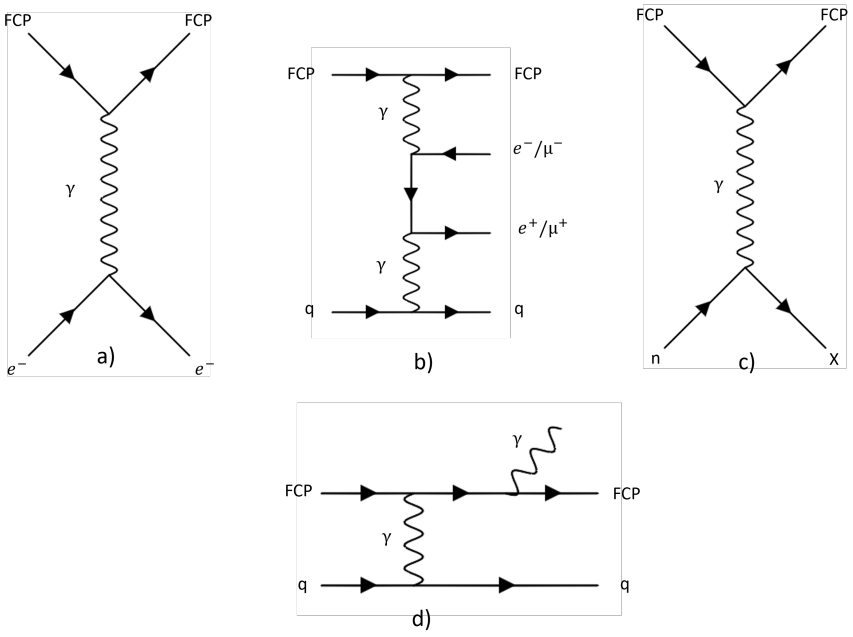

Figure 2.6: Feynman diagrams for energy losses
Shown are the Feynman diagrams for ionization (a), pair production (b), photonuclear interaction (c) and bremsstrahlung (d). X represents a hadronic remnant, q charged and n neutral particles.

2.5.6 Energy losses for fractionally charged particles

For particles with anomalous charge and higher mass compared to the muon, bremsstrahlung becomes negligible, as it scales with z^4 and is suppressed by m^2. All other secondary processes exhibit a z^2 scaling and more complex mass dependence. In the context of light production, charge remains the dominant factor.

The energy losses due to ionization, pair production, and photo-nuclear interactions in ice, for a simulated mass of 10 GeV[3] and varying charges, are shown in Figure 2.7. For sub-TeV muons, where ionization dominates, the ionization loss is approximately $0.25\,\mathrm{GeV/m}$. For a particle with charge fraction $\varepsilon = 1/3$ the energy loss is expected to decrease by an order of magnitude, which is confirmed in Figure 2.7.

Comparing ionization losses across different charges reveals the expected z^2 dependence, scaling, with the highest contribution for $\varepsilon = 2/3$. The crossover point, where pair production becomes the dominant loss mechanism in ice, occurs at $4 \cdot 10^5$ GeV for an ε of 2/3, $6 \cdot 10^5$ for an ε of 1/2 and $7 \cdot 10^5$ for an ε of 1/3. Thus, for energies exceeding roughly 10^4 times the particle's rest mass, pair production dominates energy loss. This transition

[3]Throughout the thesis all masses appear in natural units with $\hbar = c = 1$

occurs at a similar point for muons.

Photonuclear interactions become more significant than ionization for energy thresholds of 10^5 *GeV* ($\varepsilon = 2/3$), $2 \cdot 10^5$ GeV ($\varepsilon = 1/2$) and $4 \cdot 10^6$ GeV ($\varepsilon = 1/3$). However, photonuclear processes remain less important than pair production, especially for particles with lower charge. The energy losses for particles with masses of 10 GeV and 100 TeV, both with a

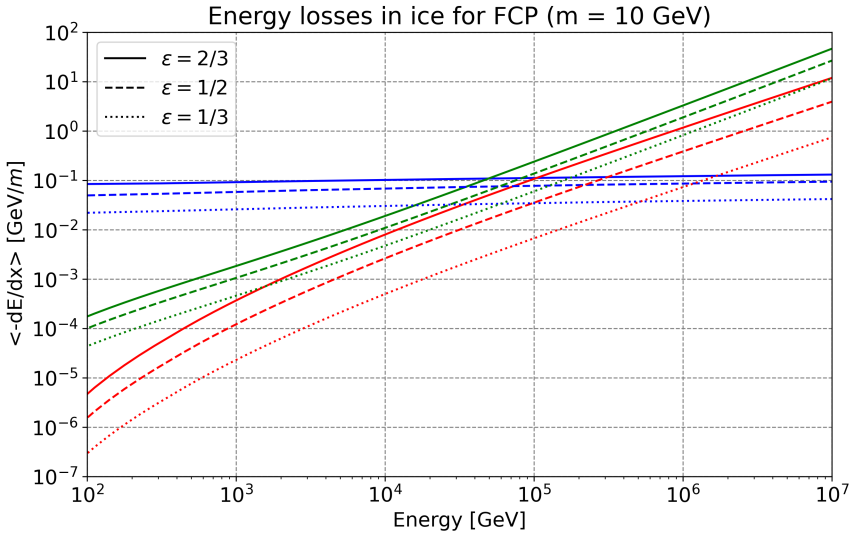

Figure 2.7: Energy loss processes comparison for a fixed FCP mass
Comparison of ionization (blue), pair production (green) and photonuclear interactions (red) for a fixed FCP mass of 10 GeV. Each contribution is shown for ε of 2/3 (solid) 1/2 (dashed) and 1/3 (dotted).

fixed charge fraction of $\varepsilon = 1/3$ are shown in Figure 2.8. While the shapes of the curves remain the same, they shift along the x-axis. The intersections of the energy loss curves occur at the same multiples of the particle's rest mass for both cases. This implies that for very massive particles at relativistic energies, secondary processes contribute less significantly to energy loss. Consequently, a 100 TeV particle moving at relativistic speeds can travel much farther than a 10 GeV particle at the same speed, leading to a more isotropic flux, as discussed in section 2.6.

It can be concluded that light emission processes from secondary interactions become dominant only at very high energies. Due to the simulated energy spectrum, these processes occur infrequently in the simulations used in this thesis (in $\approx 3\%$ of the events explained in section 5.1). While delta electrons created by ionization are more abundant ($\approx 5\%$ of the events explained in section 5.1) in the simulation, the primary mechanism for light production is the emission of photons through the Cherenkov effect, as discussed in

subsection 2.5.1. Therefore, although the photon production processes described here are accounted for, they do not drive the overall light emission.

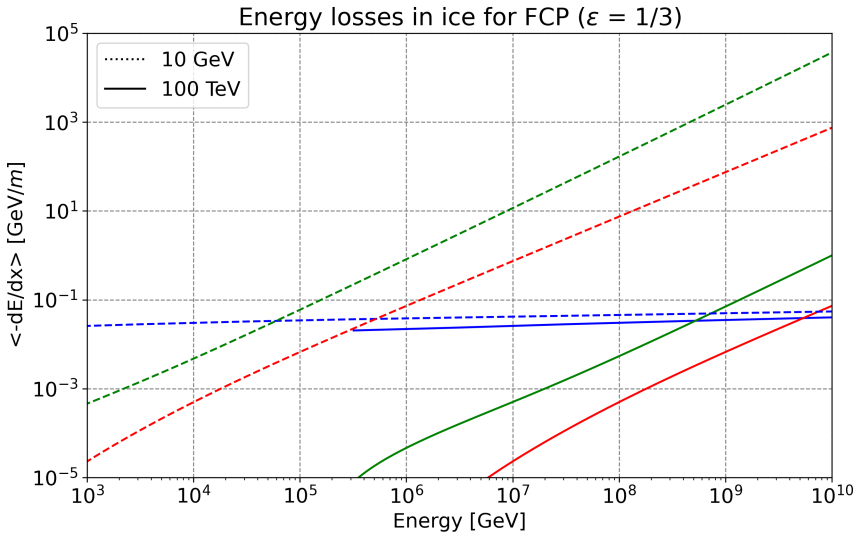

Figure 2.8: Energy loss processes comparison for a fixed FCP charge
Comparison of ionization (blue), pair production (green) and photonuclear interactions (red) for a fixed ε of 1/3. Each contribution is shown a mass of 10 GeV (dotted) and 100 TeV (solid).

2.6 Survival probability for fractionally charged particles

To account for the varying path lengths that particles traverse through the Earth, which arise from the randomized zenith angles, it is essential to consider this propagation. The distance traveled by a particle through the Earth to the center of the IceCube detector (explained in chapter 3) can be expressed as follows:

$$D = \sqrt{(R_\oplus - d)^2 \cos^2\theta + d(2R_\oplus - d)} - (R_\oplus - d)\cos\theta$$

$R_\oplus$ is earth's radius set to 6356.8 km, d the depth of the detector center set to 1950 m and θ is the zenith angle. The mean free path is calculated by:

$$b = \frac{\frac{dE}{dx}(E_i) - \frac{dE}{dx}(E_f)}{E_i - E_f}$$

$$R = \frac{1}{\rho b} \ln\left(\frac{\frac{dE}{dx}(E_i)}{\frac{dE}{dx}(E_f)}\right)$$

$\frac{dE}{dx}(E_{i,f})$ corresponds to the average energy losses at the initial and final energies after the particle has propagated to the center of the detector. ρ is the mass density of the material and is set to 0.9168 $\frac{g}{cm^3}$ corresponding to ice. The cross sections for the energy loss processes are calculated using PROpagator with optimal Precision and Optimized Speed for All Leptons (PROPOSAL) [52, 53]. In this calculation, the density does not vary with zenith angle. Due to the spectral shape of the simulated particles, high energies are suppressed in this simple model. For almost all charge-mass combinations, zenith angles above 90° are suppressed at the lower energies of the corresponding spectra. Up to a zenith angle of 90°, ice is the appropriate material description. Thus, except for a few high-energy events occurring below the horizon, the simplified model is suitable.[4]

The survival probability is then the ratio of the mean free path divided by the traversed length [41].

$$P = \exp\left(\frac{-D\cos\theta}{R(E_i, \varepsilon, E_f)}\right) \tag{2.3}$$

The survival probability is calculated for a particle that has sufficient energy to travel an additional 500 m after being propagated to the center of the detector and is above the Cherenkov threshold. A survival probability plot for the zenith angle and energy range of a FCP with a mass of 1 TeV and $\varepsilon = 1/3$ is shown in Figure 2.9. It can be observed that for all energies, the survival probability exceeds 50% above $\cos\theta = -0.125$. Below this value, the survival probability decreases rapidly due to the increasing distance the particle must travel, which can only be compensated for by higher energies. As a result, there is a large area below the horizon where no signal is expected.

Given the spectral index (2 for this mass in this thesis) of the energy spectrum, most events are concentrated within an energy range of 10^5 GeV. Consequently, the expected flux below $\cos\theta = -0.125$ is negligible, leading to a non-isotropic flux for this charge-mass combination. It is worth noting that there is some expected flux near and slightly below the horizon. This region is typically a sweet spot for analyses in IceCube searching for exotic signatures, as the dominant atmospheric muon contributions can be significantly

[4] In the future, a zenith-dependent average density that accounts for the different layers of the Earth's core crossed can be implemented.

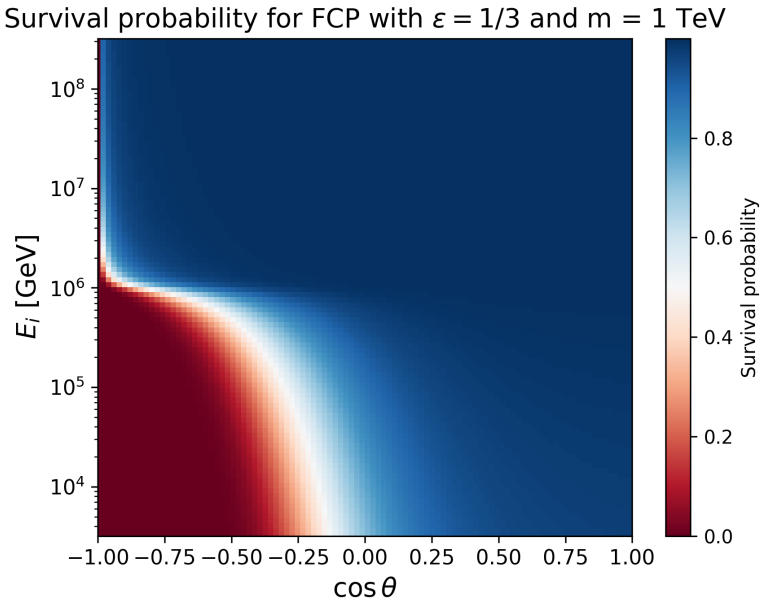

Figure 2.9: Survival probability for a FCP with a mass of 1 TeV and ε of 1/3
The survival probability is shown for a cosine zenith range and the total energy of the FCP.

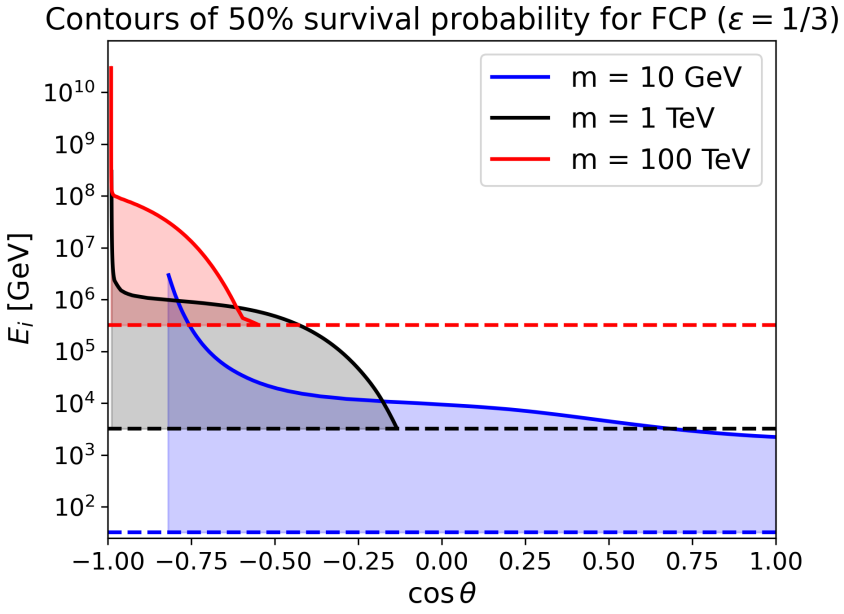

Figure 2.10: 50% survival probability contours for FCPs with $\varepsilon = 1/3$
The 50% survival probability contours are shown for masses of 10 GeV (blue), 1 TeV (black) and 100 TeV (red). The y-axis shows the initial total energy. The dashed lines show the minimum energy of the simulation sample. The energy value at which the contours end is the maximum simulated energy. For each mass the area between the minimum and maximum simulated energy corresponds to the total flux for the given energy range. Contours ending before $\cos\theta = -1$ *have lower values than 50% in the uncovered area.*

reduced due to the large ice overburden at these angles.

To analyze the influence of the FCP mass on the isotropy of the flux, the 50% survival probability contours for different masses are plotted in Figure 2.10. As shown in Figure 2.9, the approximately 50% survival probability sharply divides regions of high and low suppression. For each sample, the minimum and maximum simulated energies vary, as indicated by the dashed lines at the ends of the corresponding contours.

For the 10 GeV sample, a significant fraction of the parameter space has a survival probability of less than 50%, covering more than half of the total area for that sample. As the mass increases, this area shrinks due to the suppression of energy losses at high energies, resulting in higher survival probabilities. Therefore, an increasing mass leads to a more isotropic flux.

To analyze the influence of the charge of the FCP on the isotropy of the flux, the 50% survival probability contours for different charges are plotted in Figure 2.11.

It can be observed that as the charge decreases, the flux becomes more isotropic due to the z^2 dependence of energy loss processes. For $\varepsilon = 1/10$, no significant contributions below the horizon are expected. Combining the two effects, one can conclude that the flux is expected to be the more isotropic the heavier the particle, and the smaller the charge

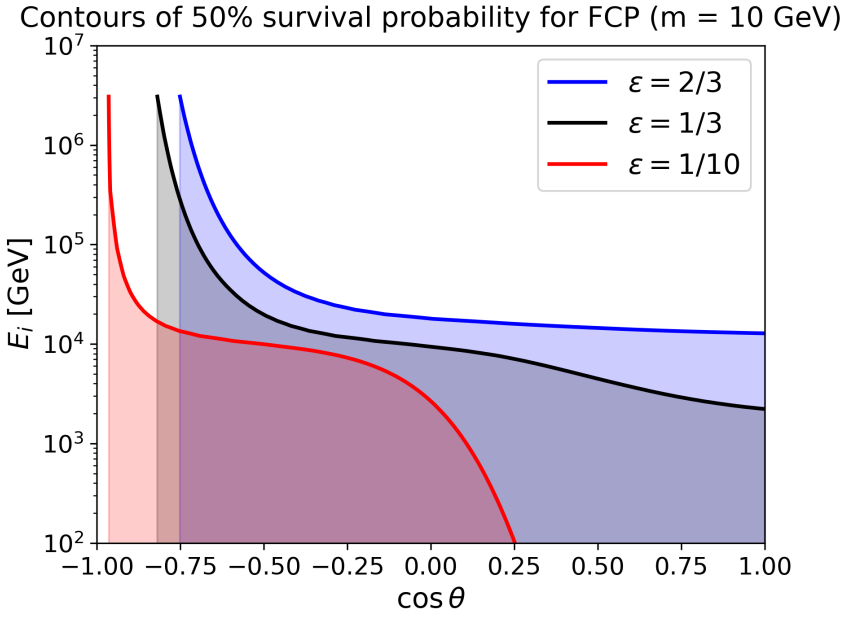

Figure 2.11: 50% survival probability contours for FCPs with m= 10 GeV
The 50% survival probability contours are shown for ε of 2/3 (blue), 1/3 (black) and 1/10 (red). The y-axis shows the initial total energy. Contours ending before $\cos\theta = -1$ *have lower values than 50% in the uncovered area.*

is. For the follow up of the previous FCP search in IceCube the most isotropic scenario corresponds to a charge mass combination of 100 TeV and ε of 1/3. For a potential MCP search no isotropic flux is expected due to the mass range of the models, which were analyzed for 5 GeV in this thesis.

2.7 Cosmic rays

Primary CRs are stable particles accelerated by astrophysical sources, consisting primarily of protons (90%) and smaller amount of heavier nuclei, electrons and positrons [54]. Secondary CRs are produced through interactions of primary CRs with interstellar gas or atmospheric nuclei. The energy spectrum of CRs follows a power law:

$$\frac{d\Phi}{dE} = E^{-\gamma} \tag{2.4}$$

with spectral index γ and ranges from GeV to EeV as shown in Figure 2.12. The spectrum exhibits distinct features where the spectral index changes. The knee is located at approximately $10^{6.6}$ GeV where the index steepens from approximately 2.7 to 3.1 [55]. This change may indicate a transition from galactic to extragalactic sources. The ankle feature appears at approximately $10^{9.6}$ GeV corresponding to a further hardening of the spectrum [56]. A steep fall-off is observed at approximately $3 \cdot 10^{10}$ GeV. At these energies the cosmic ray protons have enough energy to produce a Δ^+ resonance with the cosmic microwave background photons, limiting the propagation range and offering an explanation for the cut off.

At the energy of the knee one expects one particle per m^2 per year. Consequently, satellite experiments are not feasible for directly detecting primary CRs at these energies. Therefore, the properties of high energy primary CRs can only be inferred from secondaries produced in the atmosphere measured with large ground based detectors.

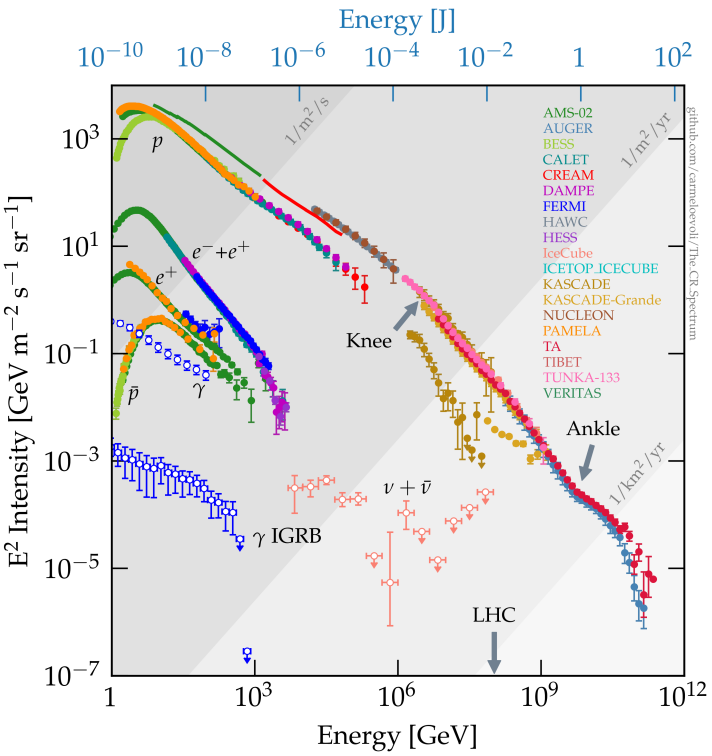

Figure 2.12: The Cosmic Ray energy spectrum
The Cosmic ray energy spectrum as measured by multiple experiments is shown. Taken from [57].

2.7.1 Extensive Air showers

CRs impinge on the Earth's atmosphere and interact with atmospheric nuclei and thereby produce secondary particles. This interaction initiates a cascade due to the decay or further interaction of these secondary particles, resulting in a cascade composed of hadronic, electromagnetic, neutrino, and muonic components, as shown in Figure 2.13.

Muons are the dominant particles observed from air showers at sea level due to their high mass, which suppresses energy losses (such as bremsstrahlung) compared to electrons, as well as their relativistic speeds and a lifetime of approximately 2.2 µs. Muons produced vertically above IceCube, with a minimum energy of about 400 GeV at ground, can reach the detector due to the 1.5 km ice shield. Together with the neutrinos generated in the cascade, these two components can be detected, as they result from the decay of charged pions (π) and kaons (K).

The pions originate from the interaction of cosmic rays with protons or neutrons in the atmosphere. The produced neutral pions primarily contribute to the electromagnetic

component through their decay into two photons. In contrast, charged pions, which have a longer lifetime, have a higher probability of interacting again, leading to the production of additional charged pions and kaons. The charged pions predominantly decay to [15]:

$$\pi^+ \rightarrow \mu^+ + \nu_\mu$$
$$\pi^- \rightarrow \mu^- + \bar{\nu}_\mu$$

The most relevant kaon decays are [15]:

$$K^\pm \rightarrow \mu^\pm + \nu_\mu / \bar{\nu}_\mu \quad (63.6\%)$$
$$K^\pm \rightarrow \pi^\pm + \pi^0 \quad (20.7\%)$$

The decay of charged pions and kaons feeds the muonic and neutrino component, which can be detected by IceCube, dominated by the muon contribution.

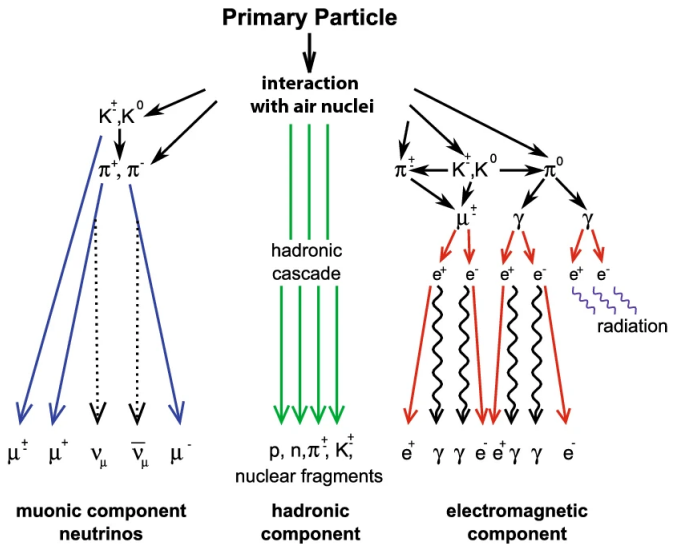

Figure 2.13: Schematic view of an extensive air shower
Schematic view of an extensive air showers, resulting in a neutrino, muonic, electromagnetic and hadronic component. Taken from [55].

3

The IceCube Neutrino Observatory

The IceCube Neutrino Observatory, discussed in this chapter, is located at the geographic South Pole[1]. It is a cubic-kilometer, multi-purpose detector (see Figure 3.1) and consists of 5160 DOMs deployed on 86 vertical strings at depths between 1.5 and 2.5 km within the Antarctic ice. Such a large detection volume is necessary to compensate the low interaction cross section of neutrinos, resulting in sufficient neutrino count rates for statistical analyses. IceCube's main purpose is to detect astrophysical neutrinos [59] and study their sources [60–62]. Also, neutrino oscillation studies, cosmic ray measurements and BSM searches are conducted.

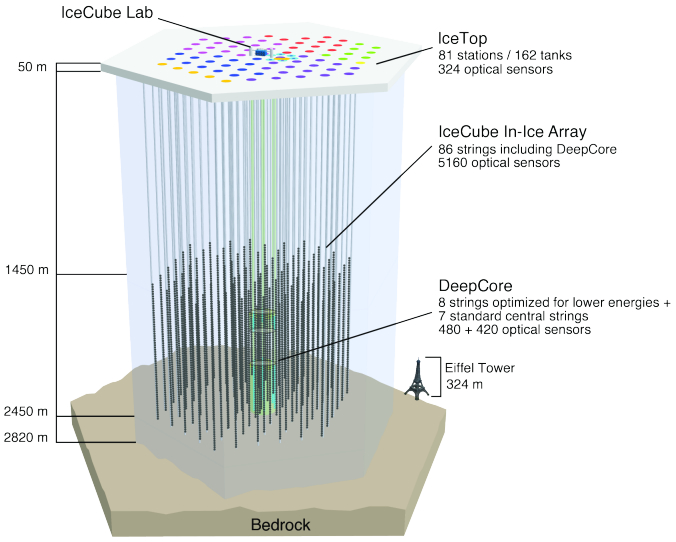

Figure 3.1: The IceCube Neutrino Observatroy
Schematic view of the IceCube Neutrino Observatory, consisting of IceTop, the IceCube in-ice array and DC. All detectors are connected to the IceCube Lab (ICL). Taken from [58].

[1]The y-axis of the right-handed IceCube coordinate system points towards Greenwich (UK) and the x-axis 90° clockwise from the y-axis. The z-axis is perpendicular to the ice surface, pointing upwards. The center of the coordinate system can be found in the literature [58].

3.1 The Antarctic ice

The Antarctic glacial ice serves as the detection medium for IceCube. It has formed over approximately 165,000 years through snow accumulation and compaction, resulting in a dense crystal structure [63]. Produced photons undergo depth-dependent scattering and absorption as shown in Figure 3.2. Within the detection volume, the absorption ranges up to 400 m, and the scattering length up to 100 m [64]. To calibrate for this, in-situ calibration measurements, using light from Light Emitting Diodes (LEDs) boards that are located within each DOM are used [66]. A notable feature is the dust layer at approximate depth of 2000 to 2100 m, where high dust concentrations significantly degrade the optical properties as shown in Figure 3.2.

3.2 IceCube

The IceCube in-ice array is designed to detect high-energy astrophysical neutrinos, consisting of 78 strings arranged in a hexagonal grid (see Figure 3.2), each with 60 DOMs. The 125 m string spacing and 17 m vertical DOM spacing together results in a lower energy detection threshold of approximately 100 GeV.

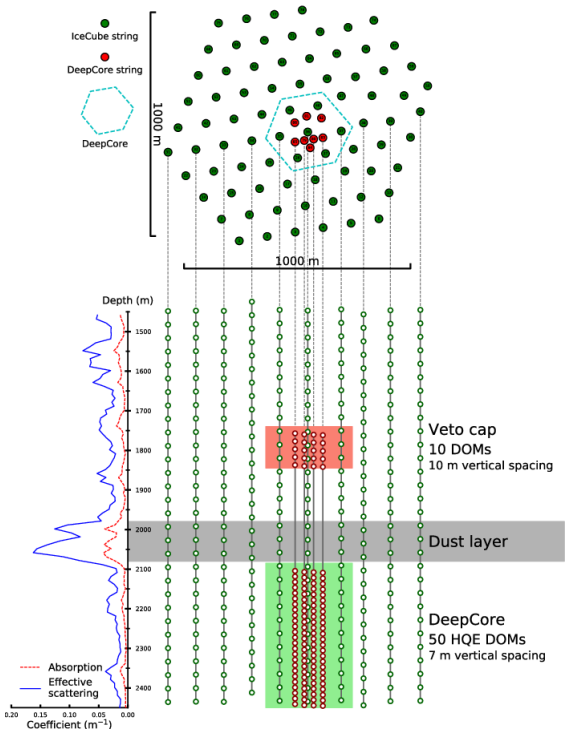

Figure 3.2: Schematic top and side view of IceCube and DC

Top view of the detector (top) with highlighted DC string selection. The side view (bottom) shows the DOM positions on DC and IceCube strings. Highlighted are the veto, dust layer and DC regions. The depth dependent inverse of the absorption and scattering coefficients are shown in the left panel. Taken from [65].

3.3 DeepCore

The denser instrumented DC sub-array consists of the 8 DC strings and 8 IceCube strings as shown in Figure 3.2 [67]. This sub-array uses the lower 40 Photomultiplier Tubes (PMTs) of IceCube strings and the lower 50 PMTs of the DC strings instrumenting a sub volume with high optical properties. The DC PMTs have, up to 35% dependent on the wavelength, higher quantum efficiency than the IceCube PMTs [67]. The average string spacing is approximately 75 m and vertical DOM spacing 7 m, resulting in a lower energy threshold of $\approx$ 5 GeV. This allows to study neutrino oscillations, searches for sterile neutrinos and enhances the sensitivity for BSM searches including the search for dim particles carrying an anomalous charge [67] [32].

3.4 The Digital Optical Module

The DOMs detect, digitize and send the information about the detected photons. The main components of each DOM are shown in Figure 3.3.

The 33 cm diameter pressure vessel protects the inside electronics, withstanding pressures up to 690 bar. Cables for the high voltage board supplies the voltage for the operation of the PMT. These are mainly 10" Hamamatsu R7081-02 sensitive between 300 nm to 650 nm. All amplified PMT waveforms above a set voltage discriminator threshold, which is equivalent to 0.25 PE, are triggered resulting in a hit [58].

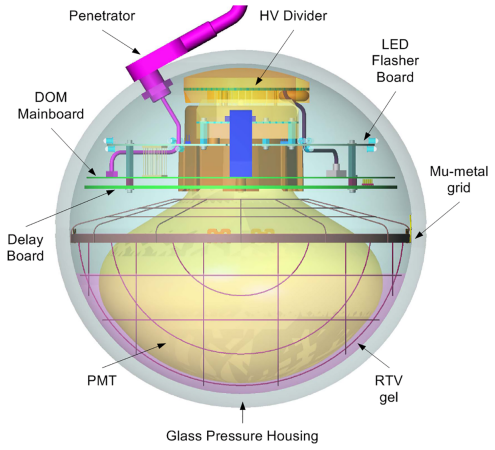

Figure 3.3: Schematic view of a DOM

The main components of a DOM are visualized. Taken from [68].

Each detected hit is assigned a coincidence label, marking it as either a HLC or SLC hit. Hits are labeled as HLCs if, within a $\pm$ 1 µs time window around the trig-

ger, the neighboring or next-to-neighboring DOMs on the same string is also above the threshold. Otherwise the isolated hit is marked as an SLC hit.

For the digitization of the hits two types of Analog to Digital Converters (ADCs) are used. The Analog Transient Waveform Digitizer (ATWD) contains the PMT signal at different amplification levels to cover the dynamic range of the PMTs. The saturation levels are 100 mV, 800 mV and 7.5 V. The input voltage is sampled at 300 Mega-samples per second (Msps) in a capacitor array. The time window of the ATWDs covers 427 ns including 75 ns before the trigger, which is possible due to the delay board.

Complementary, there is one Fast Analog to Digital Converter (FADC) launched simultaneously with the ATWD covering a larger time window of 6.4 µs. It has a sampling speed of 40 Msps. If the local coincidence condition is satisfied the complete waveform is digitized. For SLC hits only a time stamp and three samples around the FADC maximum are digitized [58]. The PMT is optically coupled via the Room Temperature Vulcanizing (RTV) gel and is shielded against the earth's magnetic field by the mu-metal grid. The flasher board controls 12 LEDs used for in-situ calibration measurements.

3.4.1 Dark Noise

The average total hit rate of the standard DOMs is $\approx$ 560 Hz and $\approx$ 760 Hz for high quantum efficiency DOMs [58]. This rate is dominated by an uncorrelated noise component originating from Potassium-40 decays and a correlated noise component. Potassium-40 is in low abundance present within the glass vessels of each DOMs [58]. Different noise components appear on distinct time scales as shown in Figure 3.4. The correlated component manifests as a short burst of hits after a radioactive decay. The decay products can excite the gas in the pressure sphere resulting in photon emission by scintillation or emit Cherenkov light themselves [69].

The uncorrelated thermionic emission of photons emitted from the photo-cathode due to heat is subdominant for the temperatures in ice, which has a depth dependent maximum of approximately T = -5 °. Overall the noise hits are dominantly SLC hits as they occur on an individual DOM basis.

[2]All SLC and HLC hits of a typical eight hour run are spooled to files independent of the rest of the Data Acquisition (DAQ). This serves as a backup and allows to look into the untriggered data in case of external

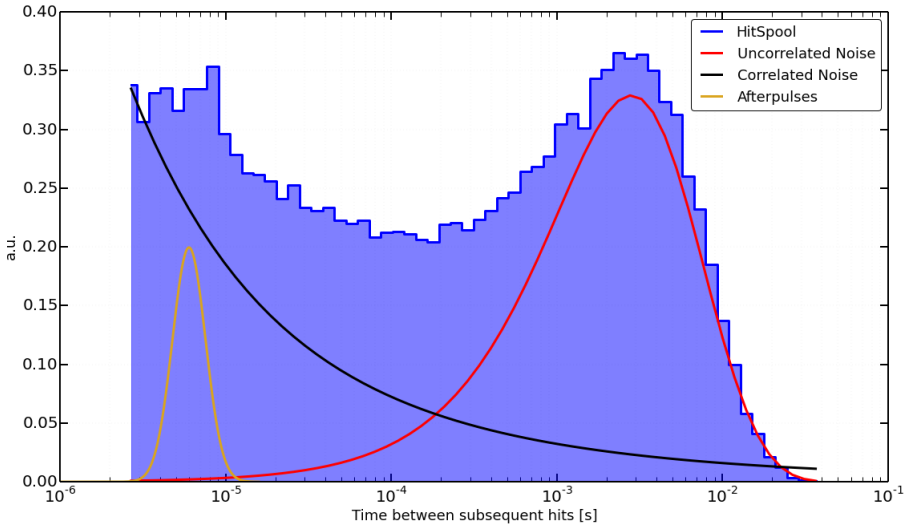

Figure 3.4: Noise components
The subsequent inter DOM hit times between consecutive hits is shown for HitSpool data[2][70]. Different noise components manifest on different time scales. Taken from [58].

3.5 Triggering

All time sorted hits are cached per string. A condensed version of the HLC hits, time sorted across all strings, is forwarded to the trigger system, corresponding to an input hit rate of approximately 77 kHz to the trigger system. The main triggers are the Simple Multiplicity Trigger (SMT) triggers with one IceCube and one DC version, the volume and string triggers. All of these are explained in detail in [58]. The IceCube SMT requires at least eight HLC hits in a time window of 5000 ns, adjusted to the time it takes a relativistic signature to cross the detector. The DC SMT, optimized for detecting faint signals, requires at least three HLC hits within a 2500 ns window.

The FPT explained in chapter 5 operates on all DC DOMs. It is optimized for the detection of faint signatures as explained in section 2.3, which due to the reduced photon emission compared to particles carrying the elementary charge, dominantly produces SLC hits. To utilize SLC hits at trigger level, the DAQ team used a free bit to store local coincidence information for each hit forwarded to the trigger system. Additionally, a study [71] confirmed that both SLC and HLC hits could be time sorted across all strings, which was not previously necessary. These developments are also advantageous for the upcoming IceCube Upgrade, which will use a dedicated DAQ to handle higher rate multi-PMT

alerts.

modules[3] [72, 73].

All time sorted SLC hits from DC and all time sorted HLC hits from IceCube, corresponding to an input hit rate to the trigger system of approximately 600 kHz, are now forwarded to the trigger system. Each trigger can subscribe to a HLC or HLC plus SLC (limited to DC) input hit stream.

Following this, trigger algorithms are applied, and around each readout window sized according to the trigger type is laid around each trigger window to capture early and scattered photons. To allow for the merging of multiple readout windows, a Throughput Trigger is laid around each readout window, starting 10 µs before the trigger start time and extending for a length dependent on the readout window size, with a minimum duration of 20 µs. Overlapping Throughput Triggers are combined into a single Global Trigger, which includes IceTop triggers as well [58]. The Event Builder processes Global Trigger requests, retrieving all cached SLC and HLC hits within the designated readout windows across the entire detector and stores them along with trigger information in an event.

The median event rate at trigger level is approximately 2.7 kHz corresponding to approximately 1 TB of triggered data per day. The event rate varies by approximately $\pm$ 10 % with the atmospheric muon flux [74].

[3]For the IceCube Upgrade it is at the time of writing not clear if all hits of the modules will be sent to the surface, or only hits that already satisfy an inter PMT coincidence condition.

3.6 Transmission and filtering

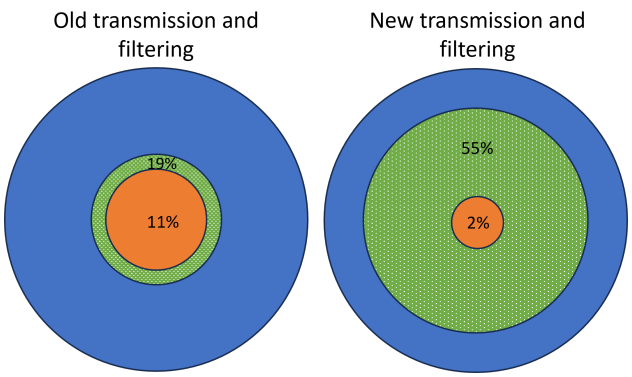

Figure 3.5: IceCube filtering and transmission
The blue area corresponds to the event rate of 2.7 kHz at South Pole and the green dotted area to the filtered event rate that is transmitted via satellite. The orange area corresponds to the offline filtered data that are saved in the long term storage. The left figure shows the values until 2023 and the right figure the values of the new scheme. The area covered by the newly filtered offline data (shown in the right figure in orange) may be subject to changes.

All triggered events are forwarded to the online Processing and Filtering (PnF) system where at first calibrations of the waveforms and simple reconstruction algorithms are applied [58].

3.6.1 Transmission and filtering until 2023

Until the end of the 2023 data taking season around 25 specialized filter selections were applied to the processed data reducing the amount of data to $\approx$ 100 GB per day, which is compatible with the available satellite bandwidth. Roughly 500 Hz of online-filtered events were transmitted in compressed format, while all processed, triggered events were stored on hard drives at the South Pole for annual shipment.

In the North to the online filtered events, more sophisticated offline filter algorithms were applied further reducing the rate as seen in Figure 3.5. Approximately 300 Hz of offline filtered events were stored in long-term storage and are directly accessible.

3.6.2 Transmission and filtering from 2023 on

To reduce the amount of data for the long-term storage and improve the code maintainability, the filtering scheme is changed. Now approximately 1.5 kHz of events are transmitted

fitting in the 100 Gb/day bandwidth. These data are planned to be stored on a few years scale. The reduction from the 2.7 kHz trigger level rate is mainly driven by applying a tighter minimal bound of 12 HLC hits to the IceCube SMT trigger before transmission. The SMT DC and the newly developed FPT (described in chapter 5) are among others considered as "TriggerFilters" and all events of these triggers are transmitted. Only a handful of modern implementations of the old online filters are run at South Pole. These include the online DC filter, which reduces the amount of events triggered by the DC trigger.

To this new stream of transmitted events around 15 newly developed offline filters are applied, including the FPF as described in chapter 7. The new offline filters provide modern implementations of frequently used filter selections, including new cuts to reduce the online filter rate. This approach is intended to significantly reduce the amount of data that needs to be stored in the long term, aiming for a decrease of approximately one order of magnitude compared to the old filtering.

3.7 Neutrino signatures

Neutrinos are electrically neutral and can be detected by secondary particles produced via the weak force, in a NC or CC interaction:

$$\begin{aligned} \nu_l + N &\xrightarrow{W^-} l^- + H \quad (CC) \\ \nu_l + N &\xrightarrow{Z^0} \nu_l' + H \quad (NC) \\ l &\in \{e^-, \mu, \tau\} \end{aligned}$$

In these processes, N represents the nucleus, Z and W^+ the bosons of the weak interaction and H the hadronic remnant. In the NC interaction a fraction of the neutrino's energy is transferred to the nucleus and the only observable is the hadronic remnant. In the CC interaction, the interaction products include a charged lepton and a hadronic remnant. The different event topologies for the different charged leptons can be seen in Figure 3.6. FCPs produce tracks like muons, which gets dimmer with decreasing charge.

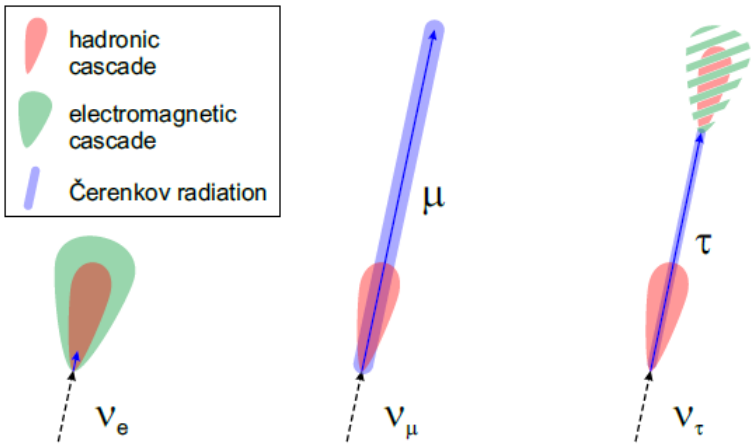

Figure 3.6: Schematic view of charged current neutrino topologies
For all final states a hadronic cascade is present. Electrons initiate an electromagnetic cascade. Muons result in tracks with the length determined by decay or stopping of the muon. A tau produces a track before decaying, which produces a cascade. The track length depends on the energy. Taken from [75].

4

Simulation

In this chapter the simulation framework used to simulate FCP in IceCube is explained. Additionally, the effective area is introduced as a measure of the detector's sensitivity to the simulated signal. It is proportional to the ratio of detected events to generated events.

4.1 Signal simulation

Signal events in IceCube are simulated via a chain of modules within the IceTray simulation framework. These include the generation and propagation of the FCP, followed by the photon propagation in ice. After that the detector response is simulated, resulting in triggered events.

4.1.1 Event generation

Events are generated on a generation disk with radius $r_{disk} = 900\,\mathrm{m}$ and distance to the detector center $d_{disk} = 1000\,\mathrm{m}$ (see Figure 4.1). The starting position of the FCP track on the generation disk is randomized. Subsequently, the generation disk is randomly rotated, and the particle is emitted perpendicular to the disk's surface, resulting in an isotropic flux around the detector.

4.1.2 Event propagation

The propagation through the ice of the FCP is done with PROPOSAL [52] [53]. Here for a given mass and charge, for the assumed stable particle, the corresponding cross-sections are calculated. The resulting energy losses, produced secondaries and their corresponding

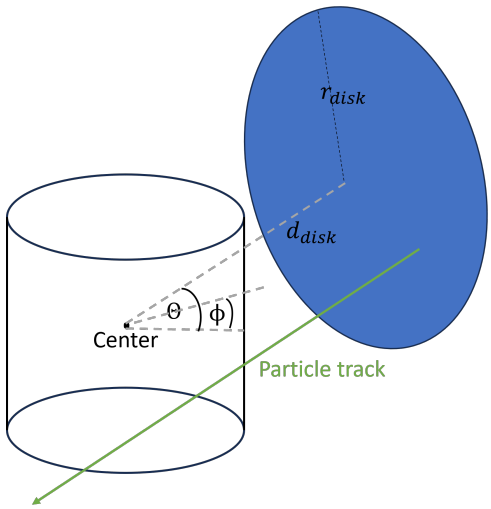

Figure 4.1: Schematic view of the FCP event generation
Shown is the generation disk in blue and the cylindrical shaped detector. Particles are injected perpendicular to the generation disk, visualized by the green track.

energy losses are saved in a tree like manner that. This tree is then forwarded to the photon propagation code [76], which collects the produced photons and propagates them through the ice, saving those that hit a photo cathode of a DOM.

4.1.3 Detector simulation

The detector simulation involves multiple steps. The vuvuzela module simulates the dark noise components (as discusses in subsection 3.4.1) with exponential components for the uncorrelated components and a log-norm contribution for the scintillation hits. For each event, noise hits are overlaid on the signal, with additional noise simulated 10 µs before and after the signal.

The PMT response is simulated, accounting for PMT jitter, pre-pulses[1], late pulses, and afterpulses, followed by digitization and the application of the local coincidence condition. Subsequently, trigger algorithms are applied, resulting in the storage of hits only within the corresponding trigger readout window for each simulated event.

All of these information are to this point stored in so called q-frames (short for DAQ frames). These are designed to store all the information from the trigger readouts and simulation input parameters.

[1]Pulses are reconstructed from the digitized waveforms. The charge information of the pulses is in this thesis not used and the term hit is used throughout this thesis.

4.1.4 Processing and Filtering

Afterwards the processing and filtering algorithms as explained in section 3.6 are applied. These form so called p-frames (physics frames), by first applying a so called TriggerSplitter module on a definable subset of triggers. These are in this thesis all the IceCube triggers. The splitter module looks for larger gaps than 10 µs between triggers stored in the event and can form multiple p-frames that inherit from the q-frame. Each p-frame corresponds to a specific time window of the q-frame and the corresponding hits are stored in a mask. To these p-frames the filter algorithms are applied and the information of passing or failing of that filter for that p-frame is stored for each filter.

4.1.5 Effective area

The effective area is proportional to the measured count rate of the detector. A particle flux is given in units of particles per solid angle, area and time. This can be converted to an initial particle rate for a specific angular coverage, detector size and time. The measured rate by the detector will be lower than the initial rate, due to the detection efficiency of the detector. The effective area quantifies this.
For the case of fractionally charged particles the flux and effective area are dependent on the charge, energy, mass and the solid angle. All effective area will be averaged over the chosen energy spectra, which suppress high energies. Therefore, the energy dependence is not analyzed here but accounted for by the survival probabilities that are energy dependent. The count rate of detected events per solid angle can be expressed by:

$$\frac{d^2N_{det}}{dtd\Omega}(\varepsilon,m,E) = \Phi(\varepsilon,m,E,\Omega)\cdot A_{eff}(\varepsilon,m,E,\Omega)$$

As all results will be averaged over the azimuth angle the integration over the zenith angle remains:

$$\frac{dN_{det}}{dt} = 2\pi\int_0^\pi \Phi(\varepsilon,m,E,\theta)\cdot A_{eff}(\varepsilon,m,E,\theta)sin(\theta)d\theta$$

The charge and mass of the particle have different effects on the flux. For higher masses and lower charges at a fixed solid angle, the flux is increased due to the reduction of energy loss processes. For lower masses and higher charges the opposite holds true.
On the other hand the effective area shows a contrary behavior compared to the flux. For higher masses and lower charges at a fixed solid angle, the effective area is reduced due to the reduction of energy loss processes.
Results are shown for different simulations samples with fixed ε between 1/33 and 2/3 at and masses between 5 GeV and 100 TeV. The effective area is evaluated for FCP searches. For MCP the expected count rate $\frac{dN_{det}}{dt}$ is evaluated for the MCP model explained in section 2.4.
Different combinations lead to more isotropic or non-isotropic scenarios. In the case of an isotropic scenario the effective area can be averaged over all solid angles, resulting in $< A_{eff} >_{\Omega}$. This quantity is important to analyze relative improvements of trigger and filter efficiencies, which are not expected to vary for different zenith angle intervals.
Furthermore, this allows to directly calculate improvements by the new trigger compared to the previous analysis, which assumed an isotropic scenario [32].
In the non-isotropic case the effective area is dependent on the zenith angle and thus only averaged over the azimuth angle. This can be used to more properly calculate expected event rates for a MCP flux model in different zenith bins and analyze up to which zenith angles signal is expected.
$< A_{eff} >$ is inferred from simulations. N_{gen} events are generated and N_{det} events are detected. For the isotropic case this can be calculated by [77]:

$$< A_{eff} >_{\Omega} = A_{gen} \cdot \frac{N_{det}}{N_{gen}} \tag{4.1}$$

To introduce a non-isotropic flux, a survival probability is assigned to each event (2.6), which depends on the charge, direction, energy and mass. Each event is weighted according to this survival probability resulting in a non-isotropic flux around the detector.

$$< A_{eff,ni} >_{\Omega} = A_{gen} \cdot \frac{\sum_{i=1}^{N_{det}} weight_i}{N_{gen}} \tag{4.2}$$

The zenith dependence of the effective area can be analyzed as well. The zenith dependent effective area in the angle interval of $\theta_{int} = [\theta_{min}, \theta_{max})$ is calculated by:

$$< A_{eff,ni}(\theta_{int}) >_{\phi} = A_{gen} \cdot \frac{\sum_{i=1}^{N_{det}(\theta_{int})} weight_i}{N_{gen}} \tag{4.3}$$

Furthermore, the following relation holds for the two quantities, when dividing the zenith in n angle intervals:

$$< A_{eff,ni} >_{\Omega} = \sum_{i=1}^{n} < A_{eff,ni}(n) >_{\phi}$$

The total error on the effective area is determined by N_{det}following a binomial distribution and is given by:

$$\sigma_{<A_{eff}>_{\Omega}} = \frac{\sqrt{N_{det} \cdot (1 - \frac{N_{det}}{N_{gen}})}}{N_{gen}} \cdot A_{gen}$$

In case of the non-isotropic cases, N_{det} can be replaced by:

$$\sum_{i=1}^{N_{det}} weight_i$$

Systematic uncertainties arising from the f.e. the simulated signal properties and used ice model on the effective area are not discussed in this thesis and would be conducted in dedicated analyses searching for fractionally charged particles.

4.2 FCP properties

In Figure 4.2 an example of a simulated FCP with a mass of 1 TeV and an ε of 1/3 can be seen. It was simulated with the chain described in this chapter. One can see that for the FCP only a handful of signal hits in DC are produced. These are dominantly SLC hits and cluster along the track. Separating them by eye from detector noise contributions, occurring randomly over the entire detector, is not possible. However, the signal hit pairs are expected to be velocity consistent and to cluster in a certain direction.

The FCP signal is characterized by a dim track dominantly producing SLC hits. To further

quantify the hit type dominantly produced by FCPs the SLC fraction[2] is analyzed. This is the ratio of all SLC hits produced by the signal and total number of hits produced by the signal (see Equation 5.1). One corresponds to an event that only produced SLC hits and zero to an event that only produces HLC hits. In Figure 4.3 one can see that these events dominantly produce SLC hits with a main contribution in the events only consisting of SLC hits. This is the reason why the previous analysis saw a significant decreases in trigger efficiency (subsection 2.3.1) for these particles. As the standard triggers only analyze HLC hits they miss for most FCP events a large fraction of the available information.

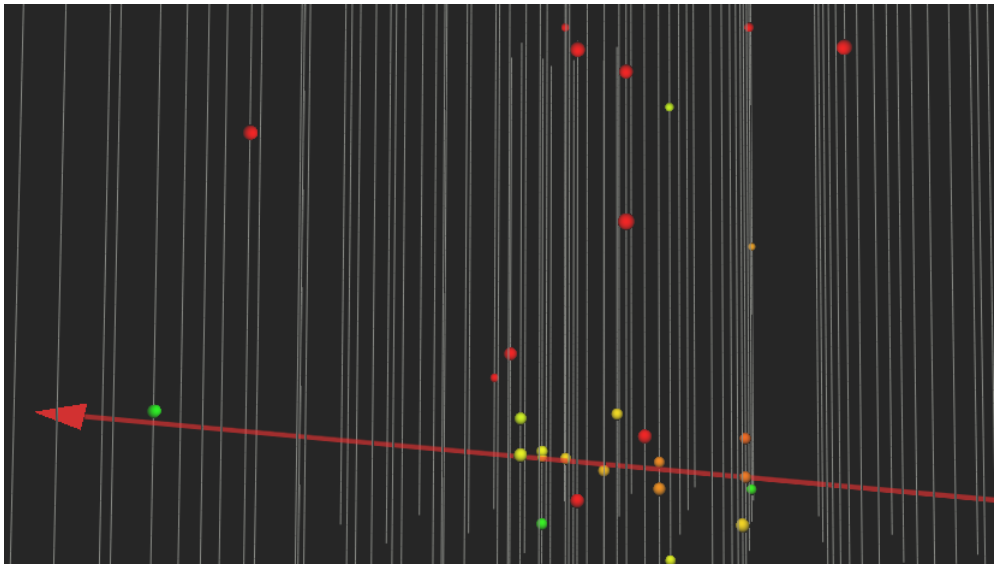

Figure 4.2: Simulated FCP
A simulated FCP with a mass of 1 TeV and an ε of $\frac{1}{3}$ is shown. The color encodes the time of the hits from early (red) to later (green) times. The red arrow corresponds to the simulated direction. The time interval is chosen such that most of the detector noise hits, simulated before the signal, appear in red.

[2]The SLC fraction is used as a cut variable in the FPT and is discussed in subsection 5.1.5

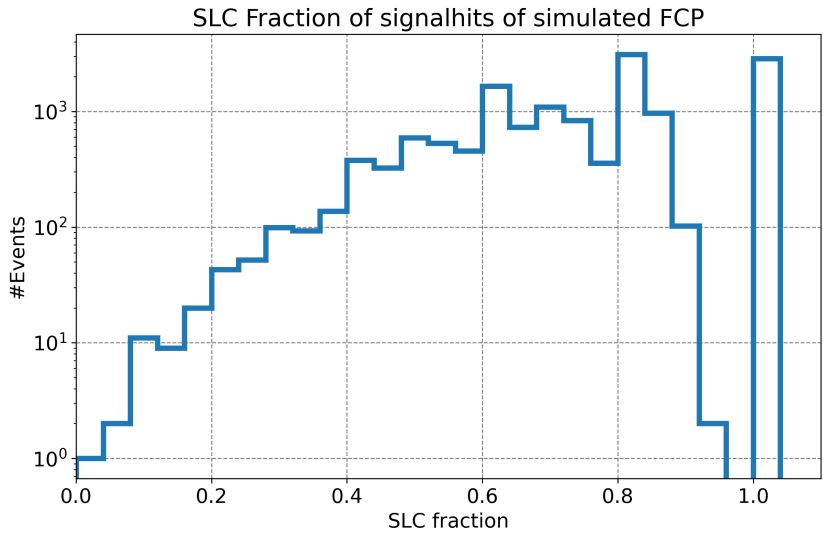

Figure 4.3: SLC fraction for FCP

Shown in the SLC fraction of signal hits produced by FCP with an ε = 1/3 and a mass of 1 TeV, following an energy spectrum with spectral index of 2 that starts above Cherenkov threshold.

5

The Faint Particle Trigger

This chapter describes the Faint Particle Trigger. The trigger analyzes all SLC and HLC hits of DC modules. These are forwarded to a sliding time window and within each time window four cut variables are calculated, which are shown in Figure 5.1. These remove too bright signatures and noise contributions.

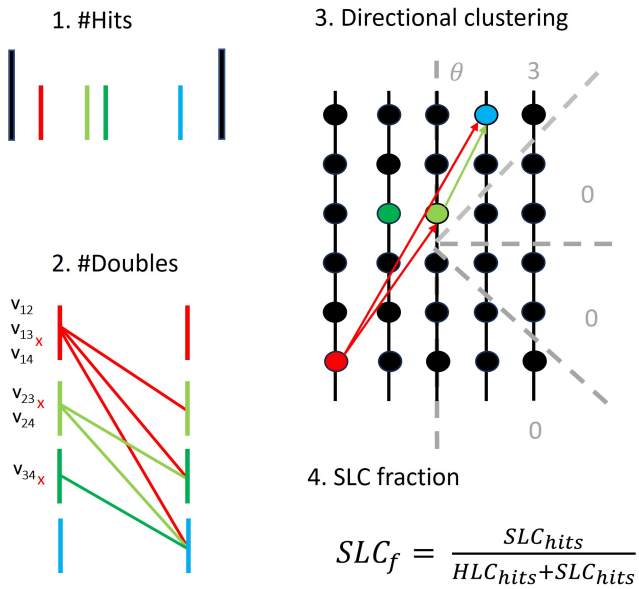

Figure 5.1: Faint Particle Trigger concept

For 1) the black lines represent the boundary of the time window. The colored lines represent the hits and the color encodes the time from early (red) to later times (blue). The example time window contains four hits. In 2) it is shown how hit pairs are formed. The red X's next to the velocity of hit pairs indicate that the hit pair failed the velocity cut. The black lines in 3) represent the IceCube strings and the black dots the DOMs. For the Doubles the direction is calculated, indicated by the colored lines. The grey coordinate system shows that the angular range is binned and it is counted how many Doubles are in each bin (grey numbers). The value of the bin with maximum counts is used for the third cut. For the last cut the SLC fraction is calculated. All hits in 3) are SLC hits, which would result in 1 for the SLC fraction of this example.

5.1 Faint Particle Trigger DC version

The figures in this chapter show distributions of cut variables and trigger efficiencies for simulations of FCP with an ε of 1/3 and a mass of 1 TeV. The energy spectrum starts above the Cherenkov threshold at 1.5 TeV up to $1.5 \cdot 10^5$ TeV. Only high-quality events that produce at least 10 signal hits in DC were selected. This threshold is chosen to make sure that the event contains enough information to reconstruct the direction properly. The reconstruction of the additional triggered events was investigated in a dedicated thesis [78]. Additionally, simulated detector noise is shown, which is in detail explained in subsection 3.4.1. Furthermore Fixed Rate Trigger (FRT)[1] data are shown. These unbiased detector data were used during the development of the FPT to estimate the trigger rate and to inspect the cut variable distributions for data.

5.1.1 Sliding time window

For the FPT, a sliding time window approach was chosen, as illustrated in Figure 5.2. The time window, with length l, is filled with hits until the first hit lies outside the window boundaries (red line in Figure 5.2). The variables for the filled window are then calculated. Afterwards, the window is shifted by the time window separation parameter s until the hit, that was outside of the boundaries, lays within the shifted window. Then this procedure is repeated. The l parameter is set to 2500 ns, which is the same time window size used by the dedicated DC trigger, adjusted for a relativistic signature traversing DC.

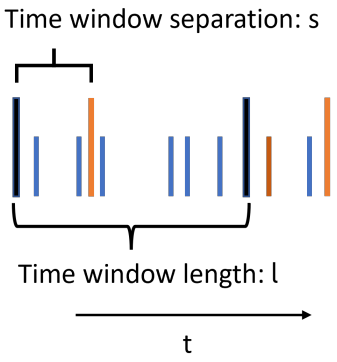

Figure 5.2: Sliding time window

The time window and shifted time window are represented by the black and orange lines. The blue lines represent the hits and the red line the first hit that lays outside the first time window.

[1] The FRT reads out the entire detector for 10 ms every 300 s.

The *s* parameter is set to 800 ns, resulting in the analysis of 1.25 million time windows per second. The impacts of different choices for *s* were analyzed and are summarized in subsection 5.1.6. If the time window satisfies all four cuts, it is triggered. If a consecutive overlapping time window is also triggered, the trigger is extended up to a maximum length of 10 ms. This maximum trigger length was chosen to prevent the DAQ system at the South Pole, in the case of unlikely trigger lengths, from starving. Typical event lengths for FCPs range up to 10 µs, so the 10 ms limit is a safe choice that does not conflict with the targeted physics.

As described in subsection 4.1.3, the simulated signal events consist of three parts: an initial part of noise hits only, a mix of signal and noise hits, and a final part containing only noise hits. The plots shown for the optimization of the cuts in the following sections use only one time window per simulated signal event to characterize the signal. This time window is the first one in the event, with the lower bound being greater than or equal to the time of the first signal hit. This approach typically excludes the first signal hit but ensures that a large fraction of signal hits is included in the window for most events.

For the final summary plot (see Figure 5.12), the final trigger algorithm is applied, which slides the time window over the entire event. Since now multiple time windows per event are analyzed, this increases the probability for the small fraction of events, lacking a significant number of signal hits in the initially used window, that a time window that contains a larger fraction of signal hits is now analyzed. Thus, the distributions used to set cuts do not precisely represent the improvements in signal efficiency as shown in Figure 5.12.

For the Detector Noise and FRT data distributions, the sliding algorithm was applied to a few seconds of simulated detector noise and FRT data collected in July 2016 (data from that year were processed and are directly accessible). All values from all analyzed windows are presented, as this corresponds to the background and noise expectations of the trigger applied in real time.

5.1.2 Cut 1: Number of hits

The first variable calculated in each time window is the hit count. Its purpose is to eliminate excessively bright signatures and noise contributions.

In Figure 5.3, the distributions for FCP, Detector Noise, and FRT data are shown. In the FCP distribution, highest contributions are observed at 10 and 11 hits. This is expected, as a minimum of ten signal hits was required for each event. Since noise hits are included in the count, it can be assumed that for most signal events, not all signal hits are contained within the single window. This can occur due to scattering effects, which result in hits being outside the upper time window boundary and the first hit being excluded by construction. Events with a lower number of hits occur due to the positioning of the selected time window. The density decreases significantly as the number of hits decreases, leading to the assumption that, for a large fraction of events, most signal hits are confined within the selected window.

The tail of events with more hits than the peak of the distribution reflects the probability of the FCP producing additional signal hits, which decreases rapidly.

The Detector Noise distribution peaks at much lower values, as expected. The lower bound

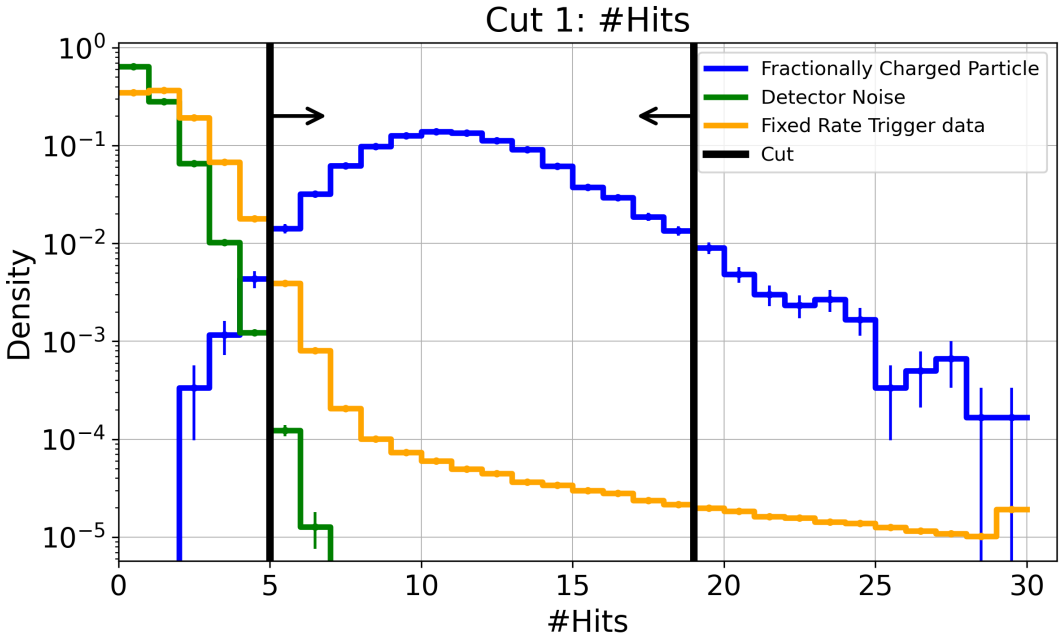

Figure 5.3: The number of hits in the time window
The number of hits shown for simulated FCP with ε of 1/3 and a mass of 1 TeV (blue), simulated Detector Noise (green) and FRT data (orange). The black lines indicate the cut values and the arrows the region that is kept by the cut.

for the number of hits cut is set to be greater than or equal to 5, significantly reducing the contribution from Detector Noise.

The FRT data predominantly contain Detector Noise and atmospheric muons. The distribution is shifted to a higher mean compared to the Detector Noise distribution and exhibits a large tail corresponding to muons. To cut out the too bright signatures which do not correspond to the signal properties an upper bound of 19 hits was chosen. When applying the sliding time window algorithm and implementing the first cut ($5 \leq \#Hits \leq 19$), 99.7% of the signal events are kept (see Figure 5.12).

5.1.3 Cut 2: Number of Doubles

The second variable is the number of Doubles, a count of velocity consistent hit pairs. Its purpose is to further reduce the contribution from Detector Noise.

To decrease the rate of time windows filled with detector noise hits, the velocity consistency of the hits within the time window is analyzed. For noise hits, no velocity consistency is expected. For this cut, all possible hit pair combinations in the time window are formed, excluding combinations with the hit itself and commutative combinations. The total number of hit pairs is given by:

$$N_{hit\,pair} = \frac{x!}{(x-2)! \cdot 2!}$$

x corresponds to the amount of hits in the time window and has a maximum of 19, limiting $N_{hit\,pair}$ to 171 per time window. Then the corresponding velocity of each hit pair is calculated. The hit pair velocity distributions for Detector Noise and FCP are shown in Figure 5.4.

The amount of hit pairs per simulated signal event differs and the signal distribution shows multiple velocities per event. The blue FCP distribution shows a clear peak at the speed of light, representing hit pairs from hits along the track that are connected by that speed. Lower values can occur due to scattering effects. Higher values can occur due to photons emitted from the same position of the track, hitting DOMs at different positions.

The Detector Noise distribution shows a peak at $\approx 4 \cdot 10^5$ km/s. This is driven by the time window length allowing a maximum Δt of 2500 ns and the distance distribution, which

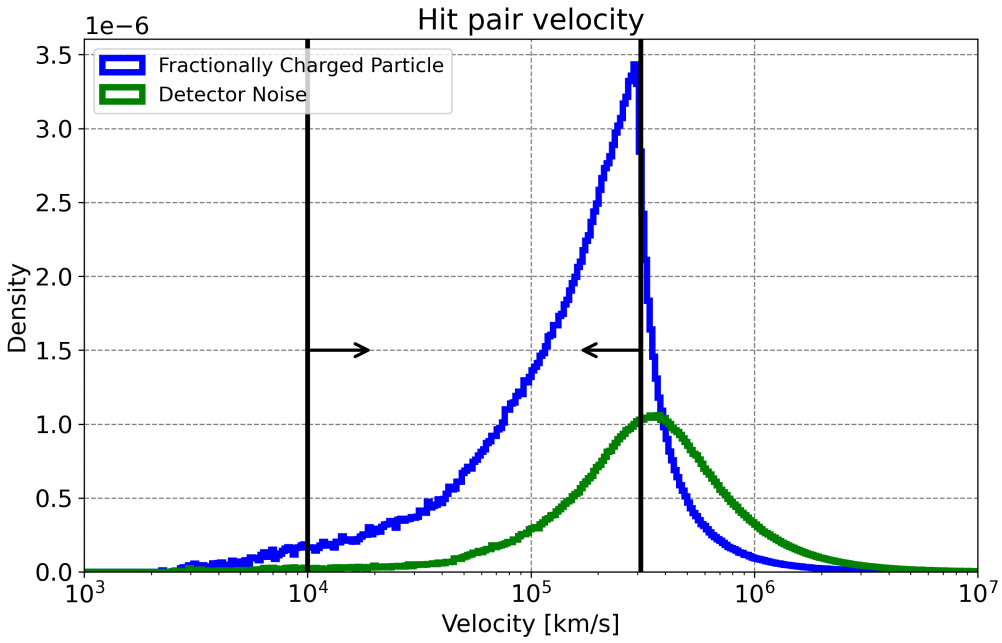

Figure 5.4: Hit pair velocity distribution

The hit pair velocity distribution is shown for FCP (blue) and Detector Noise (green). The black lines indicate the cut values and the arrows the region that is kept by the cut.

peaks at the string and DOM spacings within the DC region (both distributions before and after the velocity cut are shown in Figure A.2 and Figure A.1).

If the velocity falls within the range $0.03c < v_{\text{hitpair}} < 1.03c$, it is kept. After the velocity cut, $\approx 16\%$ of the Detector Noise hit pairs and $\approx 60\%$ of the FCP hit pairs remain. Each hit pair in the defined velocity interval is classified as a Double.

The number of Doubles per event is counted and the corresponding distributions shown in Figure 5.5. The Detector Noise clusters at lower values compared to the FCP distribution. This underlines that the amount of velocity consistent hit pairs for Detector Noise is significantly lower as expected. To reduce the Detector Noise contribution by a factor of ≈ 14 a lower bound on the number of Doubles of 10 was chosen. The second cut ($\#Doubles \geq 10$) reduces the Detector Noise contribution to ≈ 57 Hz and 97.4% of the signal events are kept (Figure 5.12).

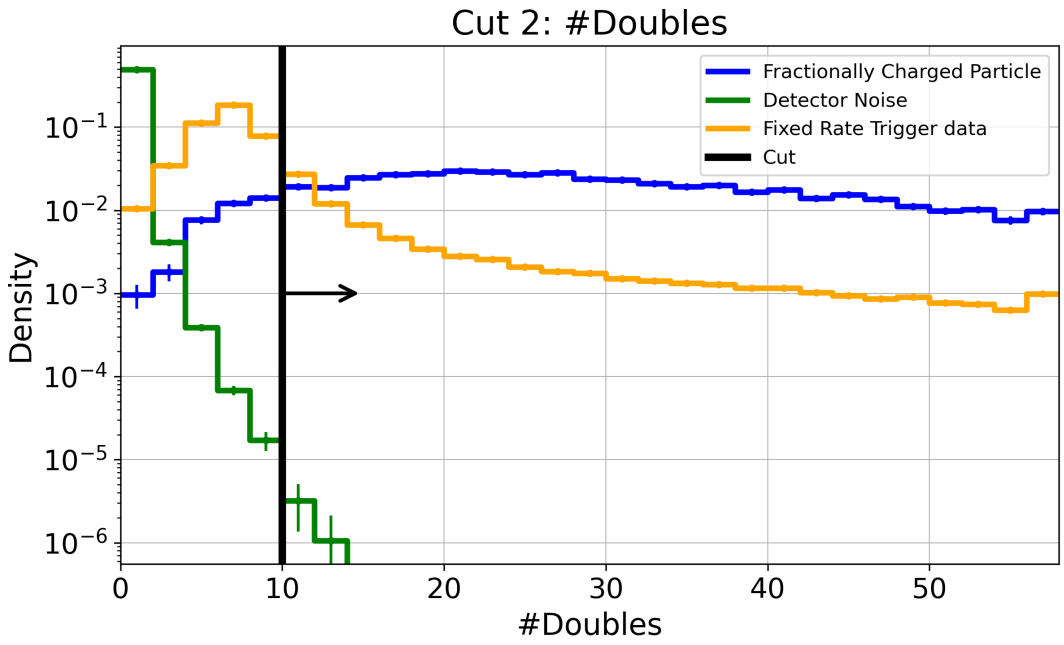

Figure 5.5: Number of Doubles in the time window
The number of Doubles shown for simulated FCP with ε of 1/3 and a mass of 1 TeV (blue), simulated Detector Noise (green) and FRT data (orange). The black line indicates the cut value and the arrow the region that is kept by the cut.

5.1.4 Cut 3: Directional consistency of Doubles

The third cut quantifies the directional clustering of Doubles, aiming to further reduce the Detector Noise contribution to the few Hz level.

For this cut, the azimuth and zenith angles for each Double are calculated. For Detector Noise Doubles within a time window, no preferred direction is expected. The approach involves creating histograms of the zenith and azimuth angles and applying a cut based on the maximum bin count value, which is anticipated to be higher for FCPs than for Detector Noise.

An example is shown in Figure 5.6, which illustrates one FCP event overlaid with Detector Noise. For all Doubles in the event, the zenith angle is calculated and histogrammed in 20° bins. A clear excess of Doubles at the true zenith direction is observed, resulting in a maximum bin count value of 16. Such a peaked distribution is not expected for Detector Noise, which should on average have lower maximum bin counts when analyzing many events. To find a suitable bin size, bin sizes between 5° to 50° in steps of 5° were analyzed and the distributions for 5° and 20° are shown in Figure 5.7. In general the cuts that can

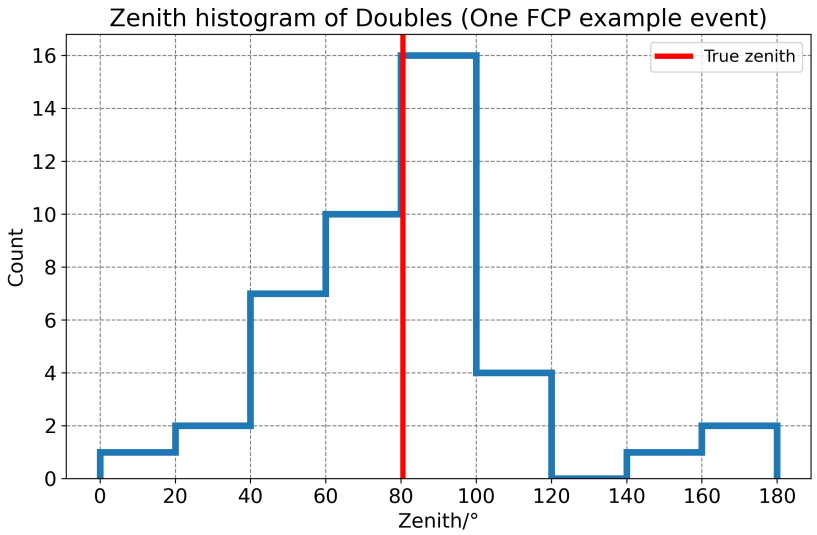

Figure 5.6: Directional clustering of Doubles for one example event
The figure shows the zenith histogram of Doubles of an example event (blue). In red the true direction is shown.

be set between 20°-50° show no significant deviation (50° binning is shown in Figure A.3). Here the preferred option is the lowest value, since it was planned to use the histograms as an directional estimate for later processing. This option was tested in [78] and showed inferior directional reconstruction compared to other methods.

For bin sizes between 5°-15° also no significant deviation was observed. Below 20° the cutting options are more limited and a comparison of the 5° and 20° options showed that when cutting for > 2 in the 5° binning 77% of the signal events and 25.4% of the Detector Noise time windows remain. At 20° when cutting for > 4.75% of the signal events and 17.5% of the Detector Noise time windows remain. Thus, the bin size was set to 20°, which showed a better Detector Noise and signal separation compared to the lower bin sizes. The same procedure is applied to the azimuth angle resulting in the same bin size.

The final cut is then based on the maximum bin count of the zenith vs. azimuth 2D histogram, which are shown in Figure 5.8 for FCP and Detector Noise (The FRT data 2D histogram can be found in Figure A.4). In order to reduce the Detector Noise rate to the few Hz level a simultaneous condition on the maximum bin counts of the zenith and azimuth histograms being larger than 4 are applied. 89.1% of the signal events survive this cut (Figure 5.12).

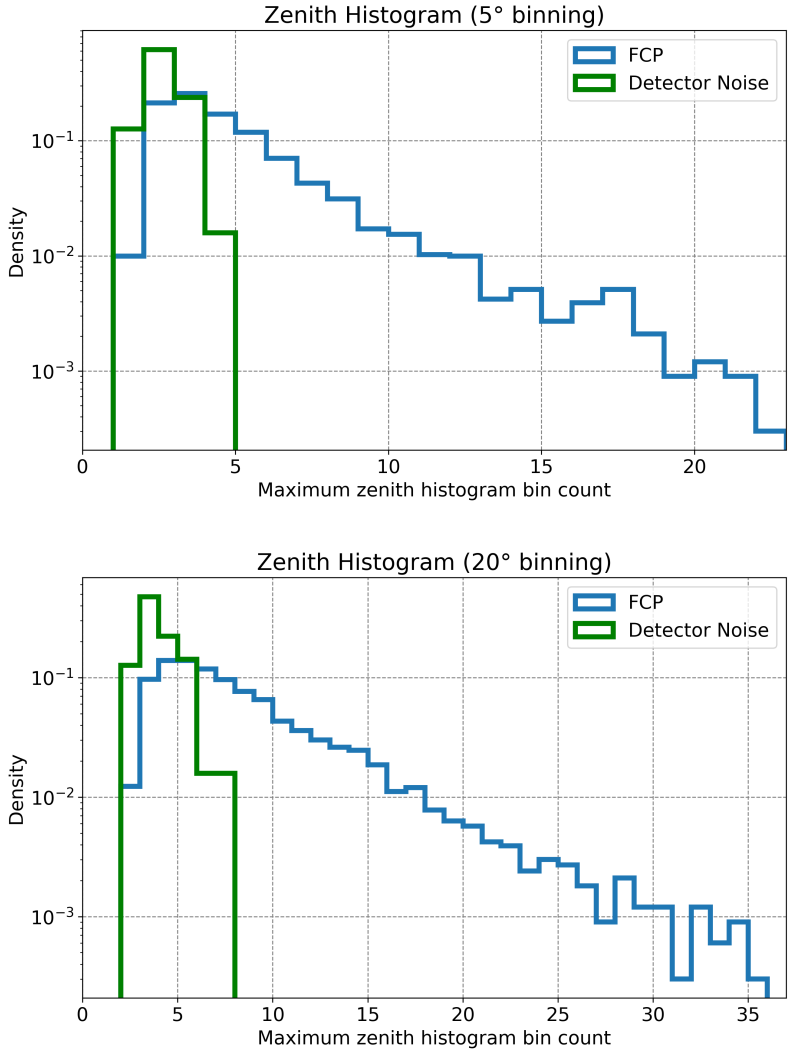

Figure 5.7: Bin sizes for directional clustering of Doubles

The maximum bin counts of the zenith histograms for a bin size of 5° (top) and 20°(bottom) are shown. In blue for FCP and in green for Detector Noise

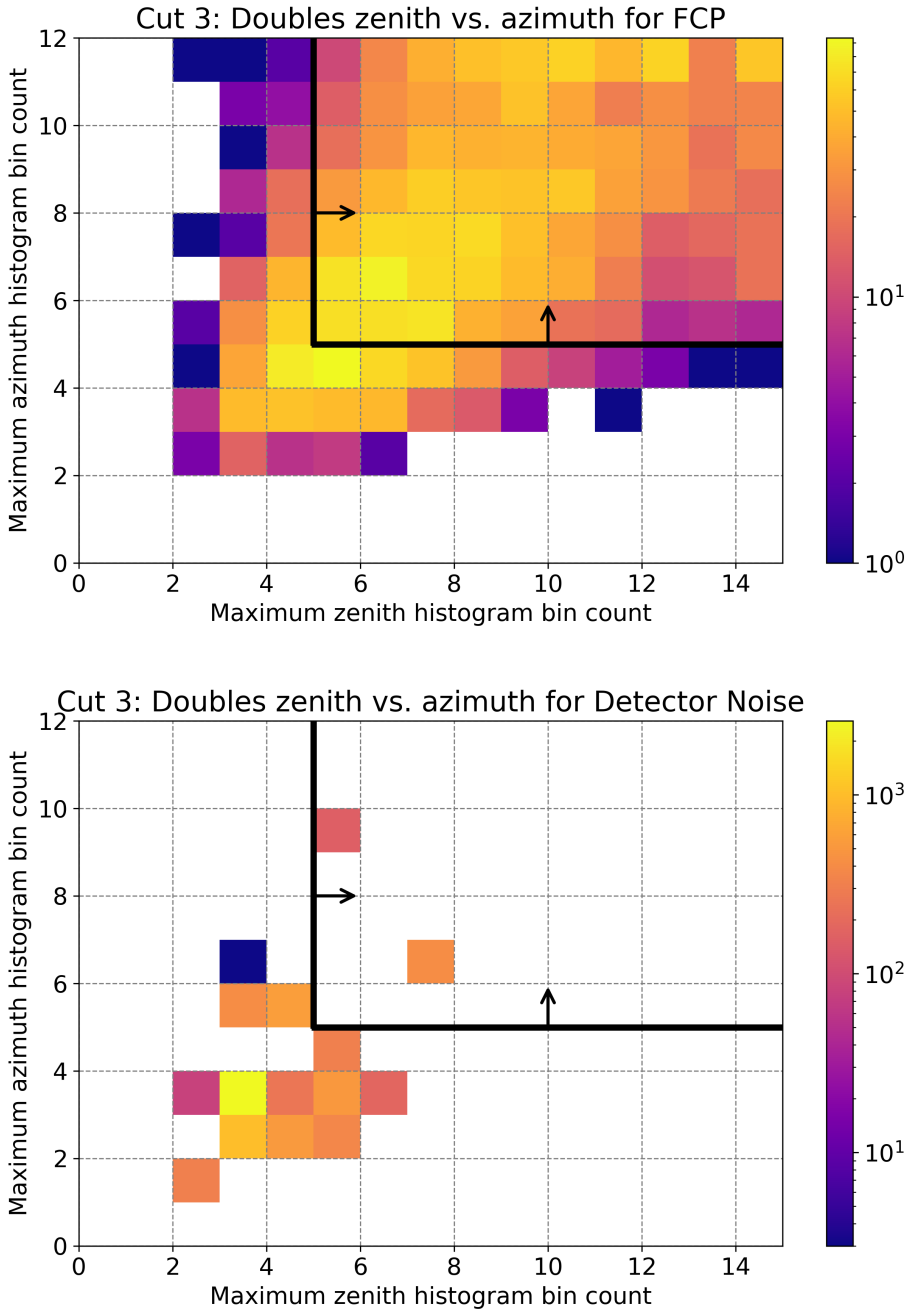

Figure 5.8: Maximum zenith vs. azimuth bin count for FCP and Detector Noise
The maximum bin count of the zenith vs. the azimuth histogram is shown for simulated FCP (top) and Detector noise (bottom). The black lines indicate the cut values and the arrows the region that is kept.

5.1.5 Cut 4: SLC fraction

The fourth cut is based on the fraction of SLC hits in the event. Its purpose is to remove parts of the atmospheric muons. The Detector Noise contribution is reduced to the few Hz level after the third cut. As FCP and Detector Noise dominantly produce SLC hits, now a cut based on time windows carrying a high fraction of SLC hits can be applied. The last cut aims to remove events that predominantly produce HLC hits. To achieve this, the ratio of the number of SLC hits to the total number of hits in the time window is calculated.

$$SLC_f = \frac{SLC_{hits}}{HLC_{hits} + SLC_{hits}} \tag{5.1}$$

The corresponding distributions for FRT data and FCP are shown in Figure 5.9. A value of zero corresponds to time windows that consist solely of HLC hits, while a value of one corresponds to time windows that contain only SLC hits. The FCP signal hits distribution exhibits a peak at 1, as seen in Figure 4.3. The SLC fraction between 0.8 and 1 is more suppressed due to the limited number of hits in the time window, which is cut at 19. The less pronounced tail towards HLC dominated time windows is expected, as SLC hits are the dominant hit type for FCPs. For the FRT data distribution the tail towards HLC dominated events is more pronounced due to the muonic component, which can be reduced with the

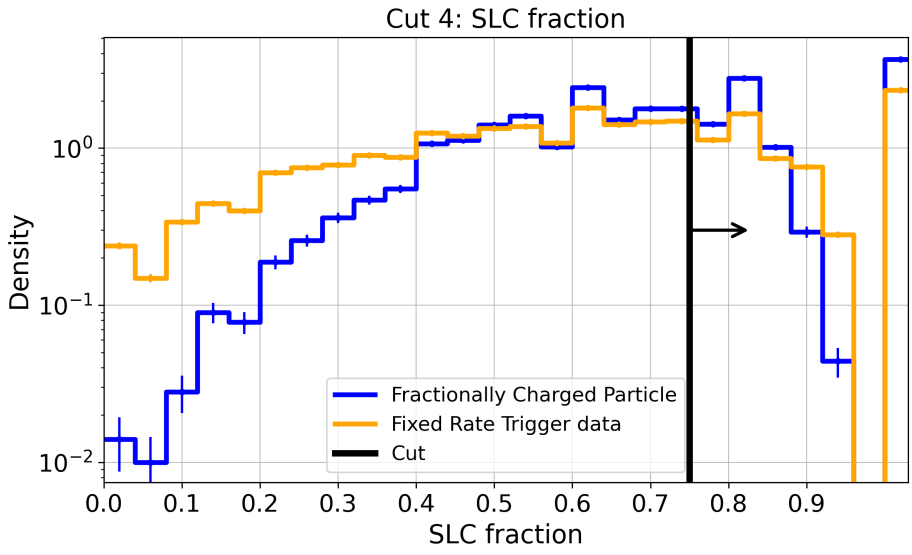

Figure 5.9: SLC fraction distribution for FCP and FRT data
The SLC fraction is shown for FCP (blue) and FRT data (orange). The black line indicates the cut value and the arrow the region that is kept.

cut. The remaining detector noise in the FRT data will dominantly cluster at SLC fractions of one. The adjustment of the cut to the SLC fraction being larger than 0.75 is explained in Figure 5.10. The variation of the threshold is shown on the x-axis. One can observe that the signal efficiency on the FCP simulation decreases rapidly when applying the FPT to them (dashed blue). Nevertheless, the combined signal efficiency (solid blue) is stable up to a value of 0.75. Thus, FCP events in the SLC fraction region 0.6 - 0.75 are mostly already covered by the standard triggers. This shows that additionally triggered events by the FPT typically have a high SLC fraction above 0.75. Setting the threshold to >0.75 reduces the FPT rate to approximately 100 Hz (dotted red) after the fourth cut. 87 % of the signal events survive all four cuts (Figure 5.12).

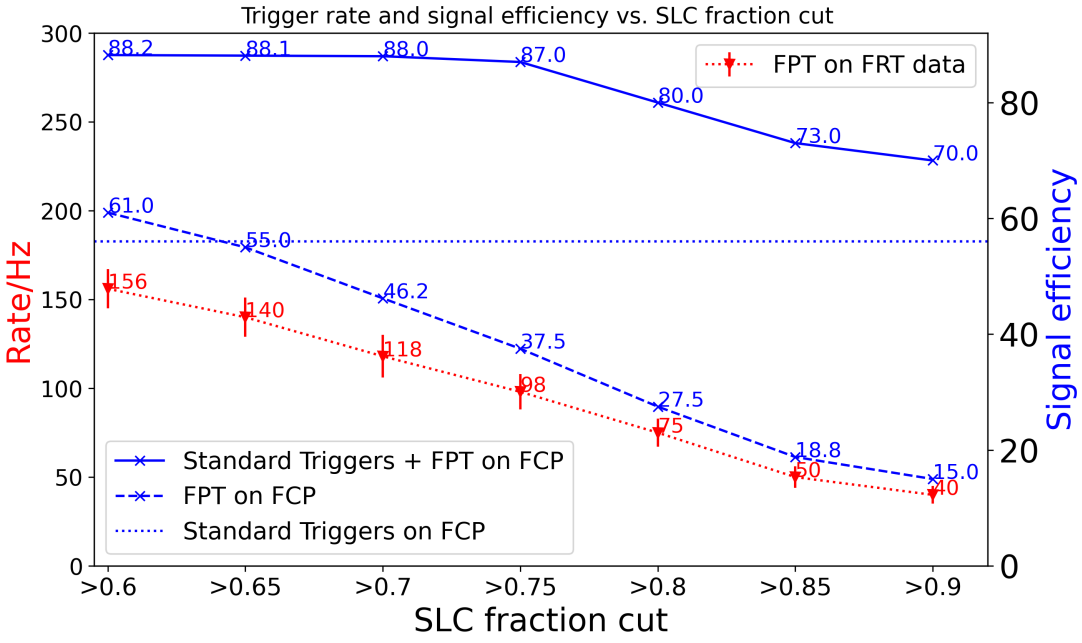

Figure 5.10: SLC fraction cut optimization

Shown are the estimated FPT trigger rate (dotted red), the standard trigger efficiency on FCP (dotted blue) as a reference, the FPT trigger efficiency on FCP (dashed blue) and the combined trigger efficiency of the standard triggers plus the FPT on FCP (solid blue).

5.1.6 Variation of the time window separation parameter

To evaluate how much the time window separation influences the result it was varied between 200 to 2500 ns. The signal efficiency decreases with an increasing time window spacing. A value of 800 ns was chosen to satisfy in order to keep the trigger rate around 100 Hz and because no significant amount of signal efficiency is lost at this point compared to lower values.

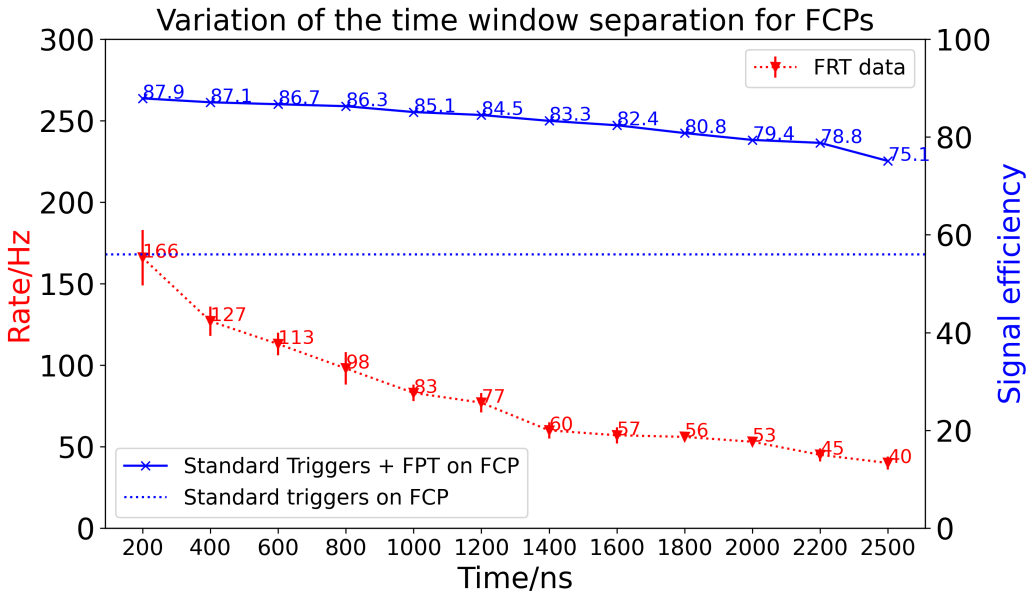

Figure 5.11: Variation of the time window separation *s*
The variation of the time window separation is shown. For each value, the corresponding blue lines show the signal efficiency from applying the standard triggers (dashed) and standard triggers plus the FPT (solid) on FCP simulation. The dashed red line shows the estimated FPT rate, derived from applying the FPT to FRT data.

5.1.7 Summary of cuts and results

The impact of each cut on the signal efficiency, detector noise rate, and the estimated trigger rate is summarized in Figure 5.12. After applying the fourth cut, 87% of the signal events are retained (solid blue), representing a relative improvement of 1.55 compared to the standard triggered events. It can be observed that the contribution from detector noise is reduced to approximately a few Hz after the third cut (solid red).

The fourth cut does not significantly further reduce the noise contribution, because detector noise predominantly produces SLC hits. On the other hand, the estimated FPT rate (dashed red) is reduced by an additional factor of three by the fourth cut. This suggests that the fourth cut is particularly effective in removing atmospheric muons, which typically produce events with a lower SLC fraction compared to FCP. The trigger was applied to existing data sets of electron, muon and tau neutrino simulation in DC. The relative improvements are shown in Table 5.1. The largest improvement of 1.18 can be found for electron neutrinos between 4-12 GeV. A complete list of the

Flavor & energy	Relative trigger efficiency increase
$\nu_{e,A}$	1.11 ± 0.02
$\nu_{e,B}$	1.18 ± 0.02
$\nu_{e,C}$	1.10 ± 0.01
$\nu_{\mu,A}$	1.11 ± 0.02
$\nu_{\mu,B}$	1.10 ± 0.01
$\nu_{\tau,A}$	1.14 ± 0.02
$\nu_{\tau,B}$	1.15 ± 0.01

Table 5.1: Relative improvements for neutrino simulation

Relative improvements above 1.03 for neutrino simulation in DC resulting from including the FPT. The energy intervals are: A(1–4 GeV), B(4–12 GeV) and C(12–100 GeV).

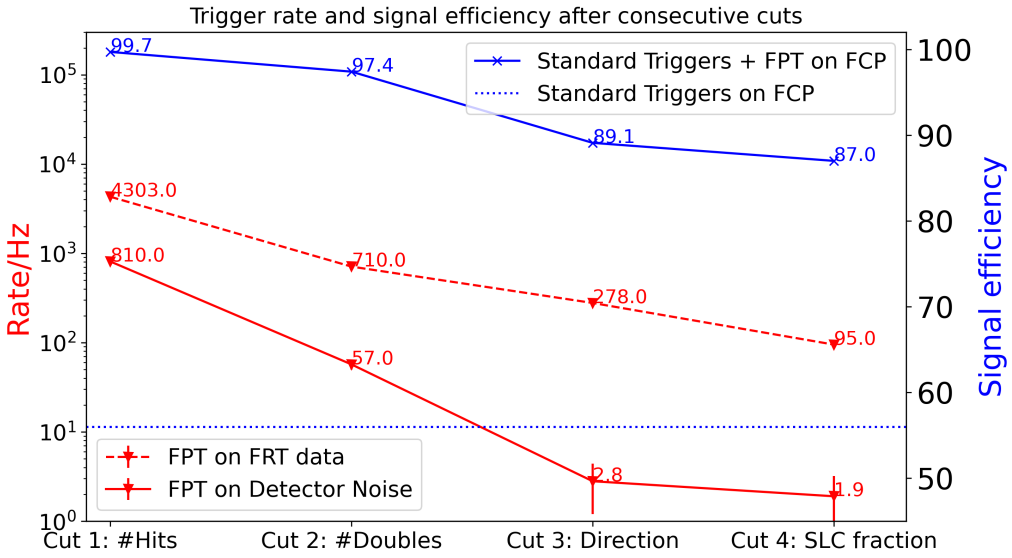

Figure 5.12: Summary of Cuts

Cuts are applied consecutively. For each cut, the corresponding rates and signal efficiencies are shown. The blue lines show the signal efficiency from applying the standard triggers (dashed) and the standard triggers plus the FPT (solid) on FCP simulations. The red lines show the estimated FPT rates, derived from applying the FPT to detector noise simulation (dashed) and FRT data (solid).

trigger parameter settings is shown in Table 6.1. The FPT DC version corresponds to the one that is deployed at IceCube.

5.2 Faint Particle trigger full detector and IC79 versions

A FPT version that operates on all IceCube PMTs was developed but not deployed at the South Pole. This full detector version shares the same structure as the DC version, albeit with different parameters and cut values. Compared to the DC version, the input hit rate to the trigger system increases by a factor of 4.5, reaching up to 2.7 MHz.
Given that it was initially uncertain whether this rate could be processed by the sorting algorithms, a method was developed to reduce the hit rate while enhancing the signal-to-noise ratio. Multiple full detector versions were created. However, all of these encountered conflicts with the limitations imposed by the current satellite bandwidth. Applications to extend the bandwidth have frequently been submitted, with no success so far. Consequently, this limitation remains an external boundary condition.

5.2.1 Input hit rate reduction

To reduce the input hit rate, a method using the timing characteristic of the PMT noise to cut out noise hits was developed. As can be seen in subsection 3.4.1, different noise contributions manifest at different time scales when comparing time differences between consecutive hits on the same DOM. A characteristic feature is that the uncorrelated radioactive decay component of potassium-40 is followed by a burst of noise hits as described in subsection 3.4.1. When counting the number of hits on each DOM over a specified time period, the probability of producing more than one hit increases due to the burst-like nature of the correlated noise component. In contrast, when examining the hits produced by FCPs, predominantly SLC hits are generated, and typically only one hit per DOM occurs. The reduced photon emission associated with FCPs favors the production of exactly one signal hit per module, which stands in stark contrast to the burst behavior of the noise component.
To leverage this characteristic for noise reduction, the number of hits per DOM is counted within a specific time window. If a DOM registers exactly one hit during this time window,

it meets the condition, and the hit is forwarded. This method is referred to as "isolated DOMs". Given that the time scale extends up to milliseconds, the vuvuzela module described in subsection 4.1.3, which was designed for relativistic signatures, cannot be applied in this context.

For searches for sub-relativistic monopoles in IceCube, a suitable tool for generating background was developed specifically for the dedicated SLOP trigger [79]. While this tool accurately models the HLC distributions, it does not account for SLC hits. Including SLC hits would necessitate significant effort and result in extensive computational demands [79].

To accurately describe the hits on this time scale, a different approach was adopted. The FRT data are recorded in snippets of 10 ms. The relativistic FCP signature is inserted into a random FRT data frame at a position between 6 and 8 ms. For this purpose, the FRTmerger [80] was adjusted to suit this simpler use case. The lower bound of 6 ms was selected to enable verification of the method up to a 3 ms time window. The upper bound of 8 ms was chosen to prevent edge effects that may occur at the end of the FRT frames. In cases where a signal hit conflicts with the readout times of the ADCs, the signal hit is prioritized.

The effect of this method on the input hit rate to the trigger system and the surviving signal hits was analyzed using the FCP signature in the FRT snippet. For signal and noise there are two competing effects. For the signal with a longer time window, the chance increases for a noise hit to occur on the module. For the Detector Noise, a hit followed by a burst of correlated hits has to occur and the probability for that increases with time. This time window was ranged and can be seen in Figure 5.13. The left y-axis shows the hit rate, corresponding to the input hit rate to the triggering system. If no cut is applied, this is at ≈ 2.7 MHz. The blue line shows the signal hits surviving this condition in percent. When observing only the signal hits distribution we can see that for a value of 10 µs still 98% of the signal hits are kept. One would only expect extremely scattered photons to arrive on the same PMT after such a long period of time. Thus, one can conclude from this first point that around 98% of the signal hits are isolated hits. One can see that if a time window of 100 µs is chosen and only the hits of DOMs that were hit exactly once in that

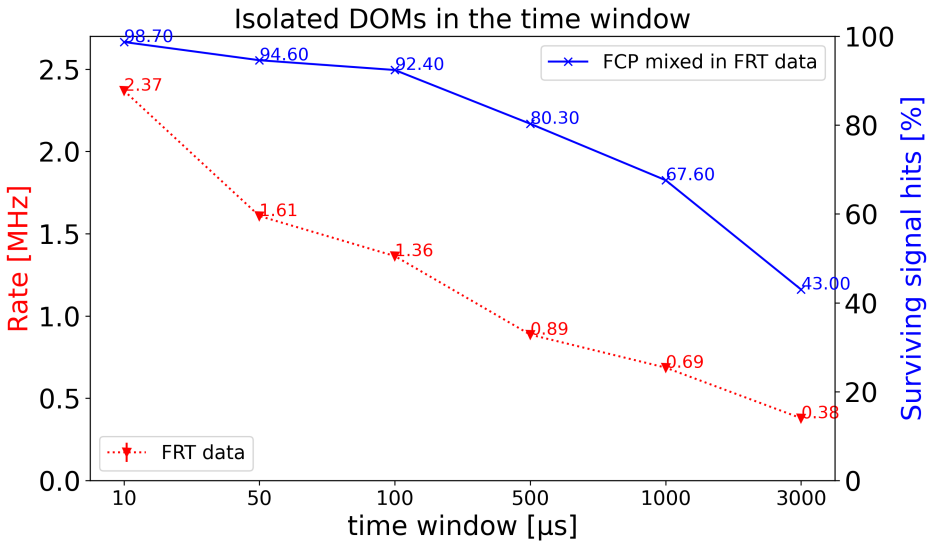

Figure 5.13: Isolated DOMs method
The variation of the time window is shown on the x-axis. The input hit rate (red) and the surviving percentage of signal hits (blue) are evaluated by applying the method to FRT data and FCP simulation.

time window, the hit rate is reduced 1.36 MHz and 92% of the signal hits survive. One can also observe when choosing larger time windows the survived signal hits efficiency decreases. Here it becomes more probable that an additional noise hit occurs. For the FD version discussed below the input hit rate to the triggering system corresponds to all DOMs that were hit once in a 500 µs time window, corresponding to 0.89 MHz.

5.2.2 Isolated DOMs, all hits and IC79 versions

Parameter	Value
largescale_time_window	100 µs
time_window	3000 ns
time_window_separation	800 ns
max_trigger_length	1 ms
hit_min ($\geq$)	5
hit_max ($\leq$)	24
double_velocity_min (>)	10 000 km/s
double_velocity_max (<)	310 000 km/s
double_min ($\geq$)	5
triple_min ($\geq$)	10
slcfraction_min (>)	0.8
domSet	11

Table 5.2: Full detector version (isolated DOMs) parameters
Shown are all parameters for the FPT full detector (isolated DOMs) version. Included is the largescale time window parameter that only exists for this version.

For the full detector version (isolated DOMs) development simulated FCP events were used that leave at least 10 signal hits in IceCube plus DC. The full detector version (isolated DOMs) has different parameter settings compared to the DC version as seen in Table 5.2. One of the main differences is the specification of a largescale time window, which sets the length of the time window in which the DOMs that are hit exactly once are selected. This then allows to scale the input hit rate for the trigger system. Secondly, the time window size is increased to 3000 ns. Furthermore, the isolated hits from all DOMs are forwarded to the trigger system, which is specified by the domSet parameter.

The third cut, which focuses on directional clustering, has been replaced with a new cut, which is called the number of Triples. To calculate the number of Triples, all Doubles are compared to each other. If they share a common middle hit in time, the velocity between the first and last hit of the Double pair is computed. If this velocity meets the same requirement as for the Doubles, the three velocity consistent hits are classified as a Triple and counted. A minimum of 10 Triples is required per time window.

The remaining cuts utilize the same functions, with only the thresholds being adjusted. The number of Triples cut was also tested in the DC version, resulting in a significantly higher rate while maintaining comparable signal efficiency. Conversely, the directional consistency cut for Doubles was also examined in the full detector version, revealing inferior performance compared to the number of Triples cut. This discrepancy is attributed to the more densely instrumented DC volume, where the directional clustering cut proves to be more effective.

The cut variable distributions for the full detector version (isolated DOMs) are shown in Figure A.5 and Figure A.6.

To check if there is an advantage in using all available hits, a full detector version (all hits) using the complete 2.7 MHz input hit rate, was optimized with the Triple cut. In Figure A.7 the summary of the cuts for the full detector (all hits) version can be found.

Lastly, an IC79 version using the IceCube string without the DC strings was created to complement the DC version. For the optimization events that produce at least 10 signal hits in IC79 were selected. In Figure A.8 the summary of the cuts for the IC79 version can be found.

5.3 Comparison of all Faint Particle Trigger versions

The different FPT versions are listed in Table 5.3. The comparison of the two DC versions shows, that they result in approximately the same signal efficiency increase, while the version using the Triple cut produces ≈ 3 times more of additional data, which would correspond to 10% of IceCub's satellite bandwidth. For these reasons the DC version using the Triple cut was discarded.

The full detector version employing the isolated DOMs method demonstrates a notable improvement in signal efficiency gain compared to the DC versions. However, the FPT rate of approximately 400 Hz would result in about 24 GB of additional data per day. This estimate is based on the behavior observed with the DC version using the Triple cut. Such a large volume of data would not be feasible to transmit under the current satellite bandwidth constraints.

The full detector versions using all hits and the IC79 version could potentially employ the vuvuzela module to simulate the background. This method is computationally much faster, offering a substantial advantage compared to the full detector version using isolated DOMs.

The full detector version using all hits suffers from a signal-to-noise ratio that is too low, resulting in ineffective cuts. This leads to the conclusion that methods such as using isolated DOMs are necessary to enhance the signal to noise hits ratio before applying cuts. In Figure 5.14 the summary of the cuts for the full detector (all hits) version can be seen.

The IC79 version was developed around events producing 10 hits in IC79. These events only make a small fraction of the events compared to the rest of the versions that were created around events that also leave hits in DC.

Applying cuts to these is even harder compared to the full detector (all hits) version since these events are in general longer. Therefore, the time window size was adjusted to 5000 ns. The signal to noise hits ratio is thus also very low in this version. Adjusting the cut to have a comparable result in signal efficiency improvement, results in a very large rate. This indicates that for an ε of 1/3, events that do not leave hits in DC are extremely difficult to detect.

This leads to the conclusion that the only realistic full detector version is the one using isolated DOMs, which could be tested and deployed if more data could be transmitted. Alternatively only the hard disks used at Pole could be used for storage. However, this would mean that data could only be analyzed with a delay, and all cleaning, reconstructions, and filters would have to be reapplied before analysis, requiring considerable time and resources.

Version	Input hit rate [MHz]	Cut 3	Relative signal efficiency increase	FPT rate [Hz]	Data increase [GB/day]
DC	0.6	Direction	1.55	95	3.5
DC (triple cut)	0.6	Triple	1.57	177	10
FD (isolated DOMs)	0.9	Triple	1.89	400	≈ 24
FD (all hits)	2.9	Triple	1.57	6580	-
IC79	2.5	Triple	1.52	35505	-

Table 5.3: Comparison of FPT versions

Comparison of two DC versions using a different third cut. Furthermore, three full detector versions are compared. One using the isolated DOMs method to reduce the input hit rate, one operating on all input hits and one operating on IC79.

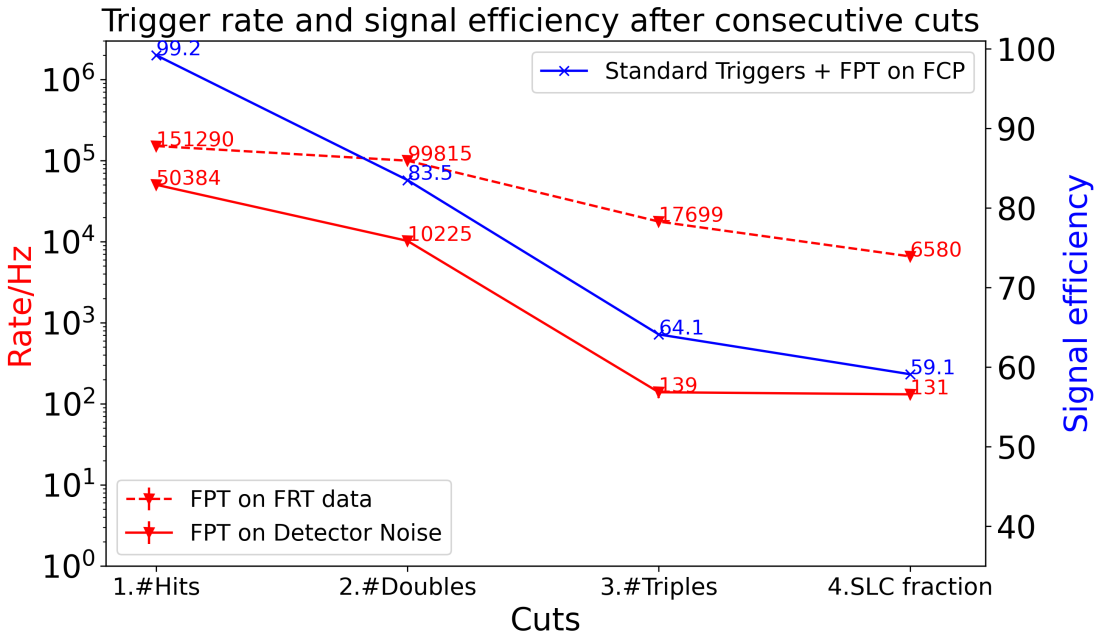

Figure 5.14: Summary of cuts for the FD (all hits) version

Cuts are applied consecutively. For each cut, the corresponding rates and signal efficiencies are shown. The blue lines show the signal efficiency from applying the standard triggers plus the FPT on FCP simulations for the full detector all hits version. The red lines show the estimated FPT rates, derived from applying the corresponding FPT version to detector noise simulation (solid) and FRT data (dashed).

6

Tests and deployment of the Faint Particle Trigger

The FPT algorithm was extensively tested on the SPTS before first test runs at the South Pole System (SPS) were conducted. In this chapter the results of the tests, comparisons of the implementations of the trigger algorithm for the simulation framework and for the SPS and the results of the test runs at the SPS are shown.

6.1 The South Pole Test System

The FPT algorithm is available in the trigger-sim project of IceTray in a C++ version. That framework is used for simulation purposes and events are simulated as described in subsection 4.1.3. A limited amount of time with a start and end point is simulated. In contrast to that at South Pole constantly input hits are forwarded to the trigger system. Furthermore, porting the algorithm to JAVA was required, which is used on the trigger machines of the SPS. The SPTS is the test DAQ of IceCube where new software can be developed and tested. So called replay data (a specific IceCube run that is used for testing purposes) were used to ensure the agreement between the two implementations. FRT data were chosen from the same month of the replay run, resulting in 87.6 s of FRT data. Minor differences are expected, because the FRT data are averaged over the entire month and the replay run represents 8 hours of a specific day. The distributions of the four cut variables were compared, by applying the C++ version to FRT data and the JAVA version to the

replay run on the SPTS.

The distribution for the final SLC fraction cut can be seen in Figure 6.1. The shape of the distribution has the same shape and the maximum bin at an SLC fraction of 1 shows perfect agreement. Minor deviations below 5% are present in some of the events containing HLC hits. These deviations can occur due to the imperfect comparison of two different time periods. More comparison plots can be found in Figure B.1 (and Figure B.2), showing the same level of agreement with no significant differences. This leads to the conclusion that

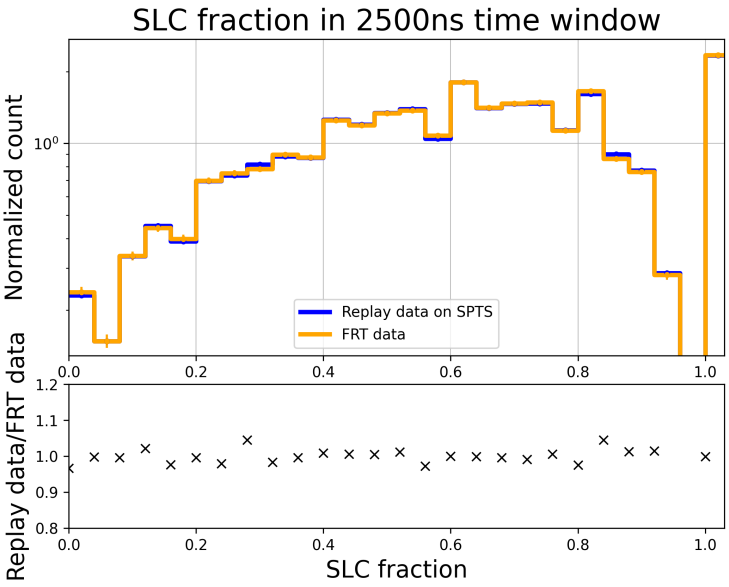

Figure 6.1: SLC fraction comparison (FRT data and SPTS)
Comparison of the SLC fraction of the JAVA version running on the SPTS (blue) and the C++ version applied to FRT data (orange).

both algorithms work identical and minor deviations are caused by the systematic errors of the comparison.

On the SPTS the trigger was tested and improved while frequently applying it to replay runs. This allows to analyze the additional CPU consumption and data increase. The additional CPU consumption stays constantly close to 1% as shown in Figure 6.2. Thus, the trigger imposes only a minimal overhead on computational resources. The trigger operates stable and running it in parallel with the other triggers the event rate is increased by 10 Hz, corresponding to a relative increase of 1.004. The data produced during an 8 h replay run including the FPT results in an approximate increase of about 3 GB per day in data size. The additional data rate of the presented DC version is low compared to the

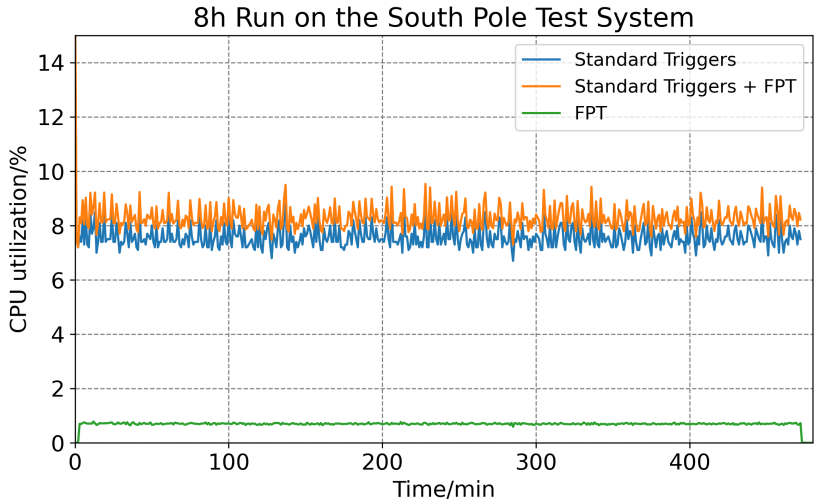

Figure 6.2: CPU utilization of the trigger system
The CPU utilization in % of the Standard Triggers (blue), the Standard Triggers + FPT (orange) and only the FPT (green) are shown.

1 TB of triggered data per day by the standard triggers.

6.2 Test runs at the South Pole System

A first test run (Run138015) for the FPT was carried out on the SPS from 02:30:21 to 02:50:25 on June 6, 2023. The FPT operated smoothly for 20 minutes without any errors, in addition to the standard triggers. The parameters listed in Table 6.1 were utilized during the test. Throughout the run, a total of 3 121 212 events were formed, resulting in a rate of 2592.58 Hz. Among these events, 112 791 were triggered by the FPT, corresponding to a rate of 93.68 Hz. Additionally, 12 056 events were exclusively triggered by the FPT, leading to an event rate increase of 10 Hz. These findings align with the tests conducted on the SPTS.

On September 6 the annual 24 hours test run was taking place. For 24 hours data with the run configuration for the upcoming season are collected. Afterwards these are analyzed and verified by the corresponding working groups. Changes include the new DAQ software release and new triggers and filters.

The FPT was included and 24 hours of data in Run00138329 - Run00138331 were collected. As a comparison all available retriggered (with the C++ version) FRT data from 2012-2015

Parameter	Value
time_window	2500 ns
time_window_separation	800 ns
max_trigger_length	1 ms
hit_min ($\geq$)	5
hit_max ($\leq$)	19
double_velocity_min (>)	10 000 km/s
double_velocity_max (<)	310 000 km/s
double_min ($\geq$)	10
azimuth_histogram_min (>)	4
zenith_histogram_min (>)	4
histogram_binning	20°
slcfraction_min (>)	0.75
domSet	6
readout_window_inice	$\pm$ 6 µs
readout_window_icetop	$\pm$ 10 µs

Table 6.1: FPT trigger parameters
The parameter settings for the FPT running at the SPS. The last two parameters are not specified in the GCD files used in the icetray software framework.

were chosen, resulting in 61.4 minutes of data. These represent the yearly average as compared to the two days at which the test runs took place. Comparing the rates in Table 6.2 one can see an $\approx 8\%$ decrease in the trigger rate, comparing the yearly average estimated by the FRT data and the runs in June and September. From previous analysis of the impact of seasonal variations on the trigger rate a $\pm$ 10% effect on the trigger rate compared to the average is expected [74]. The lowest trigger rate is expected in July, when the averaged atmospheric temperature is coldest and highest trigger rate in January, when the average atmospheric temperature is warmest. Thus, this rate comparison agrees with the expectation.

Data	Rate/Hz
Run138015	93.69 $\pm$0.28
Run138329 - 138331	93.85 $\pm$0.03
FRT data	101.67 $\pm$0.016

Table 6.2: Test runs and FRT data FPT rates
Shown are the FPT rates for the 2023 test runs: the 20 minutes run (top) and the 24 hours runs (middle). The FRT data rate (bottom) corresponds to one hour of data.

The transmitted events can be analyzed by reapplying the calculation of the trigger variables. Due to the fact that the trigger window, created for each event satisfying the cuts, is defined by the time of the first and last hit in the window, the exact position of the sliding time window is lost. These are defined by the starting time of each new run (every 8 hours), at which the first time window is placed at the occurrence of the first hit and consecutive ones start every 800 ns.

As a result, what the trigger evaluated in real-time at the South Pole cannot be fully reconstructed. However, this is not crucial because the trigger only analyzes a single time window at any given moment. Once transmitted, the complete built event, which includes hits from the readout window centered around the trigger window, is available for analysis, as described in section 3.5. Thus, post-transmission analysis is more comprehensive, and the trigger itself has no knowledge about the entire event.

The trigger variables can be recalculated by applying the appropriate functions to the DC hits. For instance, a comparison of the number of hits and the SLC fraction is shown in Figure 6.3. It can be seen that the shape of the number of hits (#Hits) distribution agrees in the peak regions, with a slight excess observed in the FRT data, likely due to averaging over the entire year. The tails of the distribution, however, show that shorter data periods have less statistical significance. Additionally, events with very high hit counts in DC are visible in the tails, typically corresponding to events with multiple triggers, where the Faint Particle Trigger (FPT) fired at the very beginning or end of a bright event. These events will undergo further analysis by the Faint Particle Filter, discussed in chapter 7.

Similarly, the SLC fraction shows consistent behavior across datasets. The 2023 data nearly perfectly overlap with the FRT data, though the FRT data averaged distribution is slightly skewed toward higher SLC fractions. In Figure 6.4 the trigger lengths are shown. The structure of the distributions agree as well. The shape of the distribution confirms the correct sliding time window behavior, which has a size of 2500 ns and is placed every 800 ns. The rapid decreases towards lower trigger lengths appear in steps of 800 ns after the 2500 ns peak. This is expected, because triggering more consecutive time windows becomes more unlikely. Distributions of the other trigger variables can be found in Figure B.3, showing the same level of consistency.

In conclusion, the test runs were successful and demonstrated consistent behavior across all evaluated trigger variables. This comparison reinforces the consistency between the two implementations of the trigger algorithm. The successful tests ultimately led to the approval of the Faint Particle Trigger (FPT), which was successfully deployed at the South Pole on November 28, 2023.

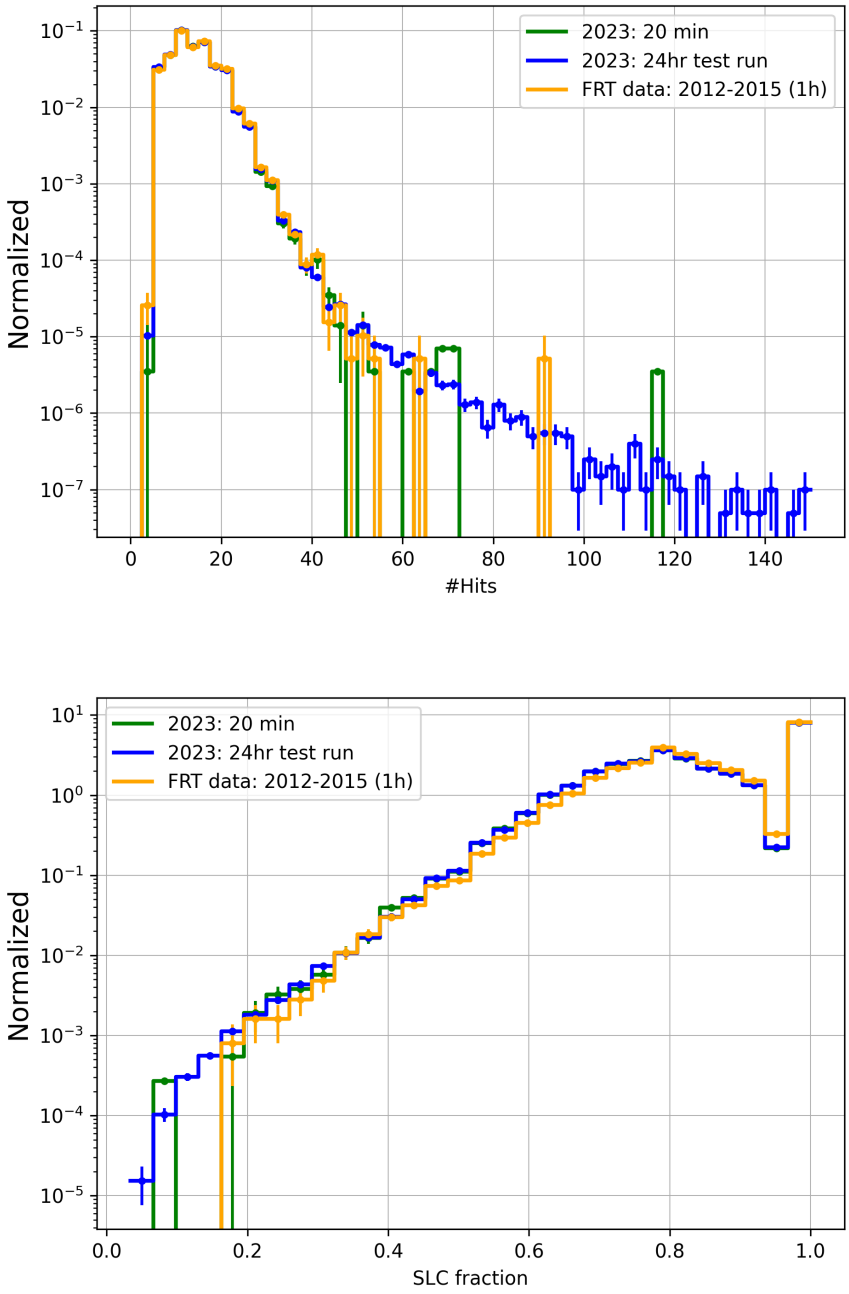

Figure 6.3: #Hits and SLC fraction for test run data.
The number of hits in the event (top) and the SLC fraction (bottom) of the event are shown for FRT data (orange), the 20 min test run in 2023 (green), and the 24 hours test run in 2023 (blue).

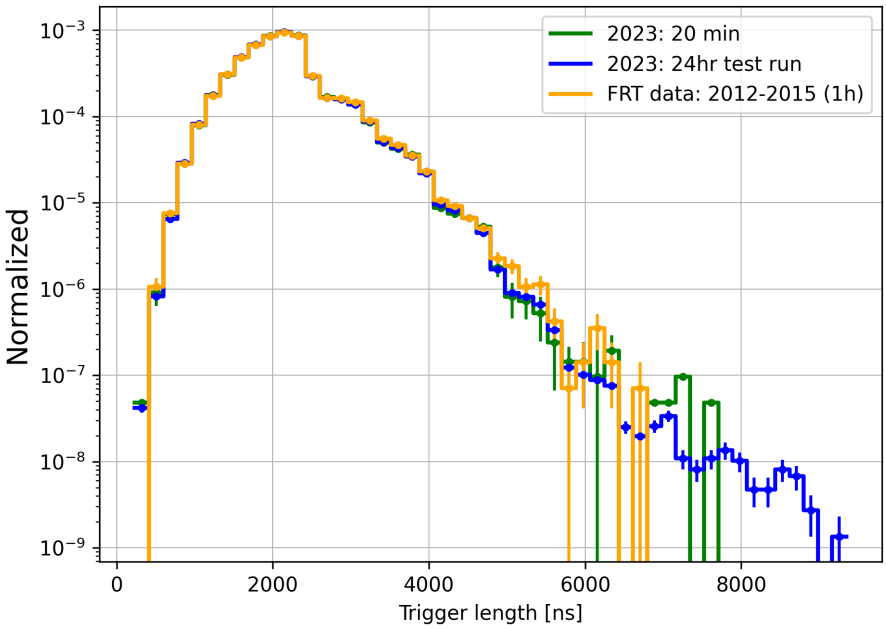

Figure 6.4: Trigger length for test run data
The trigger length for the events is shown for FRT data (orange), the 20 min test run in 2023 (green) and the 24 hours test run in 2023 (blue).

6.3 The Faint Particle Trigger rate trend

In Figure 6.5, the rate of the FPTduring the first eleven months of data collection is presented, showing rates approximately between 94 to 108 Hz. This results in an average rate of approximately 101 Hz, which aligns with the averaged FRT data in Table 6.2. The rate trend shows the same seasonal variation as are observed in other triggers [74].

This is caused by the density varying of the atmosphere with the changing temperature. In the warmer months at South Pole (around January) the atmosphere is taller and less dense. The produced kaons and pions (see section 2.7), by a CR interaction in the high atmosphere, have a higher probability to decay to muons than to interact with atmospheric oxygen or nitrogen. In the colder months (around July), interaction is favored due to the denser atmosphere, resulting in a lower amount of muons.

Given that the FPT rate is dominated by events with multiple triggers, with approximately 10% of the rate corresponding to additional triggered events, this trend is expected. In future the trend of the additional triggered events by the FPT, after applying algorithms to reduce noise contributions, could be analyzed.

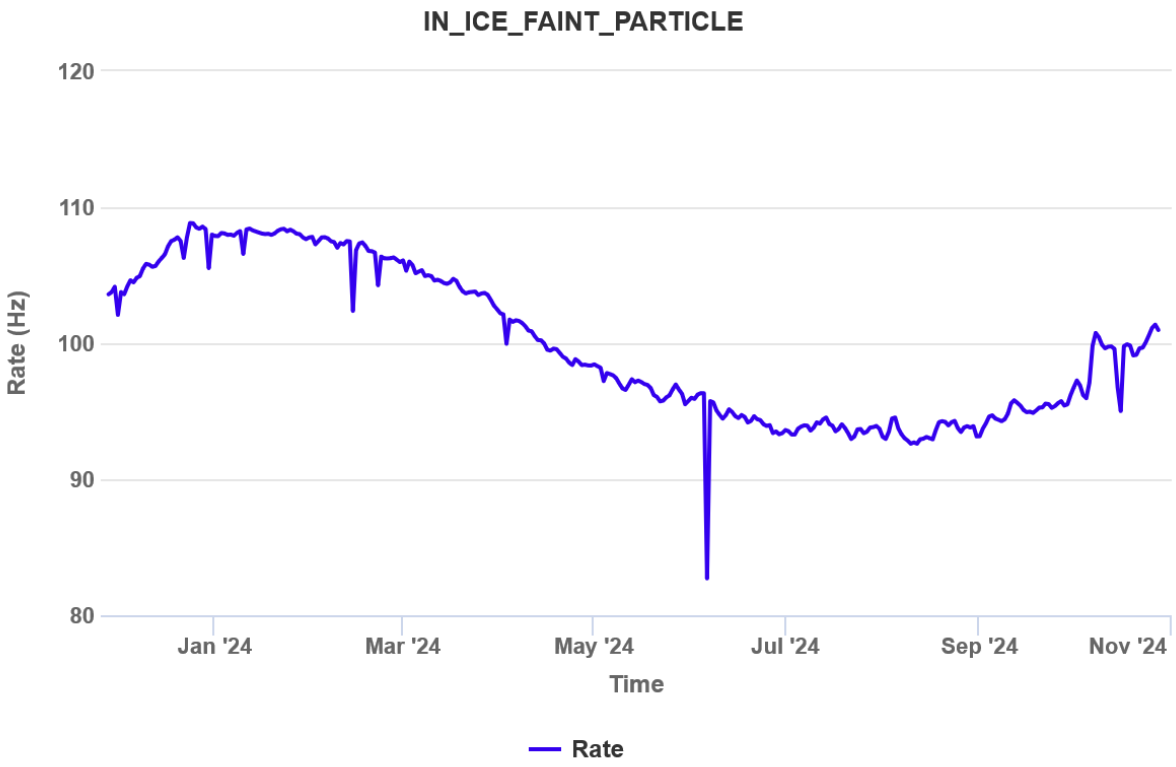

Figure 6.5: FPT rate for the first 11 months of operation
The rate development of the FPT during the first 11 months of operation is presented. Large dips in the rate correspond to short maintenance periods when the detector was offline.

7

The Faint Particle Filter

This chapter describes the Faint Particle Filter (Figure 7.1), which was developed to reduce the FPT rate that is dominated by atmospheric muons. The same event sample that was used to develop the FPT (described in section 5.1) was used to develop the FPF. The FPF reduces the 100 Hz FPT rate to ≈ 8 Hz while keeping 85% of the triggered signal events, including ≈ 96% of additional triggered events by the FPT.

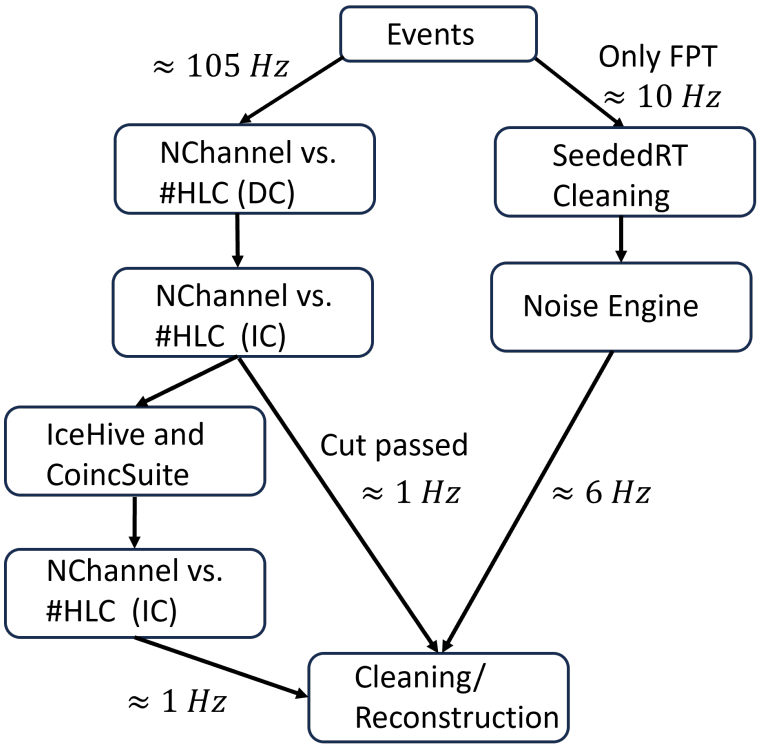

Figure 7.1: Faint Particle Filter overview
Schematic overview of the FPF, showing how it splits events into two categories based on their triggers. Within each branch different cuts and cleaning algorithms are applied.

7.1 The Faint Particle Filter algorithm

Unlike the FPT, which operates in real-time at the South Pole, the FPF processes events offline, transmitted via satellite. While the FPT is limited to analyzing DC hits in the time window with fixed length, the FPF can analyze the built event, which may consist of multiple triggers from the entire detector. Thus, signatures appearing faint to the FPT may consist of outlier hits from a bright signature in IceCube. An example of such an event can be seen in Figure 7.2. This is a simulated down-going muon, triggered by the FPT due to the few SLC hits produced in DC. The FPT fires at the very end of the event.

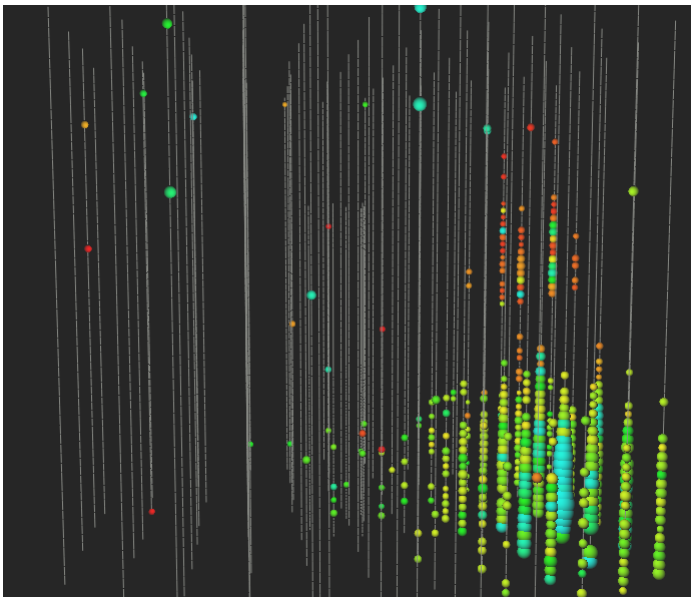

Figure 7.2: Simulated muon triggered by the FPT
A simulated muon is shown. The color encodes the time of the hits from early (red) to later (green) times. The muon produces a bright signature in IceCube and leaves few hits in DC, which the FPT triggers.

7.1.1 Input to the Faint Particle Filter

The processing of triggered event is described in section 3.6. All events that were triggered by the FPT are forwarded to the FPF. Additionally, events forwarded by the new DC online filter, are now analyzed by the FPF, as a significant fraction of FCP events is lost by the new DC offline filter. The FPF splits the events in two classes: events triggered exclusively by the FPT and those captured by multiple triggers as seen in Figure 7.1.

7.1.2 The only FPT branch

For events triggered exclusively by the FPT, IceCube is dim, with only a few hits detected in DC. Within the rate of ≈ 10 Hz two dominant contributors occur: Detector Noise and low-energy muons. The primary goal for this branch of the FPF is to identify and filter out Detector Noise frames. To achieve this, first a standard cleaning algorithm is applied to the hits. Afterwards, the NoiseEngine module [69] is employed.

The seededRT cleaning algorithm processes a list of input hits and a seed, radius and time parameters can be specified. A dedicated master thesis compared different cleaning algorithms and found that, for SLC-dominated events within this branch, the AllCoreHits seed yields the best results [78]. In this context, core refers to a hit that satisfies a parameterized radius and time condition. The RT parameters are set to 150 m and 1000 ns, meaning that a second hit must fall within the specified time and radius range to fulfill the condition. Hits that meet these criteria serve as seeds. The algorithm then iterates over the remaining hits, checking if each hit also satisfies the RT conditions. If a hit fulfills the condition, it is added to the seed list; otherwise, it is discarded.

The cleaned hit list serves as an input for NoiseEngine. It was designed to classify a hit list as either noise or signal. NoiseEngine takes several input parameters: a time window length, velocity bounds (v_{min} and v_{max}) and a threshold. It constructs all hit pairs within the specified time window and counts those with velocities falling within the $[v_{min}, v_{max}]$ interval. If the number of qualifying pairs exceeds the threshold, the hit list is classified as signal.

This module is also utilized in the LOWEN and ELOWEN samples [81], designed to retain neutrino events with energies between 0.5 MeV – 1 GeV and 1 GeV – 5 GeV, respectively, by employing multiple parameter sets. The initial settings for v_{min} and v_{max} in this analysis closely follow those used for the ELOWEN sample's looser cuts, with $v_{min} = 0.2$ m/ns and $v_{max} = 0.9$ m/ns. For the parameter scan, v_{min} was set to 0.1 m/ns and v_{end} was set to 1 m/ns. The subsequent analysis examines the effects of varying the time window length and threshold. Reducing the velocity interval requires lowering the threshold for a fixed time window to maintain consistent results. A broad velocity interval was chosen to explore a wider range of time window and threshold combinations. The resulting rates for the

FPT-only branch of the FPF are shown in Figure 7.3. At a fixed threshold value the rate increases with a larger time window size, because more hits are expected in a larger time window. For a fixed time window size the rate decreases with an increasing threshold, because the same amount of events is expected and stricter cut applied. This allows for multiple options at different combination points.

The goal for each filter is to reduce the rate as far as possible to the few Hz regime. Since the "only FPT" branch corresponds to the additional triggered events, this part is the most important one of the FPF. The goal is to keep more than 95% of the additional triggered FPT events, while reducing the FPF rate as much as possible. The efficiency for the events exclusively triggered by the FPT, is shown in Figure 7.4. The combination of time window and threshold is written as (250,0) for a time window of 250 ns and a threshold larger than 0. Saving more than 95% of the FCP events offers possibilities at (200,0), (350,1) and (750,2), each corresponding to the lowest rate of the row. The lowest rate of $\approx$ 5.5 Hz of the three options is the one for (750,2).

The efficiencies for the additionally triggered electron neutrinos with energies between 4-12 GeV, for which the FPT showed the largest improvement are shown in Figure C.2. The efficiencies for the other flavors and energy ranges are shown in Appendix C. For all flavors and energies, there is an improvement of at least 1% increasing the time window from 750 ns to 800 ns. With increasing time windows that improvement decreases for most of the neutrinos. Thus, the final parameters for the noise engine module were adjusted to (800,2), resulting in a approximately 5.5 Hz FPF yearly average rate from this branch.

7.1.3 Multiple triggers/DC branch

For the branch of events with multiple triggers, including those triggered by the FPT or those that passed the DC online filter, two to three cuts are applied to eliminate different types of events, which are explained in the following.

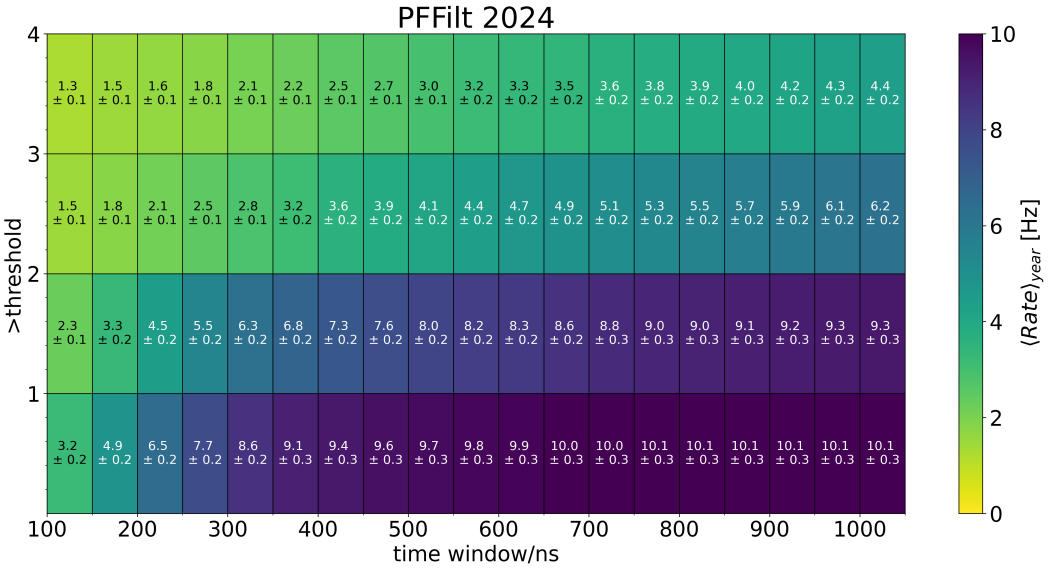

Figure 7.3: Only FPT branch rate after NoiseEngine

The FPT rate of the only FPT branch for different combinations of the time window length and threshold parameters of the NoiseEngine module. 139.8 s of PFFilt data from January 2024 were used.

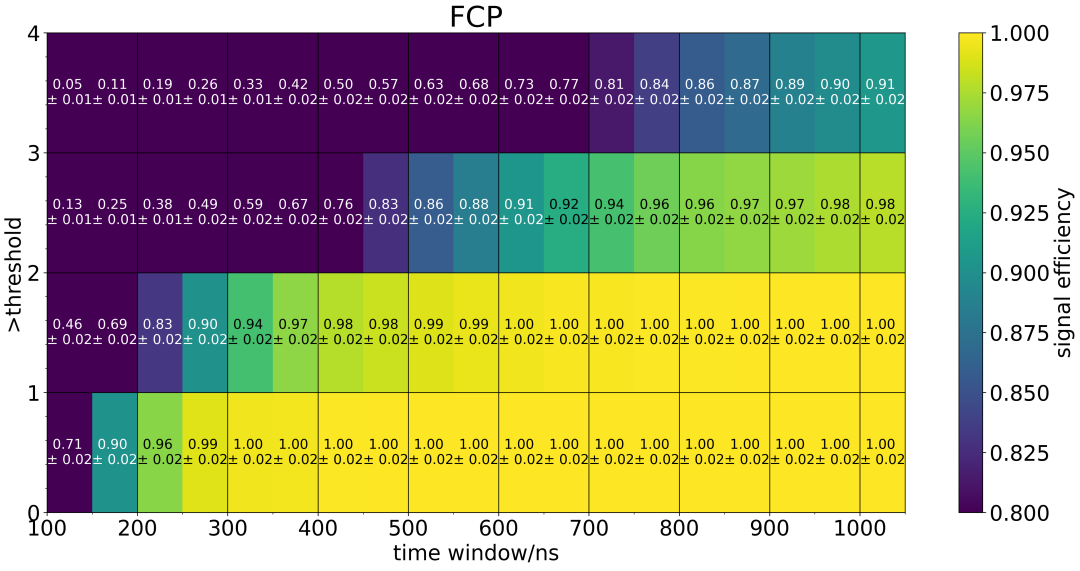

Figure 7.4: Only FPT branch FCP after NoiseEngine

The FCP signal efficiency of the only FPT branch for different combinations of the time window length and threshold parameters of the NoiseEngine module.

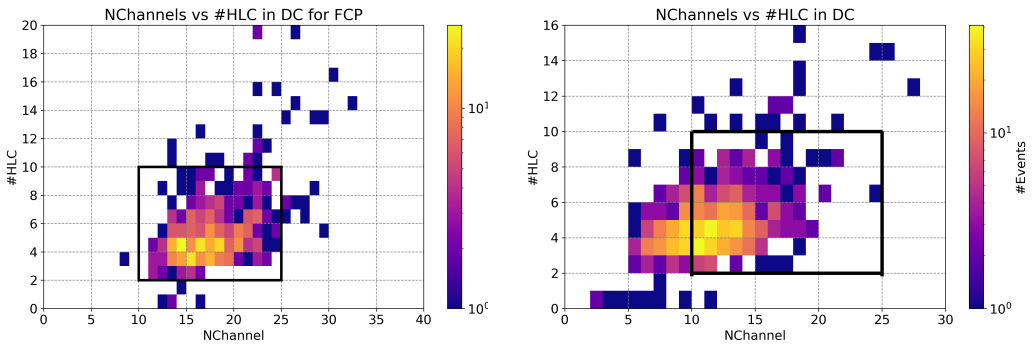

Figure 7.5: NChannel vs. #HLC cut for FCP
NChannel vs. #HLC cut for FCP of events with multiple triggers including the FPT (left) and events that passed the DC online filter and do not pass the DC offline filter (right). The black boxes indicate which events are kept by the cut.

7.1.4 NChannel vs. #HLC Cut in DC

As the signatures of interest are relatively dim, it is essential that the entire DC region remains dim during the event. For a significant fraction of events with multiple triggers, the FPT may only trigger a of the small fraction of the event at the beginning or end. Therefore, all hits of the event are considered, and a cut based on NChannel versus #HLC hits in DC is applied. Here, NChannel corresponds to the number of unique DOMs that produce at least one hit in the event. This cut is also employed by other low energy filters, such as the DC and ELOWEN filters. The 2D histograms for FCP events with multiple triggers, including those triggered by the FPT and those that either pass or do not pass the DC offline filter, are shown in Figure 7.5. The histogram for events that pass the filter shows a peak of #HLC in DC at 4. The additional trigger associated with the FPT is likely the DC trigger. In contrast, the additional trigger for events with fewer than three HLC marked hits is based on an IC trigger.

Events with a low number of HLC hits in DC are of particular interest, primarily found in the only FPT branch of the FPF. To retain most of the remaining low HLC events while satisfying rate requirements, the lower threshold for this cut was set to 2. The maximum threshold for #HLC in DC was established at 10, covering over 95% of events with multiple triggers, including the FPT. The lower NChannel threshold is based on the events that do not pass the new DC offline filter (Figure 7.5, right). This corresponds to approximately 15% of the events in the sample. Notably, 60% of these events can pass the FPF with a

lower threshold on NChannel of 10. Further reduction of this threshold would conflict with the rate requirements. In Figure 7.6 (left), the thresholds for all FCP events entering this branch of the filter are shown. The signal sample includes all events that pass the DC online filter, and a certain fraction of these will also pass the DC offline filter. By applying these cuts, 85% of the signal events survive this step, reducing the rate to approximately 29 Hz. The PFfilt data correspond to 139.8 seconds of data collected on January 5, 2024 (Figure 7.6, right). This duration represents a typical length for a subrun file and was utilized for developing cuts during the filter's development. The combined results of the two branches of the FPF are presented in section 7.2.

7.1.5 NChannel vs. #HLC cut in IC

To further reduce the rate from this branch, the next cut on NChannel versus #HLC in IceCube (IC) is applied. Since the event is dim in DC, there remains the possibility that it could be bright in IC. In the signal distribution shown in Figure 7.7 (left), it is evident that most of these events do not produce a significant number of HLC hits in IceCube. Therefore, a threshold is set for a maximum value of HLC hits in IC at 4, and a maximum NChannel in IC is set at 37. With this cut, approximately 98% of the remaining signal events are retained within the area of events directly kept by the filter. The corresponding rate of events that directly pass the filter at this point is about 1 Hz. Events that do not meet these thresholds are not directly rejected. At this stage, it is confirmed that DC is substantially dim. However, if IC is bright, there remains a possibility of coincident

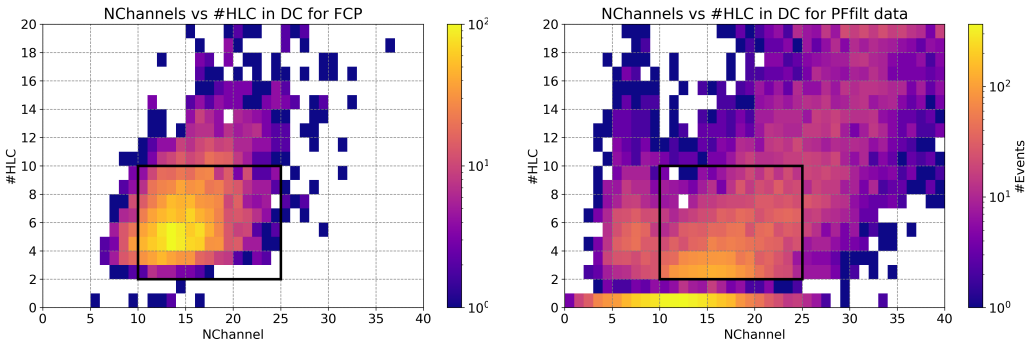

Figure 7.6: NChannel vs. #HLC cut in DC
NChannel vs. #HLC cut of events with multiple triggers including the FPT or events that passed the DC online filter for FCP (left) and PFfilt data (right). The black boxes indicate which events are kept by the cut.

signatures in both IC and DC. In the unlikely event of overlapping signatures occurring closely in time, the trigger splitter module used in the standard processing chain exhibits limited separation capability. Consequently, for the remaining approximately 28 Hz of events that do not pass the cut, a more sophisticated module is applied to distinguish coincident signatures that overlap closely in time.

7.1.6 IceHive and CoincSuite

The event sample used for evaluating the previous steps of the filter does not include coincident signatures. Thus, a new sample was created for which a high energy muon event in IC was mixed with an FCP that is only triggered by the FPT. The muon event triggers the FPT and has an additional trigger. Furthermore, the event satisfies the NChannel vs. #HLC in DC and does not pass the NChannel vs. #HLC in IC cut. Such an event can be seen in Figure 7.2.

To simulate a more complex scenario, an FCP signature, triggered exclusively by the FPT was mixed into the muon event. Only the FCP's signal hits were included to avoid overestimating the Detector Noise already present in the muon event. Such a simulated coincident event can be seen in Figure C.1. Different time offsets to the FCP signal hits were chosen to characterize different gaps between the signals. Three scenarios were created: the FCP before the muon, simultaneous to the muon and the FCP after the muon. As each signal event corresponds to a time distribution of signal hits, the gap length depends on the definition of how the difference between the distributions is quantified. The different scenarios

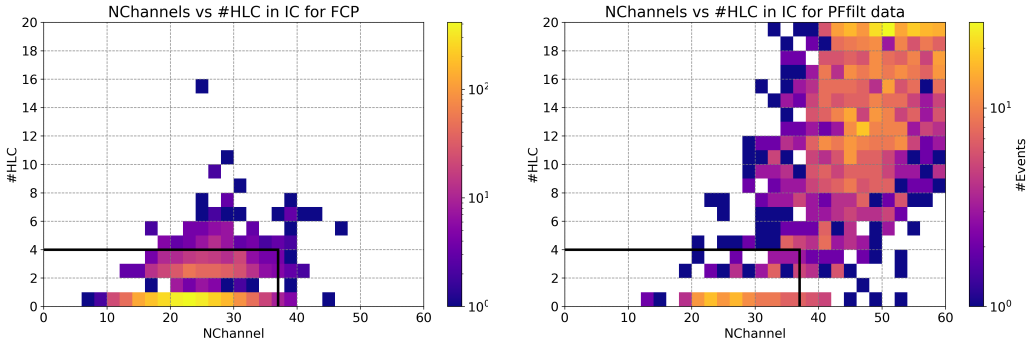

Figure 7.7: NChannel vs. #HLC cut in IC
NChannel vs. #HLC cut in IC for FCP (left) and FRT data (right). The black boxes indicate which events are kept by the cut.

require different methods. The gap between simultaneous signals is best quantified by taking the mean of the distributions. When there is a large gap between the two signals it is more correct to use a high percentile of the first signal hit times distribution and a low percentile of the second signal hit time distribution. Optimal percentiles were adjusted for each different offset time by using the TriggerSplitter module. The TriggerSplitter analyzes how far apart the triggers in each event are. If there is a gap larger then 10 µs it splits the event in two events. Thus, by using this module a gap of 10 µs can be found.
The TriggerSplitter module is part of the standard processing chain, but cannot disentangle coincident signatures occurring simultaneously in different regions of the detector. To address this limitation, a combination of the IceHive and CoincSuite modules was employed. Previously, the HiveSplitter (the precursor to IceHive) and CoincSuite were used in a similar FCP search within IceCube. The performance of the combination of IceHive and CoincSuite is compared to that of the TriggerSplitter, which is already part of the standard processing chain but has limited ability to resolve coincident signatures. Due to time constraints in developing the new filter, and the complexity of configuring the HiveSplitter and CoincSuite modules, both were used with standard settings, as in the previous analysis [32].

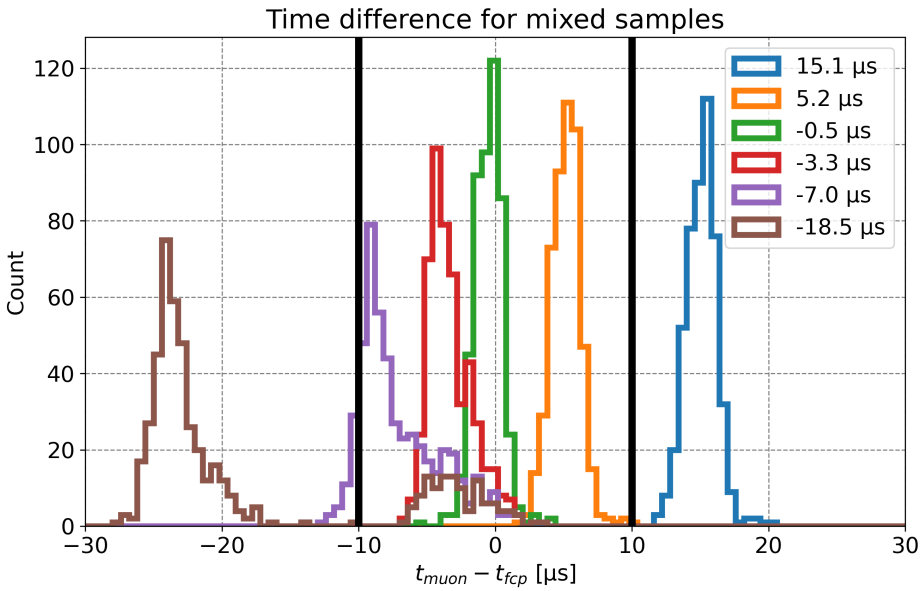

Figure 7.8: Time differences of mixed FCP and muon simulation
Time difference of muon and FCP signature for different time offsets. The black lines show the border in between which the TriggerSplitter can not disentangle coincident signatures. The legend shows the mean value for each distribution.

The time differences between the mixed FCP and muon signals for various offsets on an event basis are shown in Figure 7.8. Positive values indicate that the FCP leaves a signature before the muon, represented by the orange and blue samples. The blue sample falls outside the 10 µs threshold sensitivity of the TriggerSplitter. Similarly, most of the events in the brown sample, where the FCP signal occurs after the muon, also exceed this threshold. To quantify the improvement provided by IceHive plus CoincSuite, both splitter modules were applied to the event samples, and the number of p-frames produced was analyzed. Ideally, the splitter should return two p-frames: one containing the muon and the other the FCP. The results are summarized in Figure 7.9, where the x-axis shows the number of p-frames created by each splitter module. The TriggerSplitter produces only 1 or 2 p-frames, while IceHive occasionally creates 3 p-frames, indicating over-splitting.

For the solid lines representing TriggerSplitter, it performs well for samples with time differences outside the ±10 µs threshold. In the blue sample, all events are split correctly into two p-frames. As shown in Figure 7.8, some events in the brown sample exceed the -10 µs threshold, leading to 4% of cases where only 1 p-frame is produced. The orange, green, and red samples are correctly handled by TriggerSplitter, producing a single p-frame as expected. For the purple sample, 17% of events are correctly split into two p-frames, but the remaining fraction lies above the 10 µs threshold, as observed in Figure 7.8, which

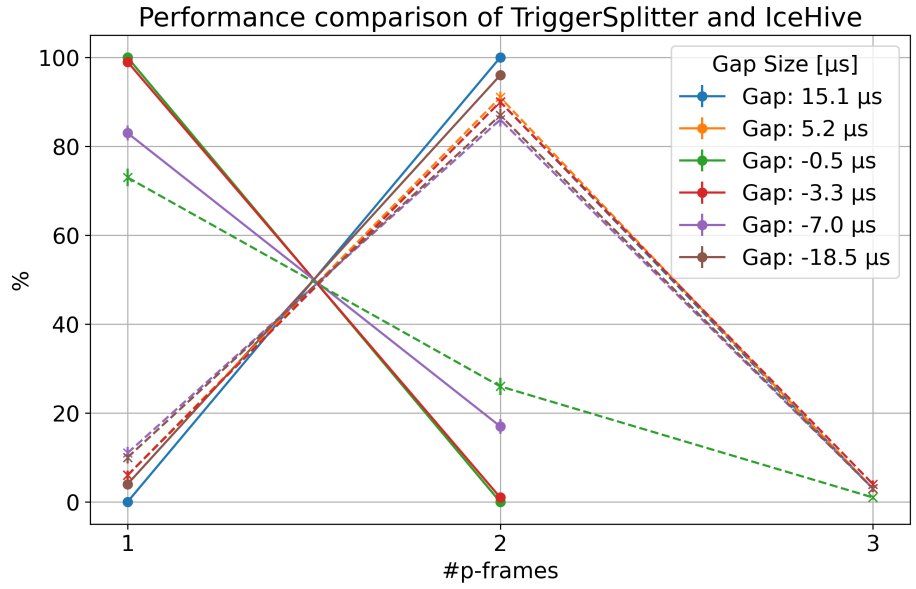

Figure 7.9: Performance comparison of TriggerSplitter and IceHive
Amount of p-frames produced by TriggerSplitter (solid lines) and IceHive+CoincSuite (dashed lines).

aligns with the expected behavior for TriggerSplitter.

The improvement with IceHive plus CoincSuite is evident across all samples. Except for the green sample, where there is near-perfect overlap with TriggerSplitter, more than 80% of the events are correctly split into two p-frames. Thus, the IceHive plus CoinCsuite modules demonstrates a significant improvement in resolving coincident signatures that occur within 10 µs. Therefore, all events that do not satisfy the NChannel vs. #HLC threshold in IC are further analyzed using the IceHive and CoincSuite modules. If more than one p-frame is created, the event is retained. This process reduces the event rate in this stream from approximately 28 Hz to around 5 Hz. Subsequently, the newly produced p-frames are re-evaluated, and the NChannel vs. #HLC in IC cut, as described in subsection 7.1.5, is reapplied. If at least one of the p-frames meets this criterion, the event passes the filter, further reducing the rate to approximately 1 Hz.

7.1.7 Cleaning and reconstruction

In the last step cleaning and reconstruction algorithm are applied to the events surviving the FPF. Different cleaning algorithms and methods to reconstruct the faint signatures were discussed in a dedicated thesis [78]. In Figure 7.10 the cleaning and reconstruction flow is visualized. Events are classified in two categories. If they have less than 3 HLC hits or were only triggered by the FPT they are cleaned with the seededRT cleaning algorithm and AllCoreHits as seed. If the events has more than 2 HLC hits the algorithm is applied with the HLCCoreHits seed. Then fit algorithms are applied with more details in the corresponding thesis [78].

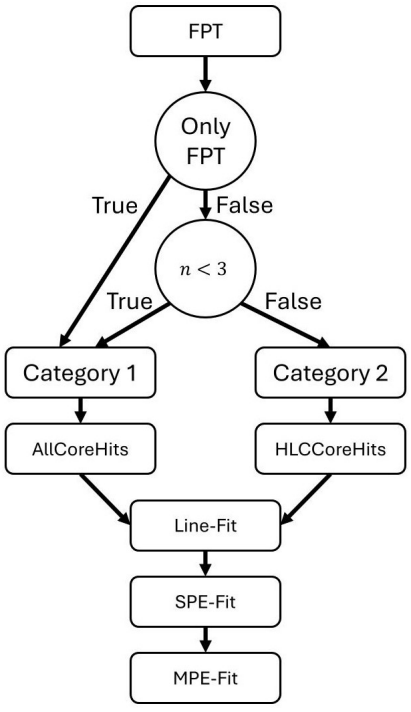

Figure 7.10: Schematic view of the reconstruction chain

Events are classified in Category 1 or 2 based on the HLC hits n and the triggers in the event. Taken from [78].

7.2 Faint Particle Filter results

The filters with dominant signal efficiency for FCP searches will be the DC offline filter and the FPF. The results of applying these two to the FCP event sample, used for developing the FPF, are shown in Figure 7.11. In solid and dashed blue one can see the results when applying the filters individually. The FPF w/o DCOnline events on the x-axis corresponds to the version, for which the DC online filter selected events are not forwarded to the FPF. By including these, one can see the efficiency of the FPT is significantly improved from 40 to 85%. The DC offline filter selects 57% of the events. When applying both filters we can see that the final combined signal efficiency is 95%. The combined rate is $\approx$ 10 Hz, which corresponds to a reduction of a factor of $\approx$13 compared to the input of 115 Hz to the FPF. The results for the low energy neutrinos correspond to the results of the only FPT branch with final improvements summarized in Table 7.1. The maximum improvement is still present for $\nu_{e,B}$ with a factor of 1.15. The upcoming ELOWEN2.0 selection will directly use the FPT events at trigger level. Thus, the improvements stated in Table 5.1 are still valid for that selection.

Flavor & energy	Relative trigger efficiency increase
$\nu_{e,A}$	1.08 $\pm$ 0.02
$\nu_{e,B}$	1.15 $\pm$ 0.02
$\nu_{e,C}$	1.09 $\pm$ 0.01
$\nu_{\mu,A}$	1.08 $\pm$ 0.02
$\nu_{\mu,B}$	1.09 $\pm$ 0.01
$\nu_{\tau,A}$	1.11 $\pm$ 0.02
$\nu_{\tau,B}$	1.13 $\pm$ 0.01

Table 7.1: Relative improvements for GeV neutrino simulation

Relative improvements above 1.03 for neutrino simulation in DC resulting from including the FPF. The energy intervals are: A(1–4 GeV), B(4–12 GeV) and C(12–100 GeV).

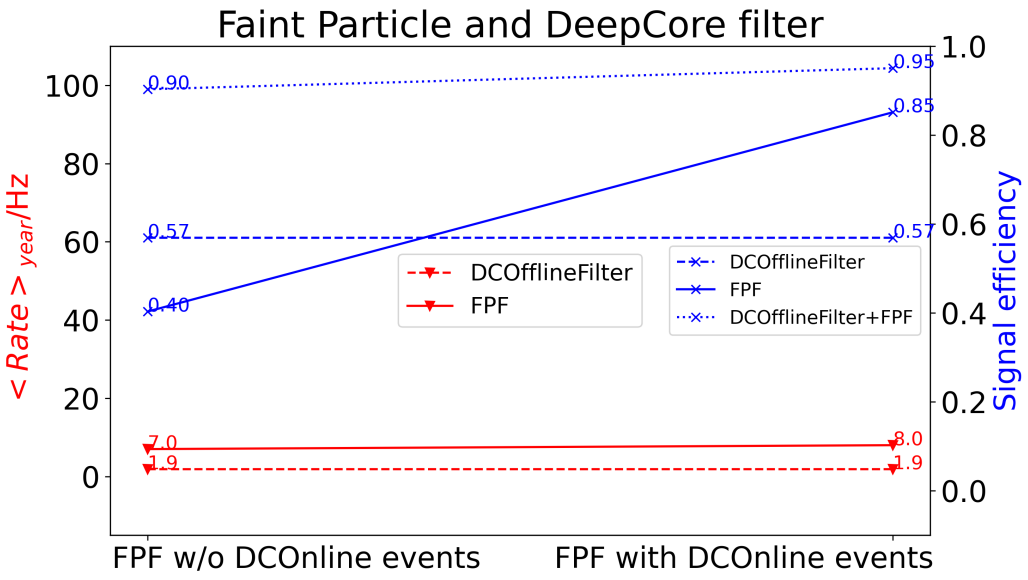

Figure 7.11: Faint Particle Filter results
Shown are the signal efficiencies (blue) for the FPF when not including and including the DC online filtered events as an input. Also, the signal efficiencies from solely applying the DC offline filter and the DC offline filter plus the FPF are shown. The average rates per year of the two offline filters are shown in red.

7.3 Faint Particle Filter test runs

Following the deployment of the FPT at the South Pole, an initial trivial FPF was introduced, which forwarded all FPT triggered events. Since the start of the 2024 data season, the new FPF described in this chapter has been implemented. Thus, comparing the trigger variable distributions between 2023 and 2024 processing essentially compares the performance of the FPT and the FPF.

The distributions include the same 2023 test run data shown in section 6.2. The FPF rate for the 2024 test run is 8.03 ± 0.01 Hz, which represents a rate reduction by a factor of approximately 12 compared to 2023. This reduction is visible in Figure 7.12, which shows the unnormalized number of hits.

Comparing the normalized hit distributions in Figure 7.12 shows that events with a high number of hits in DC are effectively removed, as intended.

The increase in the first bin of the distribution is driven by events forwarded by the DC online filter. These events are visible in the normalized distributions of the number of

hits, SLC fraction, and trigger length, as shown in Figure 7.12 (more variables are shown in Figure C.6). These are short-duration events with a low number of hits, primarily consisting of HLC hits. As a result, they contribute to the increase in the first bins of the number of hits and trigger length distributions.

The tail of the SLC fraction distribution, which corresponds to events containing more HLC hits, is enhanced by these events. Although these events represent roughly 12% of the FPF rate and are noticeable, they do not dominate the overall rate or distributions.

The SLC fraction cut for the trigger is set to values greater than 0.75, so events triggered exclusively by the FPT, dominate the SLC fraction above this threshold at the FPF level. However, with the inclusion of events from the online DC filter, lower SLC fraction events have also become relevant. In the trigger length distribution, the FPF reduces the maximum trigger length, as longer events tend to contain more hits, consistent with the number of hits distribution.

The implementation of the FPF aligns with expectations, successfully filtering events that are directly suitable for analyses involving low-energy neutrinos or faint BSM searches.

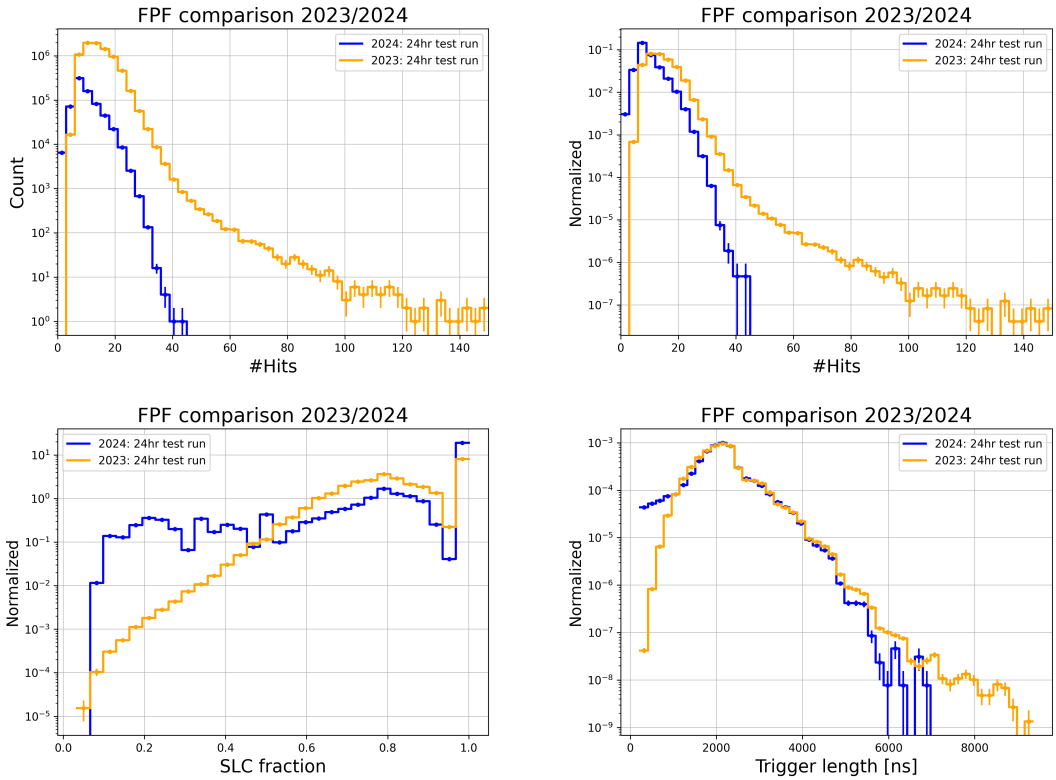

Figure 7.12: FPF variable distributions for test data

The number of hits (top left), normalized number of hits (top right) the SLC fraction (bottom left), and trigger length (bottom right) for the 2024 test run data (blue) and the 2023 test run (orange). This effectively compares the FPT trigger variables before (blue) and after applying the FPF (orange).

8

Improvements by the Faint Particle Trigger and Filter

In this chapter, the improvements brought by the FPT and FPF are analyzed at various processing stages. A comparison to the previous FCP analysis is made and model dependent expected event rates for MCP in IceCube are presented.

8.1 Simulation sets and comparison levels

To evaluate the improvements brought by the FPT and FPF, new simulation sets, for different mass and charge combinations, were generated using the latest IceTray version (1.11.1) and the recommended IceModel (spice ftp-v3). The improvements are compared at different processing levels..

8.1.1 Simulation sets

A summary of the simulation samples can be found in Table 8.1. For the direct comparison with the previous analysis, signals were simulated at 5 GeV, 10 GeV and 1000 GeV with energy spectra following a power law with spectral index of 2 for $\varepsilon = 2/3, 1/2, 1/3$. For lower values of ε, the spectral index was adjusted to 2.7 to align with the assumptions of the MCP flux model (see section 2.4), following the spectrum of the produced heavy mesons. Furthermore, masses above 10 GeV are not simulated for these, because the model does not predict such heavy particles.

Attempts were also made to simulate events with charge fractions as low as ε = 1/100, but after simulating 80 million events, no triggers were recorded. This suggests that detecting such low charged particles with IceCube might be extremely challenging due to the limited number of photons they emit.

Unlike the simulation samples used in the development of the FPT and FPF, no quality cut based on the minimum number of produced signal hits was applied to the events. Additionally, the energy spectrum was adjusted so that all particles have a velocity $\beta > 0.95$, because all the processing steps are adjusted for relativistic signatures and at β close to the Cherenkov threshold nearly no photons are emitted (see Equation 2.1).

ε	mass [GeV]	#Events [$\cdot 10^6$]	spectral index
2/3	5, 10, 1000	1.4, 0.8, 0.7	2, 2 , 2
1/2	5, 10, 1000	9, 9, 0.4	2, 2, 2
1/3	5,10, 1000	13, 9, 3	2, 2, 2
1/5	5, 10	9, 10	2.7, 2.7
1/10	5, 10	9, 11	2.7, 2.7
1/20	5, 10	81, 12	2.7, 2.7
1/33	5	70	2.7

Table 8.1: Simulation parameter
The simulated charges, masses, number of events and spectral indices for the corresponding samples are summarized.

8.1.2 Trigger level

A comparison at trigger level at South Pole is useful. All triggered data is stored on hard disk and can be accessed after shipping if needed. However, processing this data requires significant resources and effort.

8.1.3 Online Filter level

For the new filtering scheme (explained in section 3.6) the effective area at the online filter level is shown. This represents all the events that are available after satellite transfer. These are planned to be stored on a few years scale. Events removed prior to transfer include those triggered solely by the string or volume triggers, as well as SMT8–SMT12 triggers. However, a subset of SMT8–SMT12 events is retained by the new online muon filter.

8.1.4 Filter level

The final comparison involves an analysis at the (offline) filter level, corresponding to data in the long-term storage. In the previous analysis, four filters were utilized: DC13, LowUp, VEF, and OnlineMuonL2, yielding a combined rate of $\approx 60\,Hz$ [32]. For a comparison to the new filtering scheme the new FPF, offline DC, ELOWEN and offline muon filters were selected. The offline DC and offline muon filters are modern implementations of the previous OnlineMuonL2 and DC13 filters, incorporating additional cuts that have been applied at the analysis level in recent years. The ELOWEN filter is a new filter that was previously a selection developed for low energy neutrinos based on DC triggered events [81].

Combined, these four new filters result in a rate of $\approx$ 11 Hz. The difference in rate makes an apples to apples comparison impossible, because the new filters were developed to apply stricter cuts. One can assume, that a significant amount of events is lost by the old analysis when reaching the 11 Hz level[1]. Thus, the improvements here compare 60 Hz (old) vs 11 Hz (new) which results in reading the improvements shown in the next sections as lower bounds of the relative improvements.

The comparison at filter level compares the four old filters (applied to standard triggered events) used in the previous analysis and the four new filters (applied to standard triggers + FPT events), that are suitable for dim signatures, that will be used in future. A comparison of the importance of the FPF within the new filters can be found in Appendix D.

[1]For the old analysis only for an ε of 1/3 the information is available that at Level3 of the analysis, which corresponds to 2 Hz, 33% of the signal events remained, resulting in 33% of the effective area in our comparison. As this is already a factor ≈ 5 below the new filter selection rate this is also not directly comparable. As the cuts were optimized it does also not scale linearly.

8.2 Trigger efficiency comparison for various masses

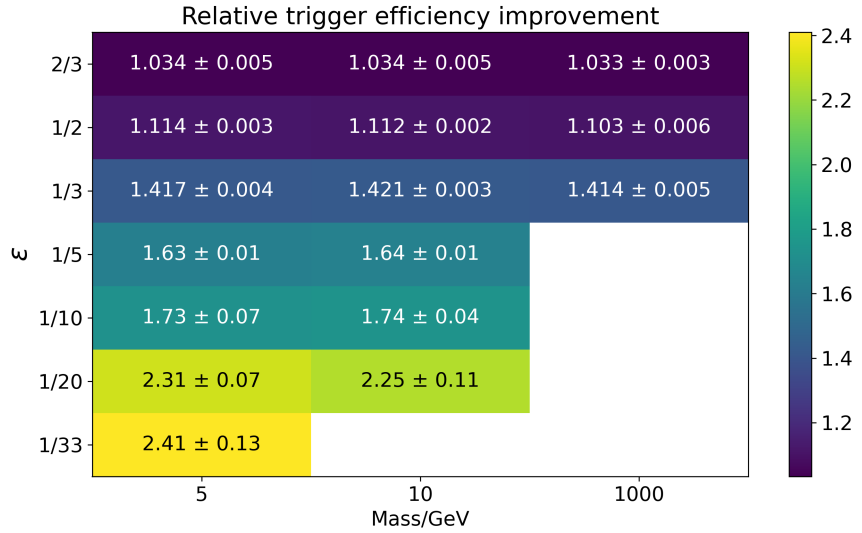

Figure 8.1: Trigger efficiency comparison for various masses and charges
The relative trigger efficiency improvement and the statistical error are shown for the different simulation samples. These are the relative improvements for the isotropic scenario.

To analyze the mass dependency on the trigger efficiency improvement, the relative improvements for the different samples were evaluated as shown in Figure 8.1. The first thing to compare is the relative improvement of 1.41 for $\varepsilon = 1/3$ at a mass of 1 TeV, which is lower than the previously reported value of 1.55 (stated in subsection 5.1.7). This discrepancy arises from two main factors.

First, no minimum cut on the number of signal hits is applied in this analysis, reducing the relative improvement by approximately 0.09. Consequently, lower-quality events, which are unlikely to progress to later processing stages, decrease the overall improvement, while high-quality events are preserved.

Secondly, the change in the energy spectrum has an effect of decreasing the relative improvement by approximately 0.05. The reason for this could be that events with velocity close to $\beta = 0.75$ can last up to 1/4 longer in the DC volume due to their lower velocity increasing the probability of creating hits. On the other hand they significantly emit less photons compared to events at $\beta = 0.95$. A positive effect of more emitted hits during their passage through DC for events with velocities below $\beta = 0.95$ is possible. Additionally, the spectrum itself, which begins at higher energies, may influence the ratio of high-quality

to low-quality events.

When examining the statistical errors, it becomes evident that these do not correlate with the size of the simulation samples. This discrepancy arises, because events are generated on a disk located 1 km from the detector center, as described in chapter 4. As a result, the simulated particles traverse a significant distance through the ice before reaching the detector, which suppresses events with lower masses that typically carry less energy. Consequently, this leads to an increased triggering of higher-mass signal events, thereby altering the trend of the errors. This disk-to-detector propagation effect is effectively removed by including survival probabilities as discussed in section 2.6.

When analyzing the general trend, when decreasing the charge at a fixed mass of 5 GeV, the expected behavior of an increasing improvement due to the FPT is observed. For the highest ε of 2/3 no significant improvement is expected, since this charge did not have a problematic trigger efficiency in the last analysis, because these events produce dominantly HLC hits. For ε of 1/2 the best limits were calculated in the last analysis [32]. Here an improvement of 1.11 is achieved. As the charge decreases, the probability of producing HLC hits diminishes, leading to increased inefficiency of the standard triggers. For ε of 1/3, 1/5, 1/10 improvements of 1.42 1.63 and 1.73 are achieved, respectively. These are the most important improvements since the FPT was developed around simulation of ε of 1/3. For the maximum improvements at the lowest charges, it will be shown that the effective areas for these charges are only a few tenths of square meter and thus they are not very important.

When examining different masses at a fixed charge, it is observed that the relative improvements remain consistent across various masses. This effect is expected, because the dominant light production process is the production by the Cherenkov effect, which is independent of the mass (see Equation 2.1). Only a small fraction of events contain photons produced by ionization or secondary processes, as discussed in subsection 2.5.6. Thus, the relative improvements shown in the next sections hold true for the entire mass range in the isotropic scenario.

8.3 Effective area comparison

The effective area is calculated as explained in 4.1.5 and for all ε the simulation sample for a mass of 5 GeV is chosen. A direct comparison to the old analysis is done and the impact of the survival probability (as explained in section 2.6) on the effective area is analyzed.

8.3.1 Effective area in the isotropic scenario

In Figure 8.2, the effective areas for the isotropic scenario at various values of ε are shown, calculated using Equation 4.1. One can analyze the ratio for consecutive effective area

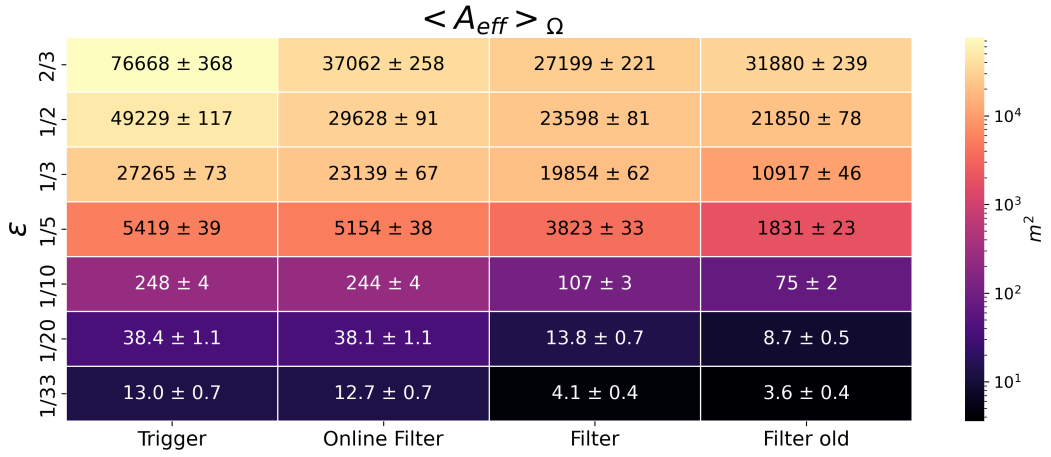

Figure 8.2: Averaged effective area for the isotropic scenario
The effective area for the isotropic scenario is shown for different processing stages and different ε. For $\varepsilon = 2/3, 1/2, 1/3$ the spectral index is 2 and for the others 2.7. The mass for all ε is 5 GeV.

values between ε of 1/33 to 1/5 at trigger level and compare it to a straightforward expected increase, which can be calculated by:

$$I_e = \frac{\varepsilon_2^2}{\varepsilon_1^2}, \quad \varepsilon_2 > \varepsilon_1 \tag{8.1}$$

The expected increase I_e results in factors of 3,4 and 4 for consecutive ε up to 1/5. The ratios with values from Figure 8.2 result in factors 3, 6, and 22. A large discrepancy arises between the expectation for the effective area increase for ε changing from 1/5 to 1/10 and the obtained values from simulation. This suggests that DC, due to the string and DOM spacing, is starting to become sensitive to signatures between ε of 1/5 to 1/10. Below ε of

1/5 the effective area decreases rapidly. Analyzing ε between 1/3 and 2/3 results in I_e of 1.5 and 1.7 and obtained values of 1.8 and 2.3. Here the improvements from the simple expectation do not show large deviations from the obtained values with simulation and behave as expected.

Inspecting the development of the effective area at the online filter level one finds that for ε above 1/3 a significant amount is lost compared to the trigger level. The reason is that there exists no dedicated online filter for events, that are too dim for the ones optimized for muons and too bright for the FPT and DC trigger, of which all events are transmitted. Nevertheless, the effective area at online filter level exceeds the old filtering level for all ε. For ε below 1/3 one can observe, that at online filter level, the fraction of kept events increases, due to the rising importance of the FPT and DC trigger.

In Figure 8.3 the improvements at trigger and filter level are compared. For the trigger level the importance of the FPT is increasing with a decreasing charge as expected. Factors between 1.42 to 2.41 are achieved for ε below 1/2.

The filter comparison shows for an ε of 2/3 a reduction by a factor of 0.85. The new implementations of the DC and muon filters apply stricter cuts. As these were not optimized for these signatures a significant amount of events is lost. Furthermore, the new FPF was not developed for ε above 1/3. This explains the reduction. This motivates developing a dedicated offline filter for events with ε above 1/3, because as discussed before at online filter level, the effective area is larger compared to the old filter (see Figure 8.2).

For the rest of the ε values improvements by the new filters are observed. Largest improvements can be found for ε of 1/3 and 1/5 with improvements of 1.82 and 2.09 respectively. The boost of improvement is explainable, since the only old filter being sensitive to these charges was the DC filter, being less efficient with a decreasing charge.

Below ε of 1/5, the new filters exhibit decreased efficiency. Events lost by the new filters are predominantly identified as noise by the noise engine module, and the quality of these events at this point is questionable. However, the new filters preserve events that produce a significant number of signal hits from these samples. At such low charges, these high-quality events are less probable, which explains the decrease in overall efficiency.

The previous analysis on FCP analyzing ε between 2/3 to 1/3 uses $\approx$ 5 years of data [32].

To repeat an analysis in IceCube, a minimum improvement by a factor of $\frac{1}{\sqrt{2}}$ is required. This can be achieved by doubling the statistics. For an ε of 1/3 at filter level the required additional 5 years of old data taking would correspond to 2.25 years of the new data taking, saving 2.75 years. Thus, either new analysis results can be produced faster or significantly better results after doubling the statistics. These improvements allow to faster conduct dedicated analyses to further constraint or discover new physics of the uncovered parameter space of particles with an anomalous charge.

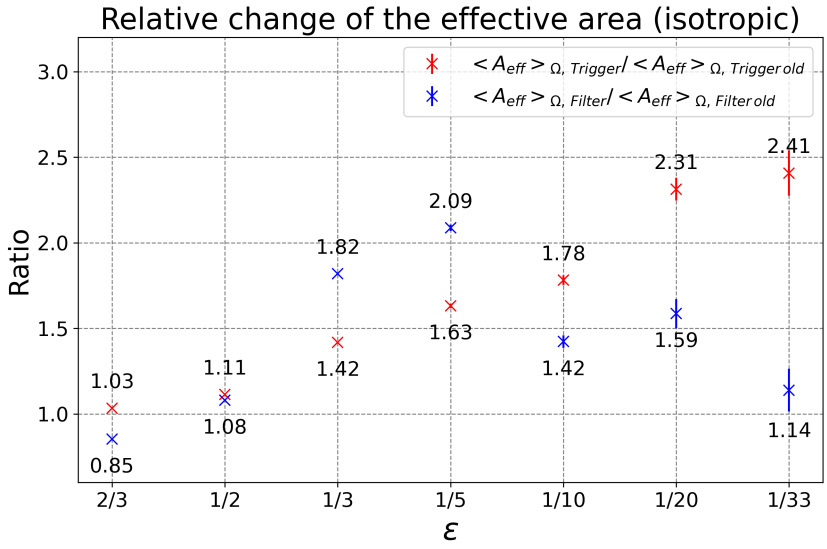

Figure 8.3: Relative changes for the isotropic scenario
Relative changes for the Trigger (red) and Filter level (red) are shown.

8.3.2 Effect of the survival probability on the zenith distribution

Using the survival probability (see Equation 2.3) as a weight for each event has an influence on the zenith distribution of the events. The events are injected isotopically around the detector. At trigger level the zenith distribution shows an enhancement towards up-going events as shown in the dashed lines in Figure 8.4. This is explained by the location of DC (see Figure 3.2) and the disk-to-detector propagation effect (section 8.2).

For a ε of 2/3, the up-down going asymmetry is least pronounced. The events are less dependent on the DC trigger and FPT than those with lower ε. Furthermore, these events have the highest energy loss in the comparison, removing more low energy events in the spectrum than for the other charges. With decreasing charge, the asymmetry increases, because lesser events are suppressed by traversing the distance to the detection volume

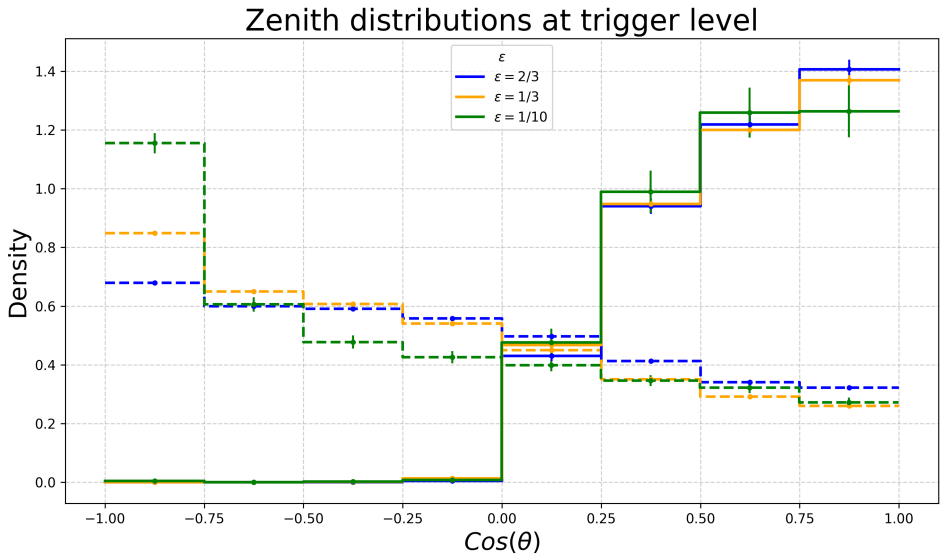

Figure 8.4: Effect of the survival probability on the cosine zenith distribution
The cosine of the zenith angle for different ε. The lines represent the zenith distributions at trigger level for the isotropic scenario (dashed) and the weighed events (solid). Events are weighed according to the survival probability. For $\varepsilon = 2/3, 1/3$ the spectral index is 2. For $\varepsilon = 1/10$ the spectral index is 2.7.

and the standard triggers get less efficient. Below an ε of 1/2, the DC and FPT are the dominant triggers. The isotropic injection around the detector is, with decreasing charge, converted to a more non-isotropic scenario with more pronounced asymmetry towards up-going events at trigger level.

The solid lines in Figure 8.4 show the zenith distributions for which each event is weighted according to the survival probability. For all ε, the contributions below $\cos(\theta) = 0$ are heavily or totally suppressed, due to the rapidly increasing distance that the particles must traverse. In the reweighted distributions, the most significant bin corresponds to the least traversed distance. In this bin, the samples are sorted by charge, as higher charges experience greater suppression with increasing distance. This suppression significantly impacts the effective area and the importance of the FPT.

8.3.3 Effective area for the non-isotropic scenario

In Figure 8.5, the effective areas for the non-isotropic scenario at various values of ε are shown, calculated using Equation 4.2. For all ε these are significantly reduced, compared to the isotropic scenario, up to a factor of 25 for an ε of 1/5. The improvements at trigger and filter level for the non-isotropic scenario can be found in Figure 8.6. The comparison

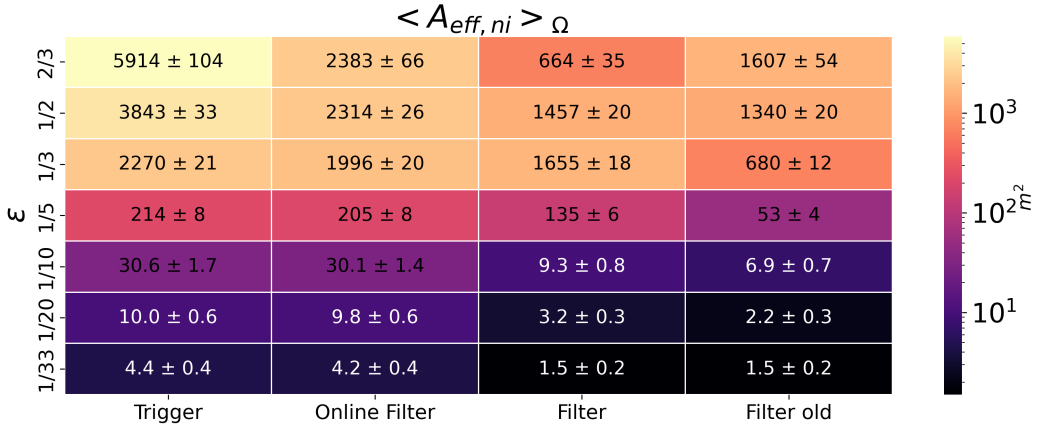

Figure 8.5: Relative improvements for the non-isotropic scenario
The effective area for the non-isotropic scenario is shown for different processing stages and different ε. For $\varepsilon = 2/3, 1/2, 1/3$ the spectral index is 2 and for the others 2.7. The mass for all ε is 5 GeV.

at trigger level shows, compared to the isotropic scenario, that all relative improvements are now further improved. The survival probability increases the weight of shorter path length to the detector. Most affected are the higher charges, improved by a higher fraction of more vertical events with higher probability to produce more hits than in the horizontal case.

The importance of the FPT increases with decreasing charge. Improvement of factors of 1.72, 2.02 and 2.19 for ε of 1/3, 1/5 and 1/10 at 5 GeV are achieved, respectively. At filter level one can see a significant reduction for ε of 2/3 to 0.41. At online filter level the effective area also exceeds the old filtering in the non-isotropic scenario. Thus, a new dedicated offline filter could compensate that decrease. Largest improvements are seen for ε of 1/3 and 1/5 as in the non-isotropic case. Since the importance at trigger level was increased, it is expected that it is increased at filter level as well. Factors of 2.43 and 2.56 are achieved respectively.

One can conclude that, by including the survival probability, the improvement at trigger level is for all ε, accept for 1/20, increased. Including the survival probability changes the relative improvements. The constant improvement behavior for the masses depicted in Figure 8.1 at the trigger level is applicable only in the isotropic scenario. This is not the case for the non-isotropic scenario. As illustrated in Figure 2.8, an increasing mass approaches a more isotropic distribution. Consequently, the relative improvements for an increased mass

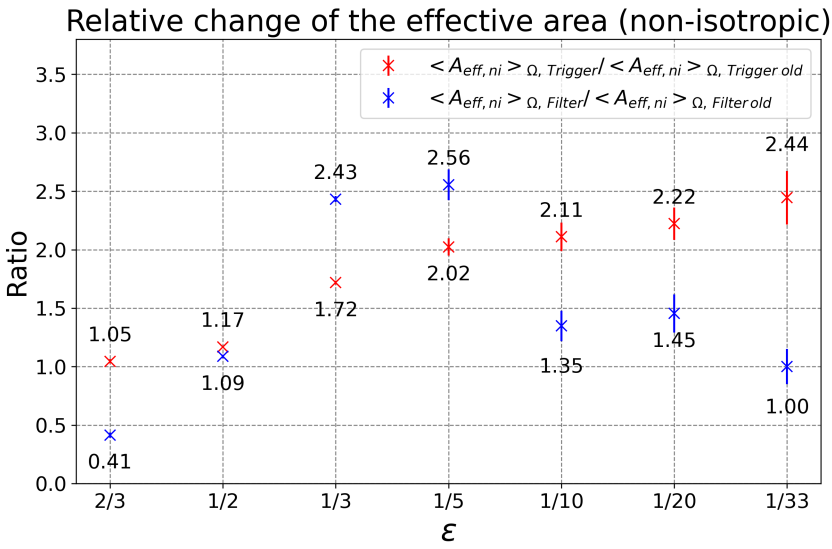

Figure 8.6: Relative changes for the non-isotropic scenario
Relative changes for the Trigger (red) and Filter level (red) are shown.

should converge towards those from the isotropic scenario. The relative improvements for ε of 2/3, 1/2 and 1/3 for the non-isotropic case were calculated at a mass of 1 TeV. These result in 1.04, 1.15 and 1.65. Comparing them with the improvements in Figure 8.1 shows the expected decreasing behavior towards the isotropic scenario improvements.

8.4 Expected event rates for the MCP model

By utilizing the flux predictions from Figure 2.4, the expected event rates can be calculated. Here the flux prediction from the decay of the Υ meson, which has a rest mass of 9.46 GeV is chosen. The corresponding highest FCP mass would be 4.7 GeV and here the simulations for a mass of 5 GeV are used. The integrated flux prediction at this point was chosen as $\Phi(\varepsilon)_i = \varepsilon^2 \cdot 10^{-13}\ cm^{-2} sr^{-1} s^{-1}$ (see Figure 2.4). The variation of this value close to the endpoint can be done by scaling it with factors that linearly affect the expected event rate. This value itself underlays a large uncertainty as discussed in section 2.4. The approximated event rates are only estimates and only the statistical error on the effective area is shown. These expectations serve as an initial investigation down to which charge and from which zenith angle MCP could be expected in IceCube. The expected event rate

per year per zenith interval is calculated by:

$$R_{\varepsilon,expected}(\theta_{int},\varepsilon) = 3.145 \cdot 10^7 s \cdot \Phi(\varepsilon)_i \cdot < A_{eff,ni}(\theta_{int}) >_{\phi} \cdot 2\pi \cdot (cos(\theta_{min}) - cos(\theta_{max}))$$

The sum over all angle intervals corresponds to the expectation, and the results are shown for different zenith intervals for $\varepsilon = 1/5$ in Figure 8.7. The plot illustrates the effective area and expected event rates at the trigger, filter, and old filter levels within zenith bins of 20°. The effective area was calculated using Equation 4.3.

Including the survival probability is reflected in the suppression of the bins above 80°. The effective area exhibits a maximum at 40°, while the expected event distribution peaks in the 40° and 60° bins. Here, the higher flux contribution in the 60° bin increases the expectation to approximately 0.15 events per year, which is equivalent to the expectation for the 40° bin. Closer to the horizon, the expected events drop to 0.025, indicating that a potential analysis could not benefit from cutting close to the horizon. However, at this low charge, the separation from muons should be enhanced compared to the previously analyzed lowest ε of 1/3.

The summed expectation for ε of 1/5 is 0.40 $\pm$0.02 events per year at trigger level, 0.25 $\pm$0.01 at filter level and 0.10 $\pm$0.01 at old filter level. Around ten years of the old filter level data are available. Combined with multiple years of the new filter level, an analysis could be conducted for an ε of 1/5. The result for ε of 1/10 is shown in Figure D.7 (for ε of 1/3 in Figure D.6). The values for ε of 1/10 do not result in a sufficient amount of expected signal events even with 100 years of data.

The values carry significant uncertainties due to the model itself and the mentioned systematic effects (see section 2.4), which would be analyzed in a dedicated analysis.

It can be concluded that for future analyses of the MCP with a mass of 5 GeV, an ε value of 1/5 could be analyzed. Additionally, values between $\varepsilon = 1/5$ and $\varepsilon = 1/10$ could also be explored.

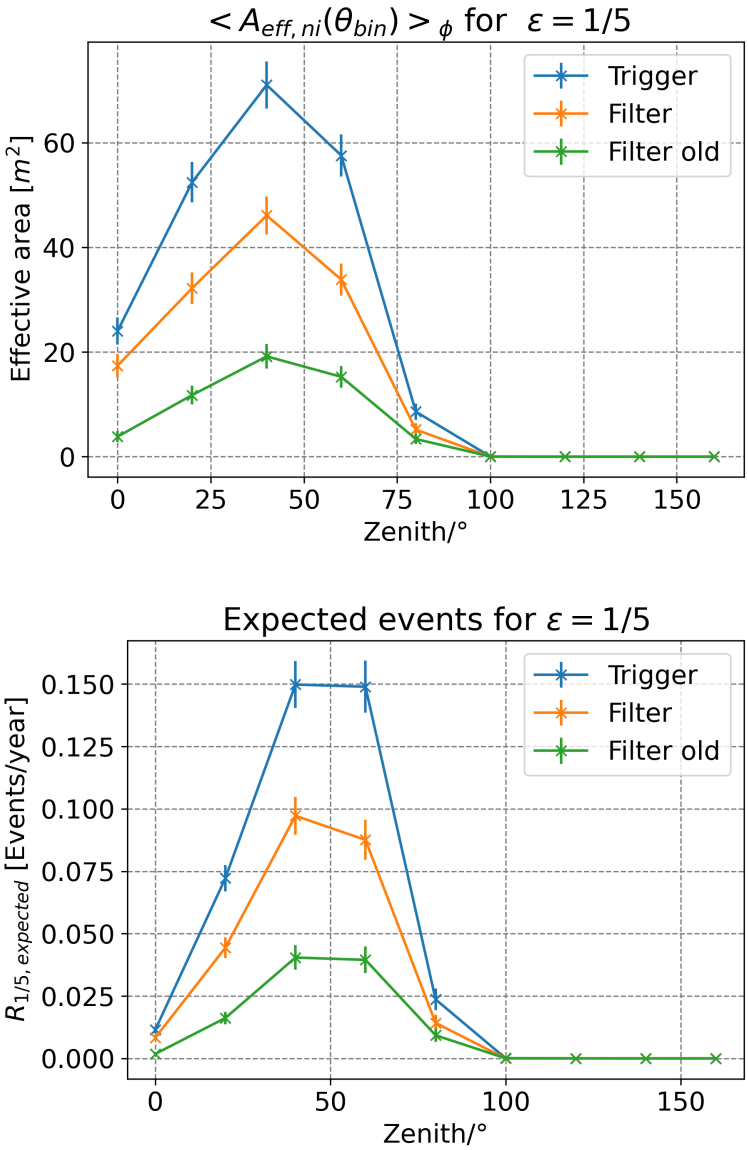

Figure 8.7: Effective area and expected event rate for ε of 1/5
The zenith dependent effective area (top) and calculated expected event rates (bottom) are shown. The trigger level (blue) and old (green) and new filtering level (orange) are compared.

9

Conclusion and Outlook

In this thesis the development of the FPT and FPF for the IceCube Neutrino Observatory and the corresponding improvements are discussed. The successful deployment of the FPT results in a significantly higher trigger efficiency for faint signatures in IceCube, while increasing the event rate by a factor of 1.004.
Included are free FCP predicted in several BSM models, with unknown mass and charge. Relative improvements at trigger and filter level were compared for an isotropic and non-isotropic scenario. For the latter relative improvements at trigger and filter level above two were found for a charge of $\frac{1}{5}e$, which corresponds to the lowest charge in a specific MCP model, resulting in analyzable event rate estimation. Additionally, leptons in the GeV energy range are triggered with relative improvements up to 1.18.

In future dedicated filters[1], using GeV energy leptons, will directly forward the FPT events to the filter. Seasonal variation analyses using GeV leptons could also benefit from including the newly triggered data. Furthermore, the uniformly processed FPF events can directly be used for future BSM searches for faint signatures, like particles with an anomalous charge.
As discussed in chapter 8, the development of a new dedicated offline filter for charges above $\frac{1}{3}e$ is required, because a lot of signal events are lost between the online and offline filter level for these charges.
The forthcoming IceCube Upgrade will significantly increase the sensitivity to GeV energy leptons in a denser instrumented sub volume of DC [82]. No conclusive result for the

[1] f.e. the future ELOWEN2.0 filter

impact on the trigger efficiency of the FCPs can be obtained so far, because the input to the trigger system and the trigger algorithms are not finalized. The former will be constrained by DAQ limitations and the latter tailored to particles carrying the elementary charge. Therefore, in future the IceCube Upgrade will improve the trigger efficiency for FCP searches and the impact needs be analyzed. This could be very beneficial for charges below $\frac{1}{5}e$ for which the current triggers rapidly loose signal efficiency.

Furthermore, a full detector version of the FPT could be implemented in future, if the satellite bandwidth is extended. The full detector version using the isolated DOMs method (as described in section 5.2) would be a suitable candidate, which would significantly increase the trigger efficiency using the entire detection volume. For this FPT version tests at the SPTS would have to be conducted.

All of the achieved and forthcoming improvements allow to scan the parameter space for particles with an anomalous charge significantly faster.

A

Appendix A

In Figure A.1 the time differences of hit pairs before and after the velocity cut are shown. Before the velocity the distribution shows a higher probability for lower time differences. This is driven by the formation of hit pairs, which is depicted in Figure 5.1. Larger time differences are suppressed, because large time differences are only formed in the first iteration, between the first and last hit. This explains the trend of the distribution. After the cut, the small time differences that result in higher velocities are removed. The distance

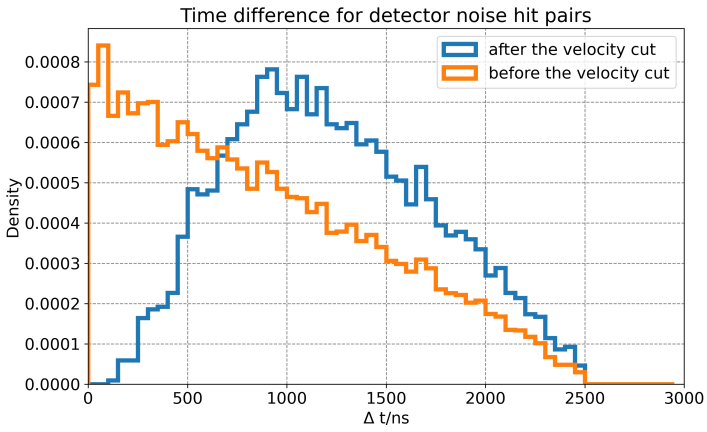

Figure A.1: Δt for Detector Noise hit pairs
Distributions for the time differences of hit pairs for simulated Detector noise before and after the velocity cut.

difference distribution shown in Figure A.2 shows peaks at the string and DOM spacings. The cut shifts the mean distance to higher values, resulting in combination with the higher time differences after the cut in lower velocities.

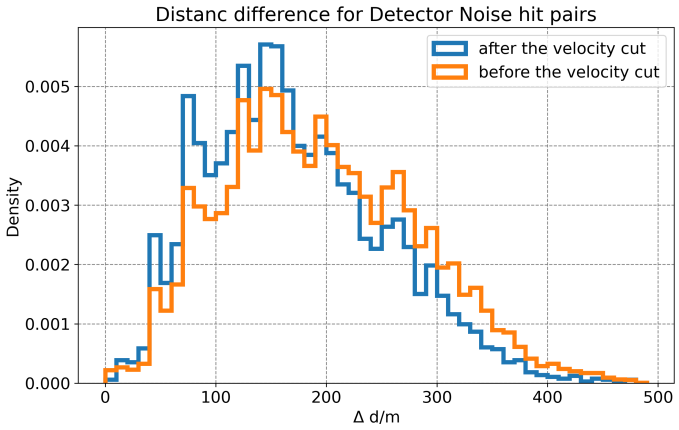

Figure A.2: Δd for Detector Noise hit pairs
Distributions for the distance differences of hit pairs for simulated Detector noise before and after the velocity cut.

The maximum zenith histogram bin count values are shown for the 50° bin size in Figure A.3. This showed no preferred cut option compared to the 20° bin size.

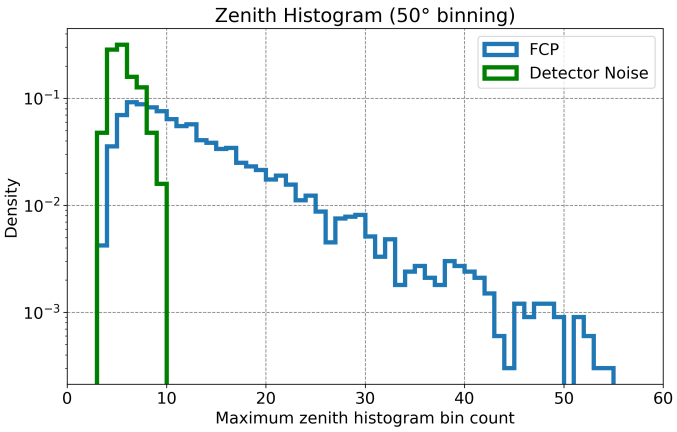

Figure A.3: Bin size of 50° for directional clustering of Doubles
The maximum bin counts of the zenith histograms for a bin size of 50° is shown. In blue for FCP and in green for Detector Noise.

The maximum bin count of the zenith vs. azimuth histogram for FRT data is shown in Figure A.4.

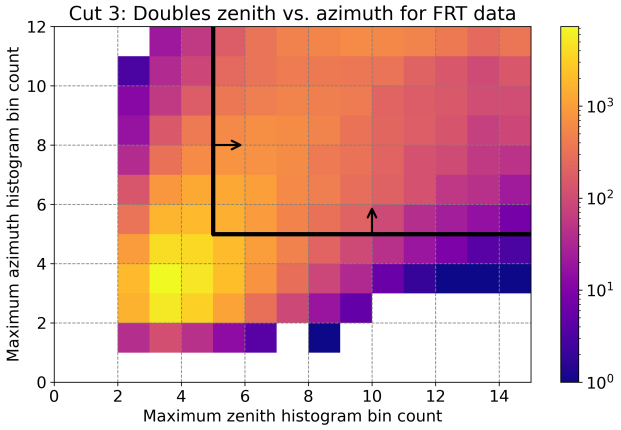

Figure A.4: Maximum zenith vs. azimuth bin count for FRT data
The maximum bin count of the zenith vs. the azimuth histogram is shown for FRT data. The black lines indicate the cut values and the arrows the region that is kept.

Cuts for the full detector (isolated) DOMs version.

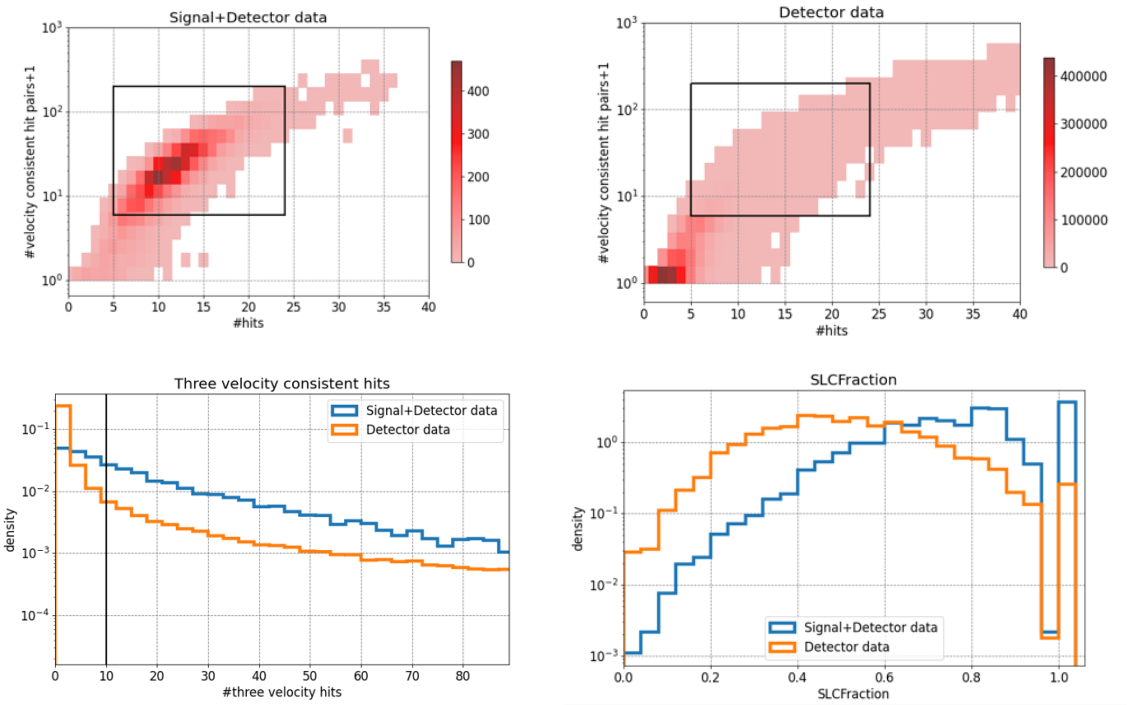

Figure A.5: FPT full detector version (isolated DOMs) cut variables
The number of hits vs. the number of Doubles (top) for FCP (left) and data (right), number of Triples (bottom, left) and SLC fraction (bottom, right). The plots are shown for FCP mixed with FRT data (blue) and FRT data (orange) for the full detector (isolated DOMs) version.

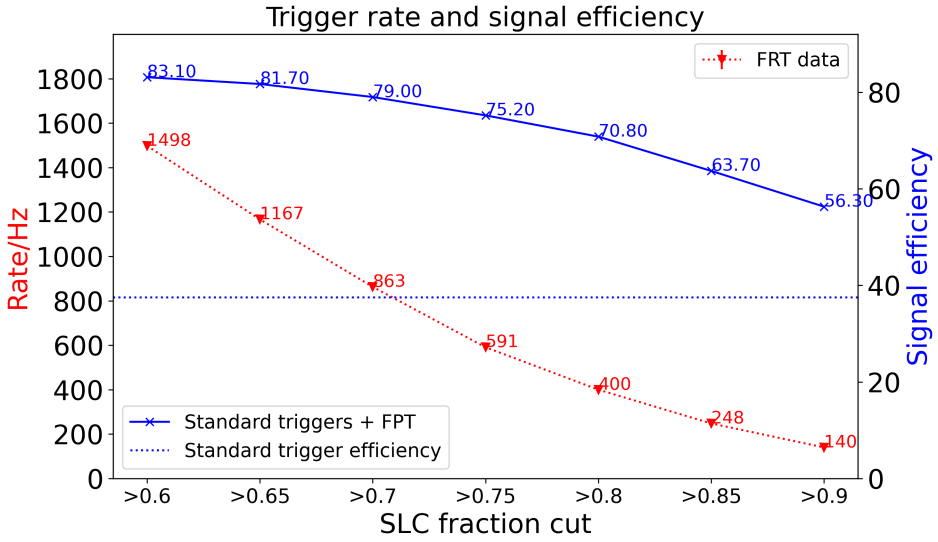

Figure A.6: SLC fraction cut optimization full detector (isolated DOMs)
Shown are the estimated FPT trigger rate (dotted red), the standard trigger efficiency on FCP (dotted blue) as a reference and the combined trigger efficiency of the standard triggers plus the FPT on FCP (solid blue).

For the full detector version (all hits) additionally the parameter of the minimum and maximum Triple velocity are included. This corresponds to the velocity bounds of the additional calculated hit pair that allows to form a Triple.

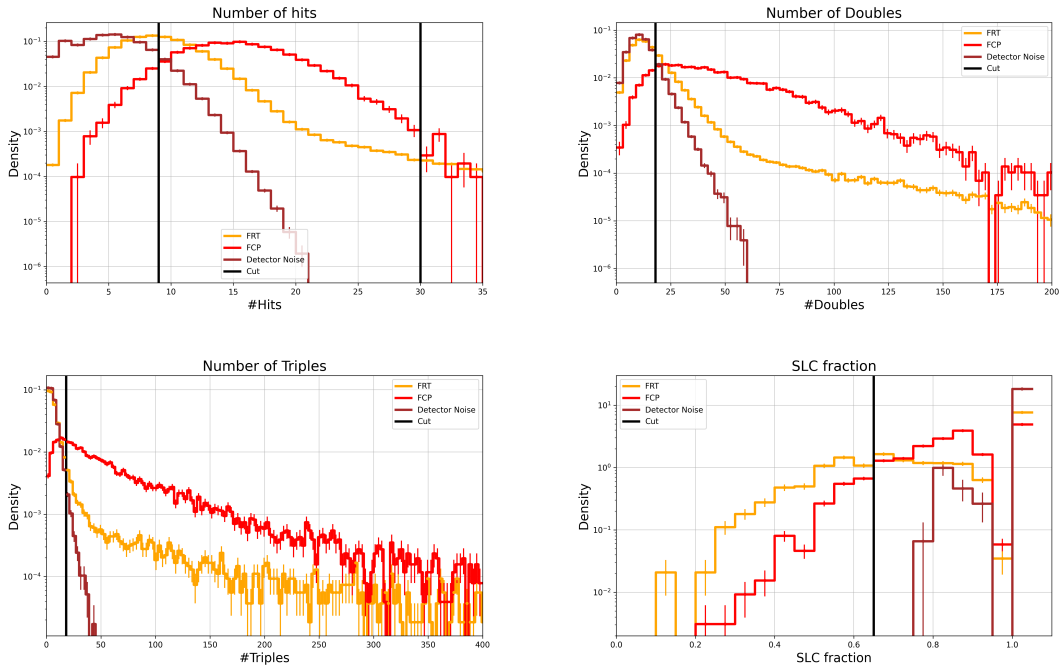

Figure A.7: FPT full detector version (all hits) cut variables
The number of hits (top,left), number of Doubles (top, right), number of Triples (bottom, left) and SLC fraction (bottom, right) for FCP(red), FRT data (orange) and Detector noise (brown) for the full detector (all hits) version.

Parameter	Value
time_window	3000 ns
time_window_separation	800 ns
max_trigger_length	1 ms
hit_min ($\geq$)	9
hit_max ($\leq$)	30
double_velocity_min (>)	20 000 km/s
double_velocity_max (<)	390 000 km/s
double_min ($\geq$)	18
triple_velocity_min (>)	2 000 km/s
triple_velocity_max (<)	430 000 km/s
triple_min ($\geq$)	18
slcfraction_min (>)	0.65
domSet	11

Table A.1: FPT full detector version (all hits) parameters

For the IC79 version the minimum and maximum Triple velocities are the same as the minimum and maximum Double velocities.

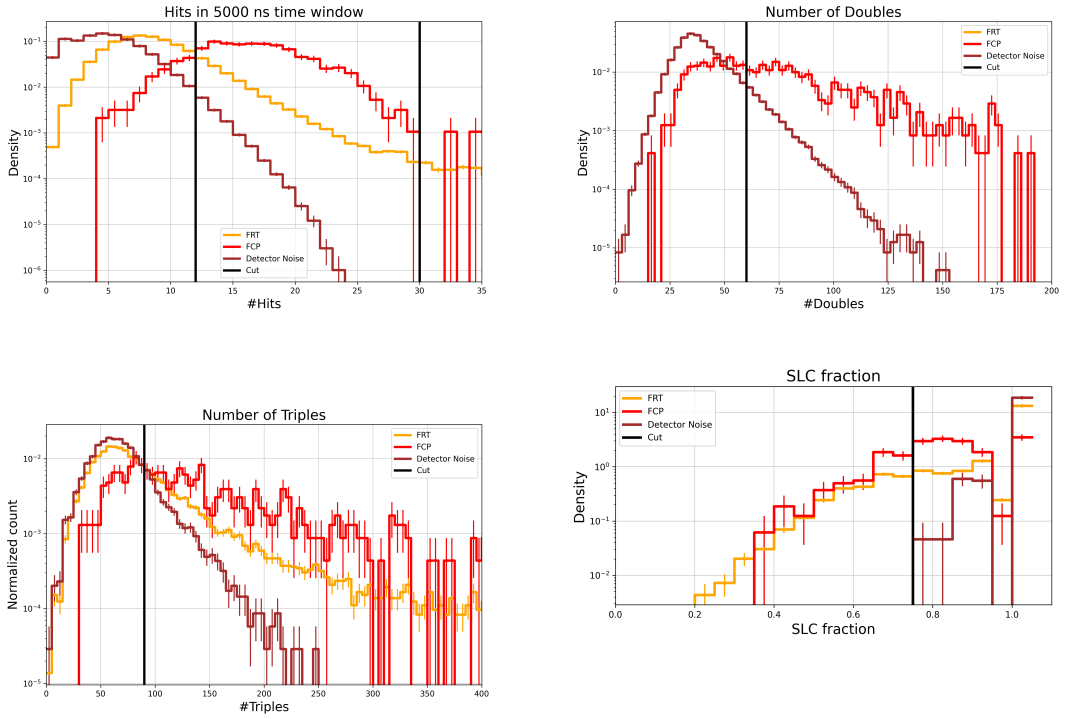

Figure A.8: FPT IC79 cut variables

The number of hits, number of Doubles, number of Triples and SLC fraction for FCP(red), FRT data (orange) and Detector noise (brown) for the full detector all hits version.

Parameter	Value
time_window	5000 ns
time_window_separation	800 ns
max_trigger_length	1 ms
hit_min ($\geq$)	12
hit_max ($\leq$)	30
double_velocity_min (>)	20 000 km/s
double_velocity_max (<)	420 000 km/s
double_min ($\geq$)	60
triple_min ($\geq$)	90
slcfraction_min (>)	0.75

Table A.2: FPT IC79 version parameters

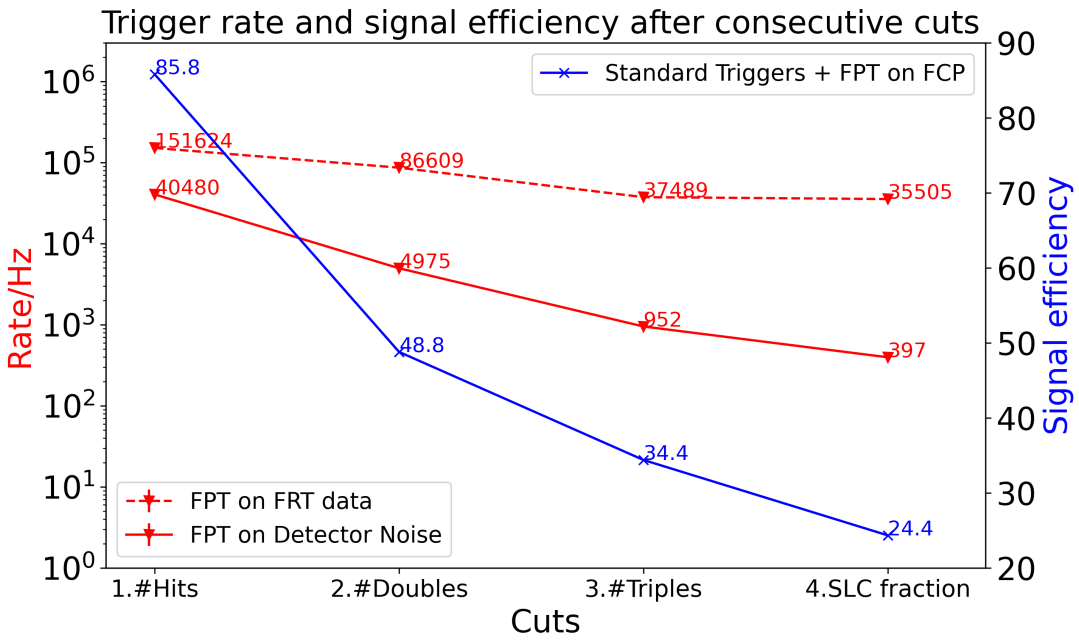

Figure A.9: Summary of cuts for the IC79 version

Cuts are applied consecutively. For each cut, the corresponding rates and signal efficiencies are shown. The blue lines show the signal efficiency from applying the standard triggers plus the FPT on FCP simulations for the IC79 version. The red lines show the estimated FPT rates, derived from applying the corresponding FPT version to detector noise simulation (solid) and FRT data (dashed).

B

Appendix B

Distributions for the #Doubles, the hit pair velocity and the azimuth and zenith maximum bin count values. The plots compare the SPTS (Java) and FRT data (C++) version of the FPT.

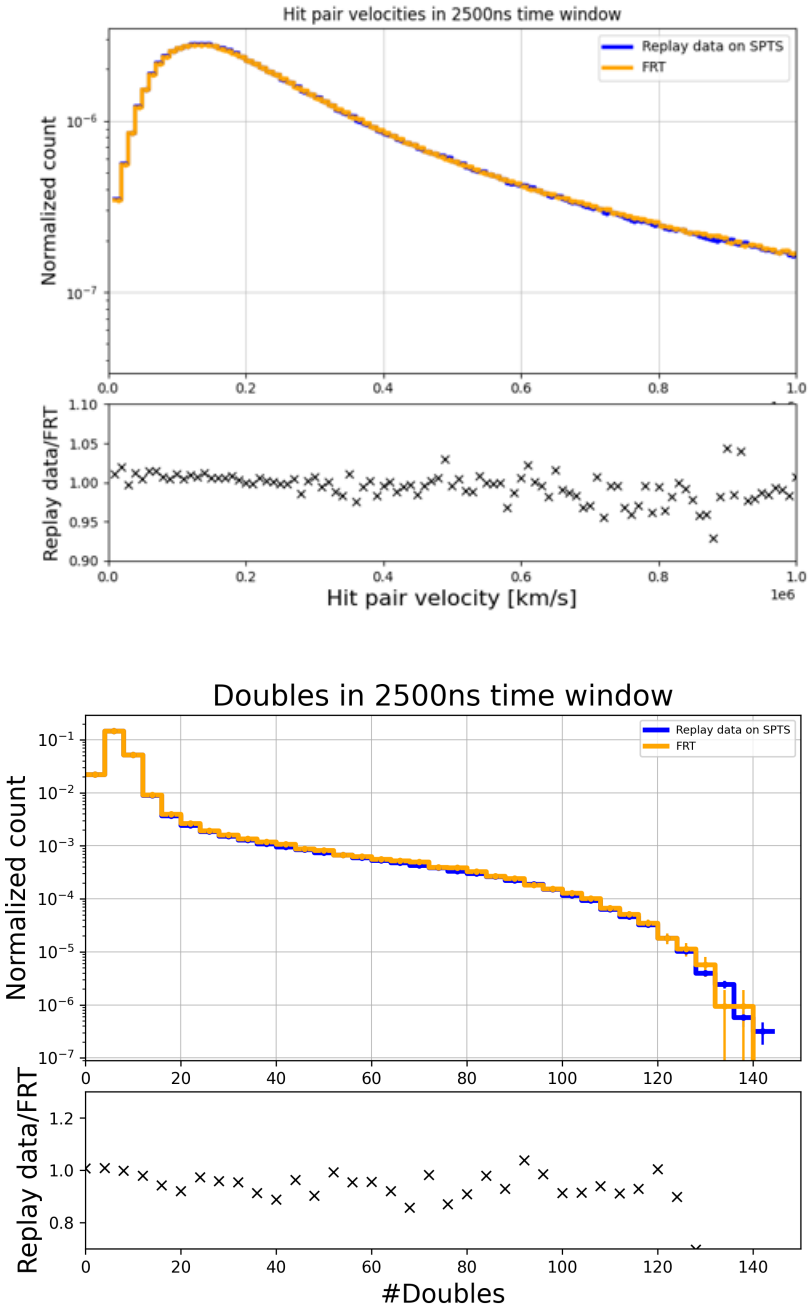

Figure B.1: Hit pair velocity and Doubles comparison (FRT and SPTS)
The figure shows the hit pair velocity (top) and #Doubles. A comparison between the JAVA version running on the SPTS (blue) and the C++ version applied to FRT data (orange).

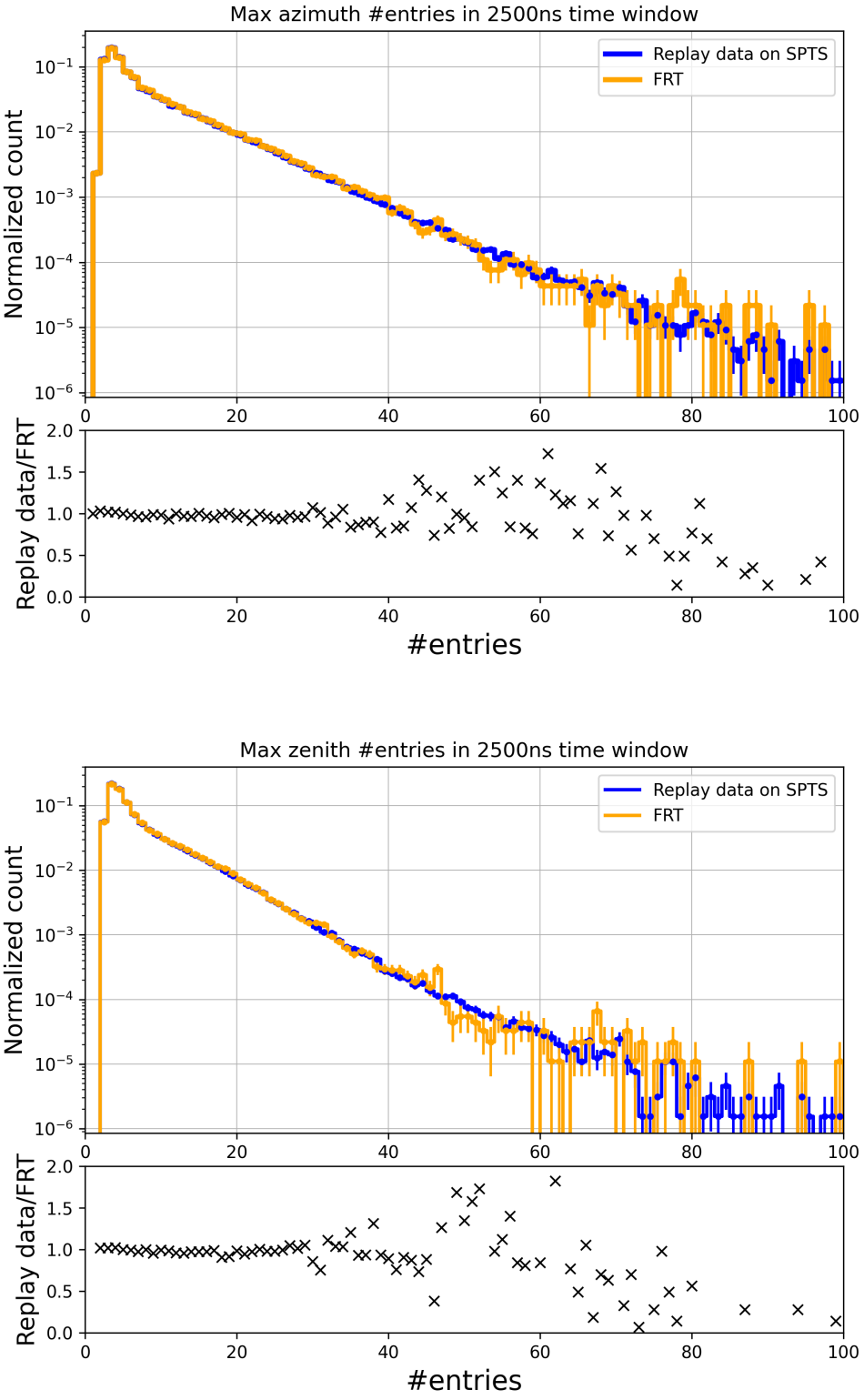

Figure B.2: Azimuth and Zenith comparison (FRT and SPTS)
The figure shows the maximum azimuth (top) and zenith (bottom) bin count distributions for the JAVA version running on the SPTS (blue) and the C++ version applied to FRT data (orange).

Further trigger variable comparison for the test runs.

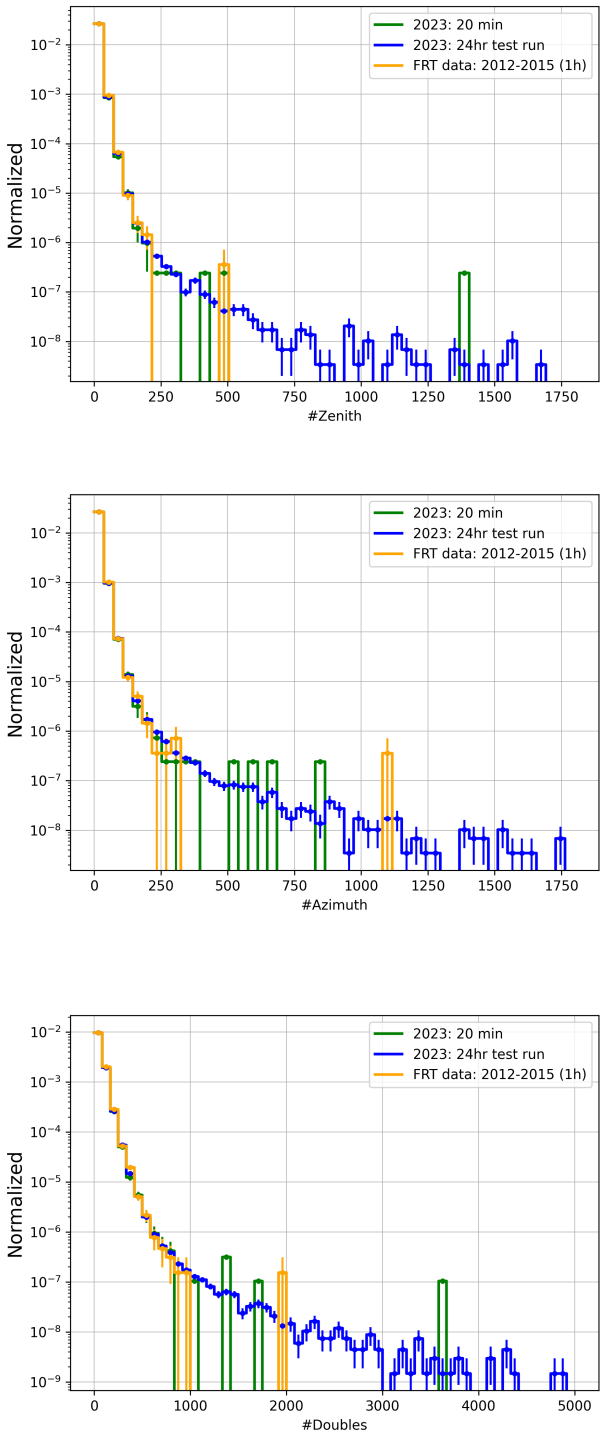

Figure B.3: Trigger variables for test run data
The number of maximum zenith (top) and azimuth (middle) bin counts and Doubles (bottom) is shown. These are shown for FRT data (orange), the 20 min test run in 2023 (green), and the 24hr test run in 2023 (blue).

C

Appendix C

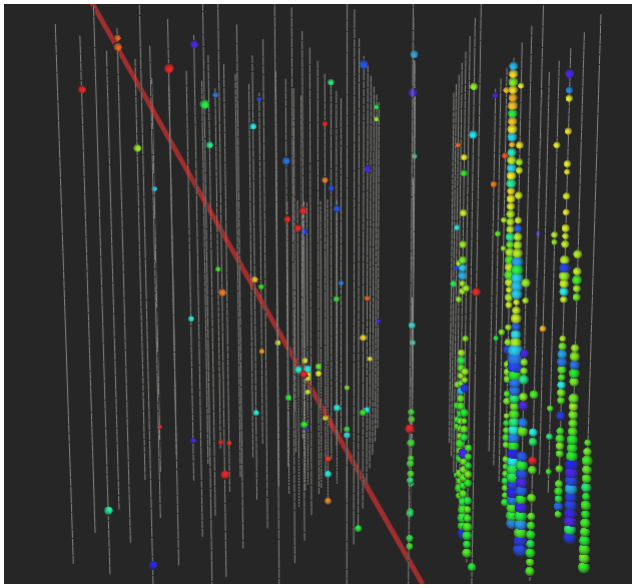

Figure C.1: FCP mixed with a high energy muon
Simulation of a FCP with mixed with a high energy muon. The muon does not satisfy the NChannel vs. #HLC cut in IC and has a FPT trigger. The FCP is only triggered by the FCT. The red line indicates the simulated direction of the FCP.

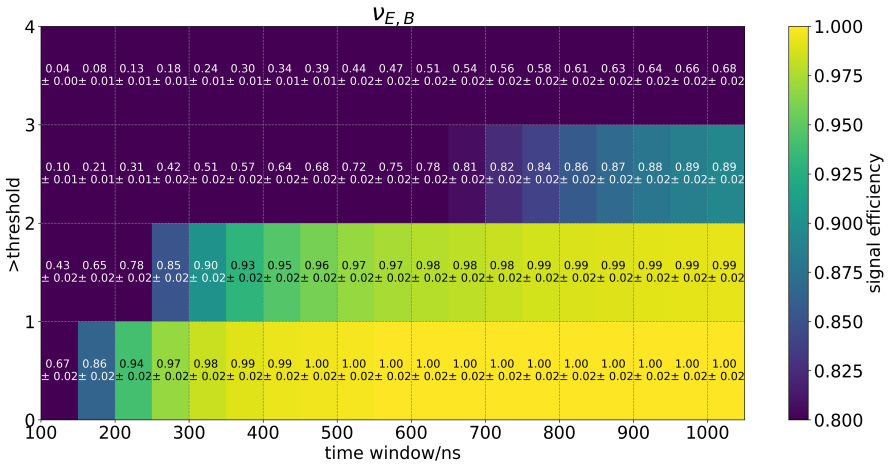

Figure C.2: Only FPT branch ν_e signal efficiency after NoiseEngine

The $\nu_{e,B}$ signal efficiency of the only FPT branch for different combinations of the time window length and threshold parameters of the NoiseEngine module.

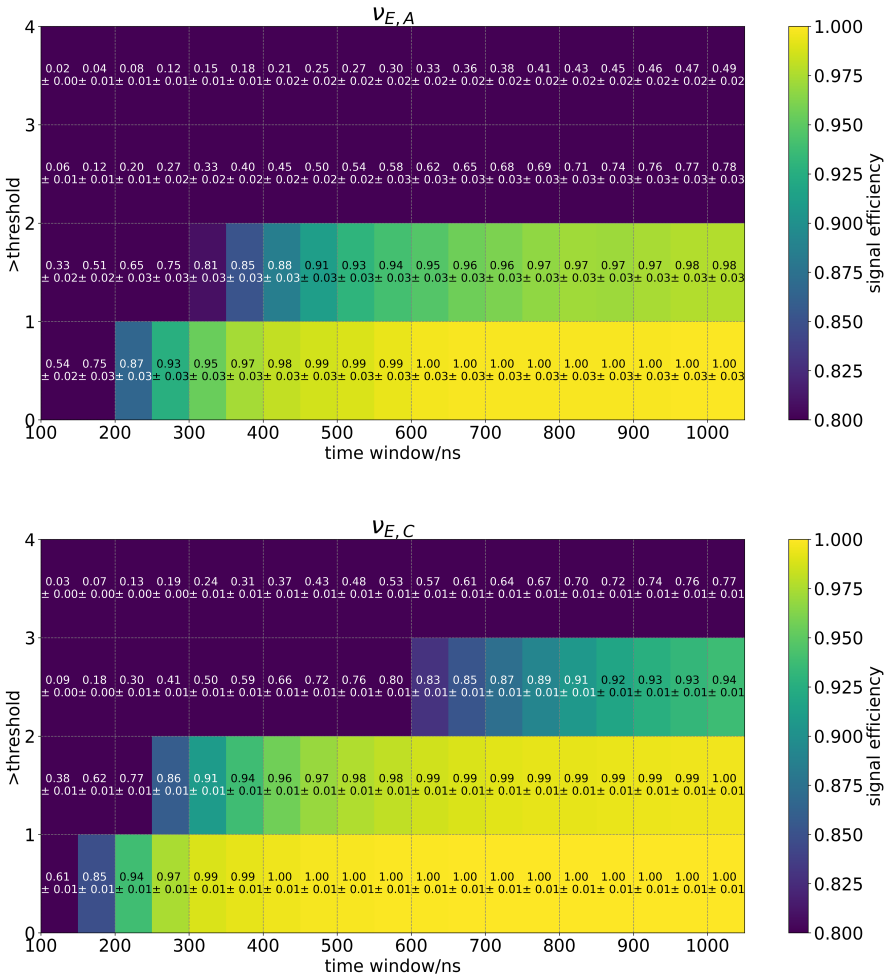

Figure C.3: FPT branch $\nu_{e,A}$ and $\nu_{e,C}$ signal efficiency after NoiseEngine

The ν_e (top) and $\nu_{e,C}$ (bottom) signal efficiencies for different combinations of the time window length and threshold parameters of the NoiseEngine module.

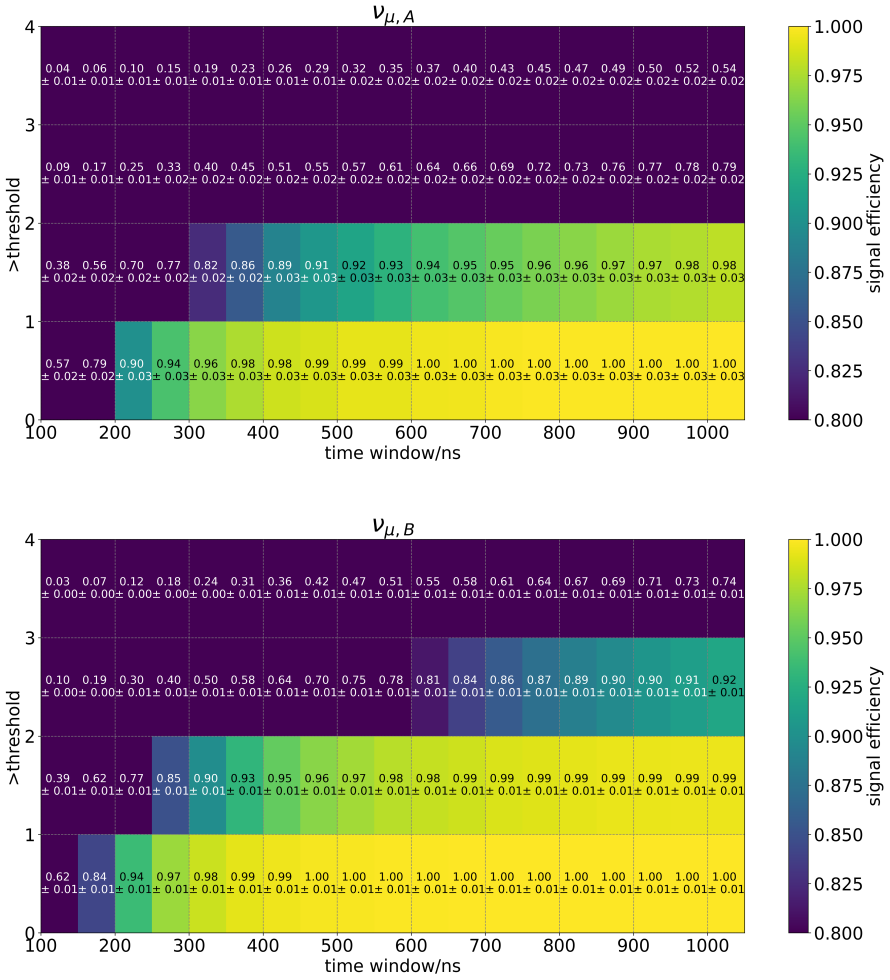

Figure C.4: FPT branch $\nu_{\mu,A}$ and $\nu_{\mu,B}$signal efficiency after NoiseEngine

The $\nu_{\mu,A}$ (top) and $\nu_{\mu,C}$ (bottom) signal efficiencies for different combinations of the time window length and threshold parameters of the NoiseEngine module.

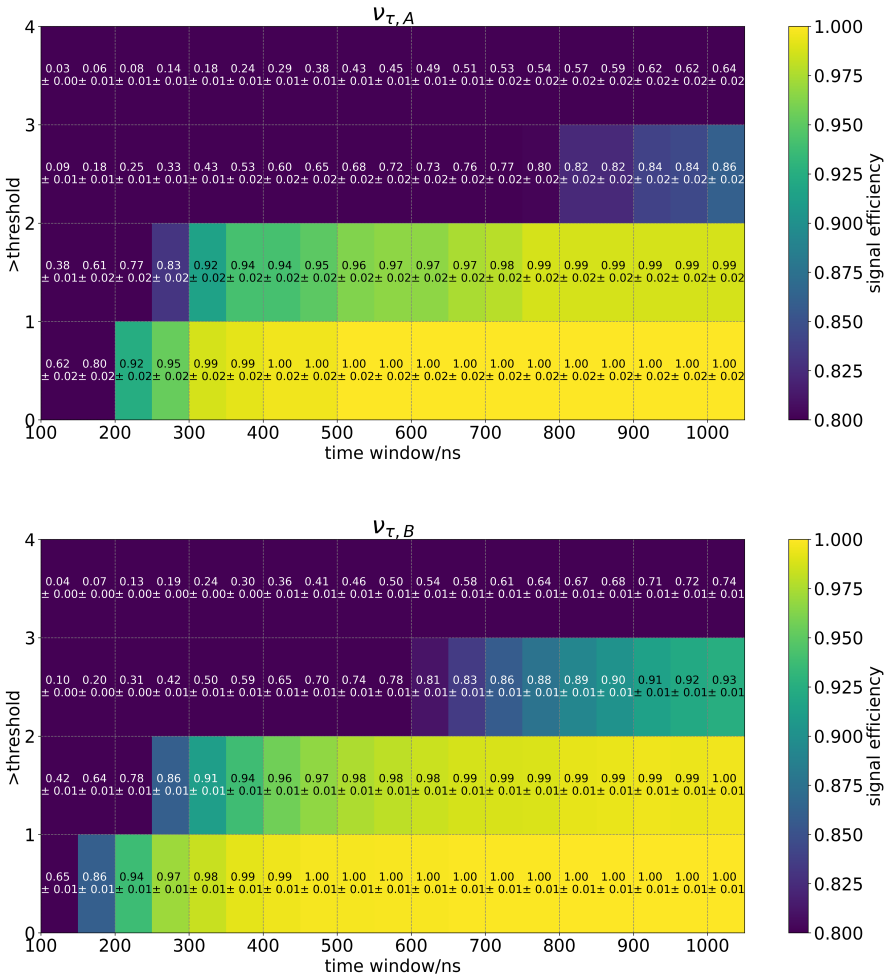

Figure C.5: FPT branch $\nu_{\tau,A}$ and $\nu_{\tau,B}$signal efficiency after NoiseEngine
The $\nu_{\tau,A}$ (top) and $\nu_{\tau,B}$ signal efficiencies for different combinations of the time window length and threshold parameters of the NoiseEngine module.

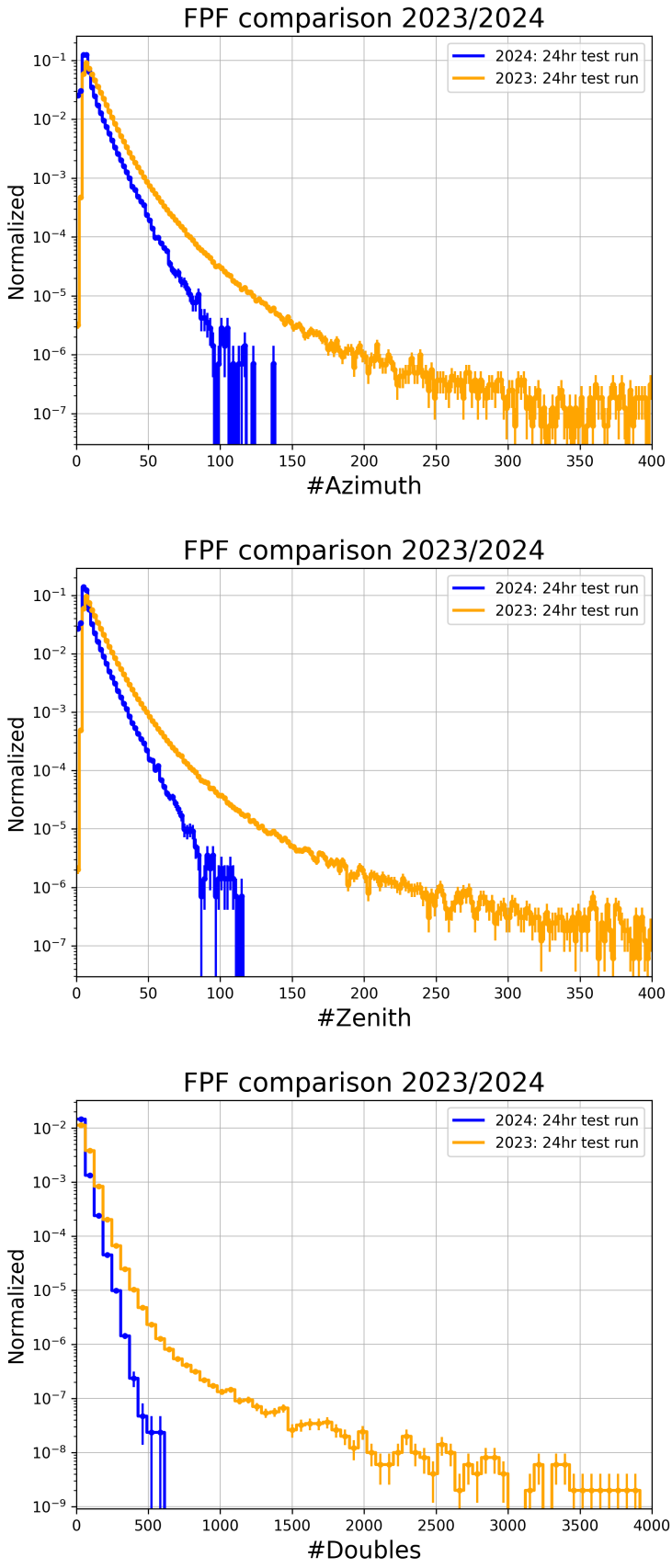

Figure C.6: FPF zenith and azimuth distributions for test data
The maximum bin count value for the azimuth (top) and zenith (middle) histograms and the number of Doubles (bottom) for the 2024 test run data (blue) and the 2023 test run (orange). This effectively compares the FPT trigger variables before (blue) and after applying the FPF (orange).

D

Appendix D

The effective area is shown for the isotropic scenario, including the only FPT and only FPF contributions.

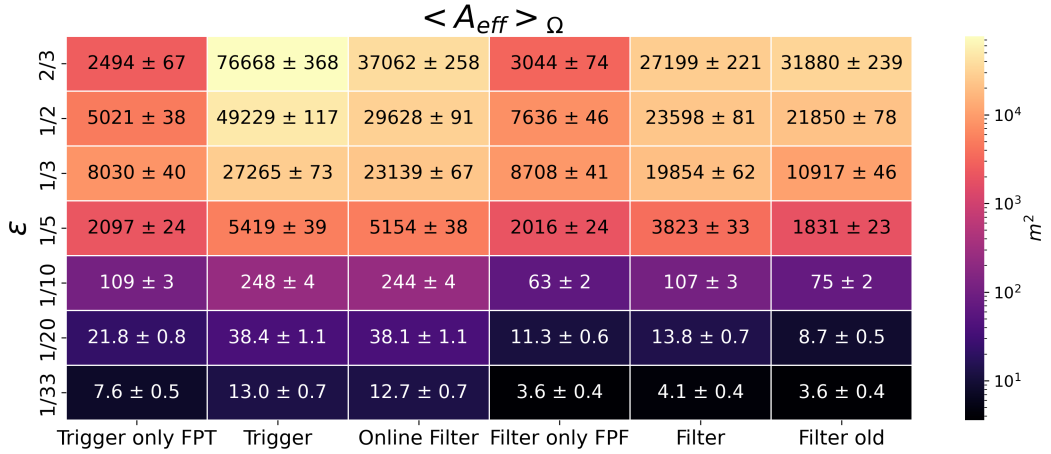

Figure D.1: Averaged effective area for the isotropic scenario including the FPF
The effective area for the isotropic scenario is shown for different processing stages and different ε. Here the only FPT and only FPF values are included. For $\varepsilon = 2/3, 1/2, 1/3$ the spectral index is 2 and for the others 2.7.

For the new filters the FPF has an important impact in the isotropic scenario. This can be seen by the comparison of the new filters with and without the FPF. The effective area is

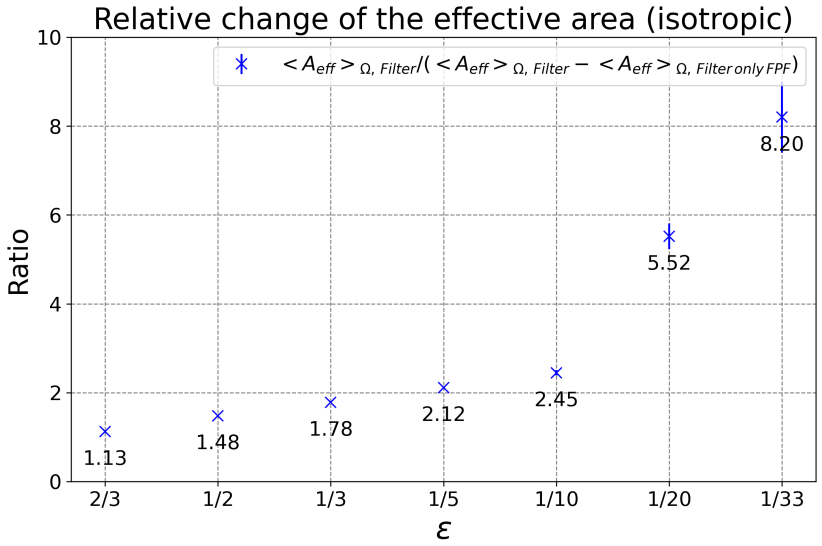

Figure D.2: Relative improvements for the isotropic scenario by the FPF
Relative improvement for the new filter level by the FPF in the isotropic scenario.

shown for the non-isotropic scenario, including the only FPT and only FPF contributions.

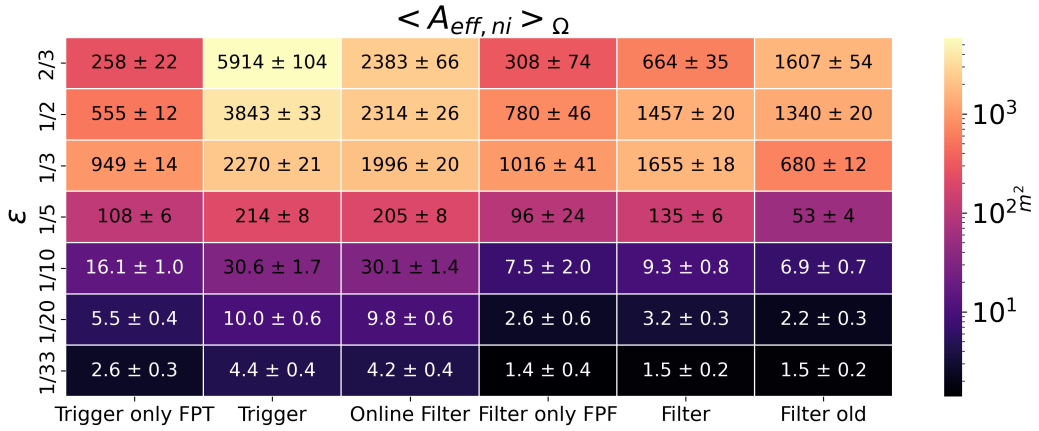

Figure D.3: Averaged effective area for the non-isotropic scenario including the FPF
The effective area for the non-isotropic scenario is shown for different processing stages and different ε. Here the only FPT and only FPF valus are included. For $\varepsilon = 2/3, 1/2, 1/3$ the spectral index is 2 and for the others 2.7.

For the new filters the FPF has an important impact in the non-isotropic scenario. This can be seen by the comparison of the new filters with and without the FPF.

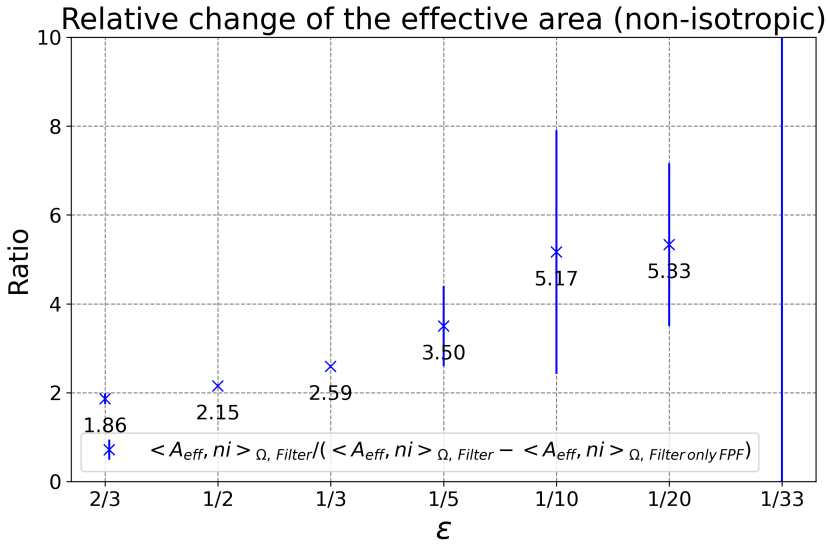

Figure D.4: Relative improvement for the non-isotropic scenario by the FPF
Relative improvement for the new filter level by the FPF in the non-isotropic scenario.

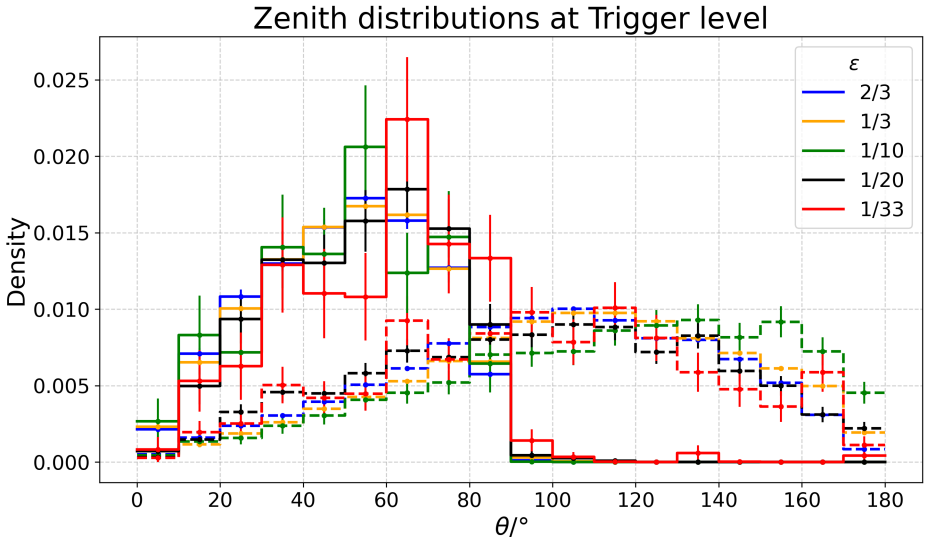

Figure D.5: Effect of the survival probability on the zenith distribution
Zenith angle for different ε. The lines represent the zenith distributions at trigger level for the isotropic scenario (dashed) and the reweighed events (solid). Events are reweighed according to the survival probability. For $\varepsilon = 2/3, 1/3$ the spectral index is 2 and for the others 2.7.

The zenith dependent effective area and event rate expectations for an ε of 1/3. It results in a sufficient amount of events with multiple years of data. Note that for this simulation sample the spectral index is 2 and thus deviates from those of the heavy mesons.

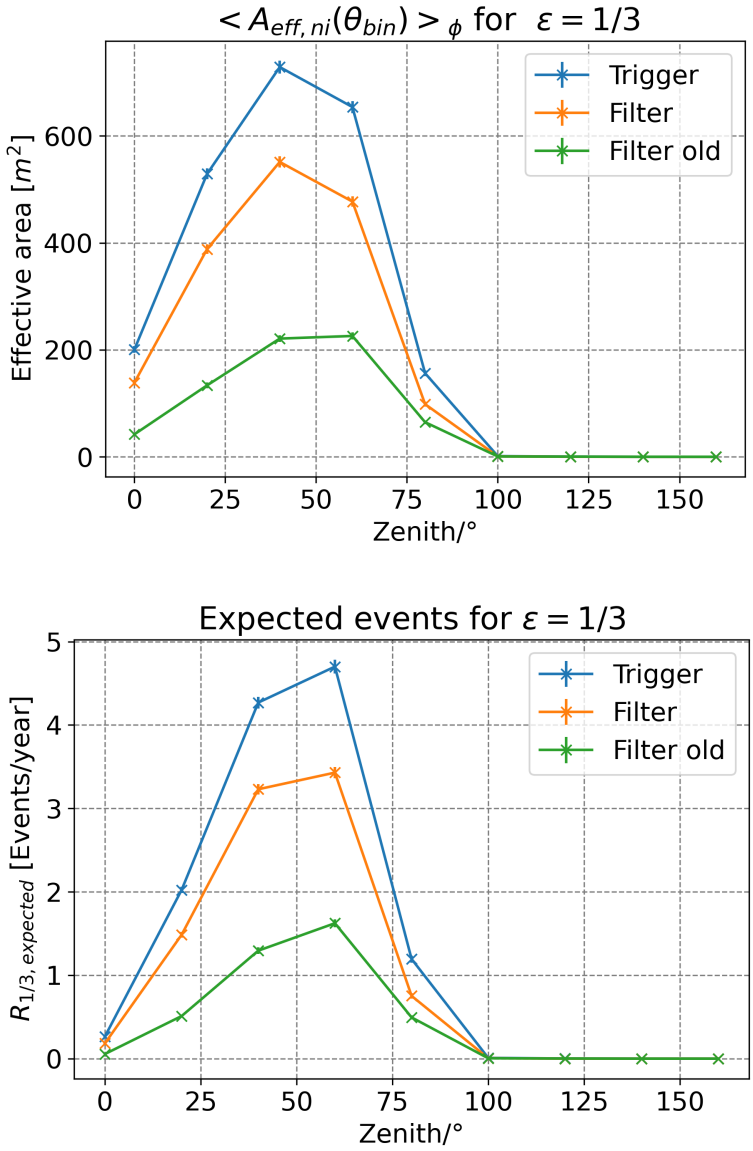

Figure D.6: Effective area and expected event rate for ε of 1/3
The zenith dependent effective area (top) and calculated expected event rates (bottom) are shown. The trigger level (blue) and old (green) and new filtering level (orange) are compared.

The zenith dependent effective area and event rate expectations for an ε of 1/10. It results in a too low number of expected events.

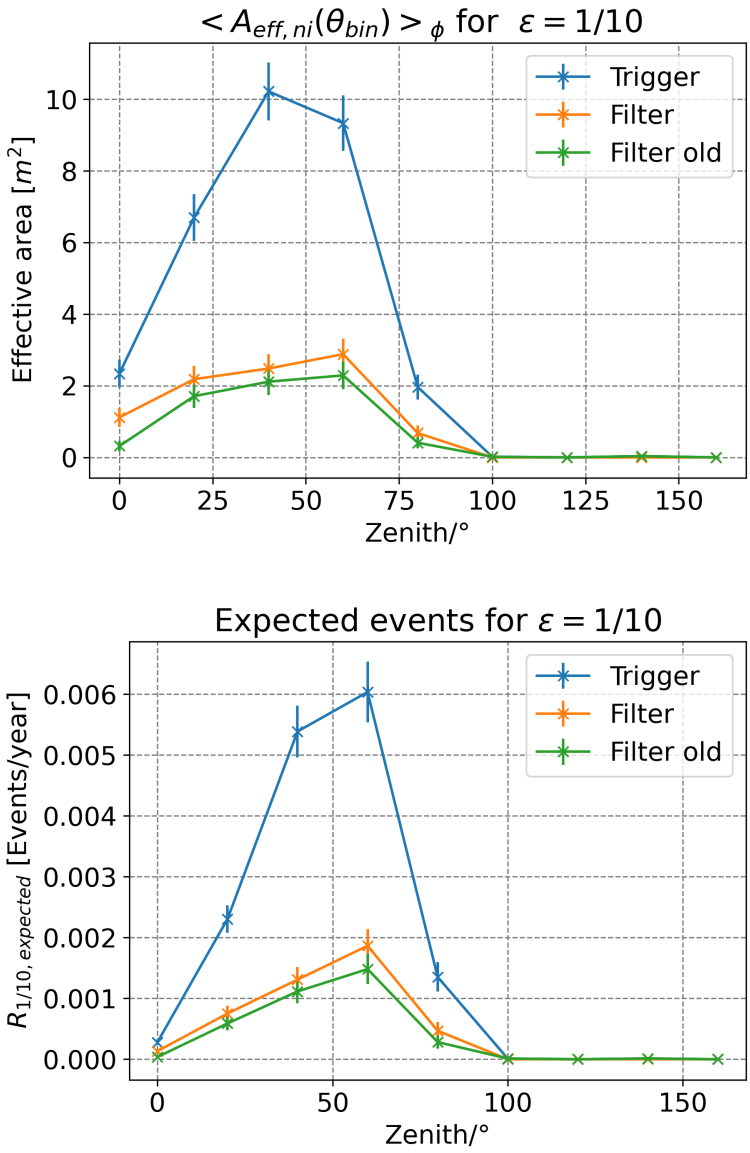

Figure D.7: Effective area and expected event rate for ε of 1/10
The zenith dependent effective area (top) and calculated expected event rates (bottom) are shown. The trigger level (blue) and old (green) and new filtering level (orange) are compared.

Bibliography

[1] Wikimedia Wikimedia Commons. *Standard Model of Elementary Particles.* Sept. 17, 2019. URL: https://commons.wikimedia.org/wiki/File:Standard_Model_of_Elementary_Particles.svg (visited on 10/25/2024).

[2] C. N. Yang and R. L. Mills. "Conservation of Isotopic Spin and Isotopic Gauge Invariance." In: *Physical Review* 96.1 (Oct. 1, 1954). Publisher: American Physical Society, pp. 191–195. DOI: 10.1103/PhysRev.96.191.

[3] Steven Weinberg. "A Model of Leptons." In: *Physical Review Letters* 19.21 (Nov. 20, 1967). Publisher: American Physical Society, pp. 1264–1266. DOI: 10.1103/PhysRevLett.19.1264.

[4] Michael E. Peskin and Daniel V. Schroeder. *An Introduction to quantum field theory*. Reading, USA: Addison-Wesley, 1995. ISBN: 978-0-201-50397-5. DOI: 10.1201/9780429503559.

[5] Matthew D. Schwartz. *Quantum Field Theory and the Standard Model*. Higher Education from Cambridge University Press. ISBN: 9781108985031 Publisher: Cambridge University Press. Dec. 15, 2013. DOI: 10.1017/9781139540940. URL: https://www.cambridge.org/highereducation/books/quantum-field-theory-and-the-standard-model/A4CD66B998F2C696DCC75B984A7D5799 (visited on 10/29/2024).

[6] F. Halzen and D. Martin. *Quarks and Leptons: An Introductory Course in Modern Particle Physics*. New York, USA: John Wiley & Sons Ltd., 1984. ISBN: 978-0-471-88741-6.

[7] Peter W. Higgs. “Broken Symmetries and the Masses of Gauge Bosons.” In: *Physical Review Letters* 13.16 (Oct. 19, 1964). Publisher: American Physical Society, pp. 508–509. DOI: 10.1103/PhysRevLett.13.508.

[8] F. Englert and R. Brout. “Broken Symmetry and the Mass of Gauge Vector Mesons.” In: *Physical Review Letters* 13.9 (Aug. 31, 1964). Publisher: American Physical Society, pp. 321–323. DOI: 10.1103/PhysRevLett.13.321.

[9] G. S. Guralnik et al. “Global Conservation Laws and Massless Particles.” In: *Physical Review Letters* 13.20 (Nov. 16, 1964). Publisher: American Physical Society, pp. 585–587. DOI: 10.1103/PhysRevLett.13.585.

[10] G. Aad et al. “Observation of a new particle in the search for the Standard Model Higgs boson with the ATLAS detector at the LHC.” In: *Physics Letters B* 716.1 (Sept. 17, 2012), pp. 1–29. ISSN: 0370-2693. DOI: 10.1016/j.physletb.2012.08.020.

[11] Roman Jackiw. “Physical Formulations: Elementary Particle Theory. Relativistic Groups and Analyticity. Proceedings of the eighth Nobel Symposium, Aspenäsgården, Lerum, Sweden, May 1968. Nils Svartholm, Ed. Interscience (Wiley), New York, and Almqvist and Wiksell, Stockholm, 1969. 400 pp., illus. $31.75.” In: *Science* 168.3936 (June 5, 1970). Publisher: American Association for the Advancement of Science, pp. 1196–1197. DOI: 10.1126/science.168.3936.1196.b.

[12] Sheldon L. Glashow. “Partial-symmetries of weak interactions.” In: *Nuclear Physics* 22.4 (Feb. 1, 1961), pp. 579–588. ISSN: 0029-5582. DOI: 10.1016/0029-5582(61)90469-2.

[13] SNO Collaboration et al. “Direct Evidence for Neutrino Flavor Transformation from Neutral-Current Interactions in the Sudbury Neutrino Observatory.” In: *Physical Review Letters* 89.1 (June 13, 2002). Publisher: American Physical Society, p. 011301. DOI: 10.1103/PhysRevLett.89.011301.

[14] Andrei D. Sakharov. “Violation of CP invariance, C asymmetry, and baryon asymmetry of the universe.” In: *Soviet Physics Uspekhi* 34.5 (May 31, 1991). Publisher: IOP Publishing, p. 392. ISSN: 0038-5670. DOI: 10.1070/PU1991v034n05ABEH002497.

[15] Particle Data Group et al. “Review of Particle Physics.” In: *Progress of Theoretical and Experimental Physics* 2022.8 (Aug. 8, 2022), p. 083C01. ISSN: 2050-3911. DOI: 10.1093/ptep/ptac097.

[16] Edvige Corbelli and Paolo Salucci. *The Extended Rotation Curve and the Dark Matter Halo of M33*. Sept. 15, 1999. DOI: 10.48550/arXiv.astro-ph/9909252. arXiv: astro-ph/9909252.

[17] Douglas Clowe et al. *A direct empirical proof of the existence of dark matter*. Aug. 19, 2006. DOI: 10.48550/arXiv.astro-ph/0608407. arXiv: astro-ph/0608407.

[18] Priyamvada Natarajan et al. *Mapping substructure in the HST Frontier Fields cluster lenses and in cosmological simulations*. Feb. 26, 2017. DOI: 10.48550/arXiv.1702.04348. arXiv: 1702.04348.

[19] Planck Collaboration et al. “Planck 2018 results. VI. Cosmological parameters.” In: *Astronomy & Astrophysics* 641 (Sept. 2020), A6. ISSN: 0004-6361, 1432-0746. DOI: 10.1051/0004-6361/201833910. arXiv: 1807.06209[astro-ph].

[20] Arttu Rajantie. “Introduction to Magnetic Monopoles.” In: *Contemporary Physics* 53.3 (May 2012), pp. 195–211. ISSN: 0010-7514, 1366-5812. DOI: 10.1080/00107514.2012.685693. arXiv: 1204.3077.

[21] Joseph Polchinski. “Monopoles, Duality, and String Theory.” In: *International Journal of Modern Physics A* 19 (Feb. 2004), pp. 145–154. ISSN: 0217-751X, 1793-656X. DOI: 10.1142/S0217751X0401866X. arXiv: hep-th/0304042.

[22] G. ’t Hooft. “Magnetic monopoles in unified gauge theories.” In: *Nuclear Physics B* 79.2 (Sept. 18, 1974), pp. 276–284. ISSN: 0550-3213. DOI: 10.1016/0550-3213(74)90486-6.

[23] Vasiliki A. Mitsou. “Searches for Magnetic Monopoles: A Review.” In: *Proceedings* 13.1 (2019). Number: 1 Publisher: Multidisciplinary Digital Publishing Institute, p. 10. ISSN: 2504-3900. DOI: 10.3390/proceedings2019013010.

[24] Howard Georgi and S. L. Glashow. “Unity of All Elementary-Particle Forces.” In: *Physical Review Letters* 32.8 (Feb. 25, 1974), pp. 438–441. ISSN: 0031-9007. DOI: 10.1103/PhysRevLett.32.438.

[25] Super-Kamiokande Collaboration et al. “Search for proton decay via $p \to e^+\pi^0$ and $p \to \mu^+\pi^0$ in 0.31 megaton·years exposure of the Super-Kamiokande water Cherenkov detector.” In: *Physical Review D* 95.1 (Jan. 6, 2017). Publisher: American Physical Society, p. 012004. DOI: 10.1103/PhysRevD.95.012004.

[26] S. M. Barr et al. “Fractional Charges, Monopoles, and Peculiar Photons.” In: *Physical Review Letters* 50.5 (Jan. 31, 1983). Publisher: American Physical Society, pp. 317–320. DOI: 10.1103/PhysRevLett.50.317.

[27] P. H. Frampton and T. W. Kephart. “Fractionally Charged Particles as Evidence for Supersymmetry.” In: *Physical Review Letters* 49.18 (Nov. 1, 1982). Publisher: American Physical Society, pp. 1310–1313. DOI: 10.1103/PhysRevLett.49.1310.

[28] Hong-Wei Yu. “SU(8) GUT models with a stable proton, $n-n$ oscillations, fractional charges, and low mass monopoles.” In: *Physics Letters B* 142.1 (July 12, 1984), pp. 42–46. ISSN: 0370-2693. DOI: 10.1016/0370-2693(84)91132-8.

[29] Katsuji Yamamoto. “Fractionally charged leptons in the SO(14) GUT.” In: *Physics Letters B* 120.1 (Jan. 6, 1983), pp. 157–160. ISSN: 0370-2693. DOI: 10.1016/0370-2693(83)90643-3.

[30] Fang-xiao Dong et al. “Fractional charges, monopoles and peculiar photons in SO(18) GUT models.” In: *Physics Letters B* 129.6 (Oct. 6, 1983), pp. 405–410. ISSN: 0370-2693. DOI: 10.1016/0370-2693(83)90129-6.

[31] Martin L. Perl et al. “Searches for Fractionally Charged Particles.” In: *Annual Review of Nuclear and Particle Science* 59 (Volume 59, 2009 Nov. 23, 2009). Publisher: Annual Reviews, pp. 47–65. ISSN: 0163-8998, 1545-4134. DOI: 10.1146/annurev-nucl-121908-122035.

[32] Ward Van Driessche. “Search for particles with anomalous charge in the IceCube detector.” Dissertation. Ghent University, 2019.

[33] J. J. Aubert et al. “A search for free quarks in deep inelastic muon scattering.” In: *Physics Letters B* 133.6 (Dec. 29, 1983), pp. 461–466. ISSN: 0370-2693. DOI: 10.1016/0370-2693(83)90828-6.

[34] The OPAL collaboration. “Search for Stable and Long-Lived Massive Charged Particles in e+e- Collisions at sqrt(s) = 183-209 GeV.” In: *Physics Letters B* 572.1 (Oct. 2003), pp. 8–20. ISSN: 03702693. DOI: 10.1016/S0370-2693(03)00639-7. arXiv: hep-ex/0305031.

[35] C. M. S. Collaboration. *Searches for long-lived charged particles in pp collisions at sqrt(s) = 7 and 8 TeV*. July 29, 2013. DOI: 10.48550/arXiv.1305.0491. arXiv: 1305.0491.

[36] C. M. S. Collaboration. *Search for fractionally charged particles in proton-proton collisions at $\sqrt{s}$ = 13 TeV*. Feb. 15, 2024. arXiv: 2402.09932[hep-ex].

[37] M. Aglietta et al. “Search for fractionally charged particles in the Mont Blanc LSD scintillation detector.” In: *Astroparticle Physics* 2.1 (Feb. 1, 1994), pp. 29–34. ISSN: 0927-6505. DOI: 10.1016/0927-6505(94)90015-9.

[38] MACRO Collaboration et al. “Search for lightly ionizing particles with the MACRO detector.” In: *Physical Review D* 62.5 (Aug. 4, 2000). Publisher: American Physical Society, p. 052003. DOI: 10.1103/PhysRevD.62.052003.

[39] M. Mori et al. “Search for fractionally charged particles in Kamiokande II.” In: *Physical Review D* 43.9 (May 1, 1991). Publisher: American Physical Society, pp. 2843–2846. DOI: 10.1103/PhysRevD.43.2843.

[40] The MACRO Collaboration. *Final Search for Lightly Ionizing Particles with the MACRO detector*. Feb. 2, 2004. arXiv: hep-ex/0402006.

[41] Carlos A. Argüelles et al. “Millicharged Particles from the Heavens: Single- and Multiple-Scattering Signatures.” In: *Journal of High Energy Physics* 2021.11 (Nov. 2021), p. 99. ISSN: 1029-8479. DOI: 10.1007/JHEP11(2021)099. arXiv: 2104.13924[hep-ex,physics:hep-ph].

[42] Mingxuan Du et al. *Millicharged particles from proton bremsstrahlung in the atmosphere*. Nov. 21, 2022. arXiv: 2211.11469[astro-ph,physics:hep-ex, physics:hep-ph].

[43] Han Wu et al. *Searching for heavy millicharged particles from the atmosphere*. June 5, 2024. arXiv: 2406.01668.

[44] Bob Holdom. "Two U(1)'s and ε charge shifts." In: *Physics Letters B* 166.2 (Jan. 9, 1986), pp. 196–198. ISSN: 0370-2693. DOI: 10.1016/0370-2693(86)91377-8.

[45] Keith R. Dienes et al. *Kinetic Mixing and the Supersymmetric Gauge Hierarchy*. Mar. 30, 1997. DOI: 10.48550/arXiv.hep-ph/9610479. arXiv: hep-ph/9610479.

[46] P. A. Čerenkov. "Visible Radiation Produced by Electrons Moving in a Medium with Velocities Exceeding that of Light." In: *Physical Review* 52.4 (Aug. 15, 1937), pp. 378–379. ISSN: 0031-899X. DOI: 10.1103/PhysRev.52.378.

[47] K. Nakamura and (Particle Data Group). "Review of Particle Physics." In: *Journal of Physics G: Nuclear and Particle Physics* 37.7 (July 2010), p. 075021. ISSN: 0954-3899. DOI: 10.1088/0954-3899/37/7A/075021.

[48] I. Frank and Ig. Tamm. "Coherent Visible Radiation of Fast Electrons Passing Through Matter." In: *Selected Papers*. Berlin, Heidelberg: Springer, 1991, pp. 109–114. ISBN: 978-3-642-74626-0. DOI: 10.1007/978-3-642-74626-0_2.

[49] Merlin Schaufel. "Implementing Hybrid Detection by Combining a Compact Air-Cherenkov Telescope with the HAWC Gamma-Ray Observatory." Master thesis. RWTH Aachen, 2017.

[50] Dmitry Chirkin and Wolfgang Rhode. "Propagating leptons through matter with Muon Monte Carlo (MMC)." In: *arXiv:hep-ph/0407075* (July 7, 2004). arXiv: hep-ph/0407075.

[51] S. Kelner et al. "About Cross-section for High-energy Muon Bremsstrahlung." In: (Jan. 1, 1995).

[52] J. -H. Koehne et al. “PROPOSAL: A tool for propagation of charged leptons.” In: *Computer Physics Communications* 184.9 (Sept. 1, 2013), pp. 2070–2090. ISSN: 0010-4655. DOI: 10.1016/j.cpc.2013.04.001.

[53] Mario Dunsch et al. “Recent improvements for the lepton propagator PROPOSAL.” In: *Computer Physics Communications* 242 (Sept. 1, 2019), pp. 132–144. ISSN: 0010-4655. DOI: 10.1016/j.cpc.2019.03.021.

[54] Maurizio Spurio. *Particles and Astrophysics. A Multi-Messenger Approach*. Astronomy and Astrophysics Library. Springer, 2015. ISBN: 978-3-319-34539-0. DOI: 10.1007/978-3-319-08051-2.

[55] A. Haungs et al. “The KASCADE Cosmic-ray Data Centre KCDC: granting open access to astroparticle physics research data.” In: *The European Physical Journal C* 78.9 (Sept. 17, 2018), p. 741. ISSN: 1434-6052. DOI: 10.1140/epjc/s10052-018-6221-2.

[56] The Pierre Auger Collaboration. “Measurement of the energy spectrum of cosmic rays above 10^18 eV using the Pierre Auger Observatory.” In: *Physics Letters B* 685.4 (Mar. 2010), pp. 239–246. ISSN: 03702693. DOI: 10.1016/j.physletb.2010.02.013. arXiv: 1002.1975[astro-ph].

[57] Carmelo Evoli. *The Cosmic-Ray Energy Spectrum*. Publisher: Zenodo. Dec. 1, 2020. DOI: 10.5281/zenodo.7948212.

[58] M. G. Aartsen et al. “The IceCube Neutrino Observatory: Instrumentation and Online Systems.” In: *Journal of Instrumentation* 12.3 (Mar. 14, 2017). ISSN: 1748-0221. DOI: 10.1088/1748-0221/12/03/P03012.

[59] ICECUBE COLLABORATION. “Evidence for High-Energy Extraterrestrial Neutrinos at the IceCube Detector.” In: *Science* 342.6161 (Nov. 22, 2013). Publisher: American Association for the Advancement of Science, p. 1242856. DOI: 10.1126/science.1242856.

[60] ICECUBE COLLABORATION et al. “Neutrino emission from the direction of the blazar TXS 0506+056 prior to the IceCube-170922A alert.” In: *Science* 361.6398

(July 13, 2018). Publisher: American Association for the Advancement of Science, pp. 147–151. DOI: 10.1126/science.aat2890.

[61] ICECUBE COLLABORATION et al. "Evidence for neutrino emission from the nearby active galaxy NGC 1068." In: *Science* 378.6619 (Nov. 4, 2022). Publisher: American Association for the Advancement of Science, pp. 538–543. DOI: 10.1126/science.abg3395.

[62] ICECUBE COLLABORATION. "Observation of high-energy neutrinos from the Galactic plane." In: *Science* 380.6652 (June 30, 2023). Publisher: American Association for the Advancement of Science, pp. 1338–1343. DOI: 10.1126/science.adc9818.

[63] P. B. Price et al. "Age vs depth of glacial ice at South Pole." In: *Geophysical Research Letters* 27.14 (2000), pp. 2129–2132. ISSN: 1944-8007. DOI: 10.1029/2000GL011351.

[64] M. Ackermann et al. "Optical properties of deep glacial ice at the South Pole." In: *Journal of Geophysical Research: Atmospheres* 111 (D13 2006). ISSN: 2156-2202. DOI: 10.1029/2005JD006687.

[65] Rezvan Abbasi et al. "Low energy event reconstruction in IceCube DeepCore." In: *The European Physical Journal C* 82 (Sept. 9, 2022). DOI: 10.1140/epjc/s10052-022-10721-2.

[66] Rasha Abbasi et al. *In-situ estimation of ice crystal properties at the South Pole using LED calibration data from the IceCube Neutrino Observatory*. Oct. 21, 2022. DOI: 10.5194/tc-2022-174.

[67] R. Abbasi et al. "The design and performance of IceCube DeepCore." In: *Astroparticle Physics* 35.10 (May 1, 2012), pp. 615–624. ISSN: 0927-6505. DOI: 10.1016/j.astropartphys.2012.01.004.

[68] The IceCube Collaboration. *Digital Optical Module*. IceCube. Jan. 11, 2021. URL: https://icecube.wisc.edu/gallery/diagrams/ (visited on 10/26/2024).

[69] Michael James Larson et al. "Simulation and Identification of Non-Poissonian Noise Triggers in the IceCube Neutrino Detector." In: *University of Albama* (2013).

[70] D. Freiherr Heereman von Zuydtwyck. “HitSpooling: An Improvement for the Supernova Neutrino Detection System in IceCube.” PhD thesis. Université Libre de Bruxelles, 2015.

[71] T. Bendfelt. *Trigger System Performance Study*. IceCube Events Management (Indico). 2023. URL: https://events.icecube.wisc.edu/event/164/contributions/9155/ (visited on 11/04/2024).

[72] T. Anderson et al. *Design and performance of the multi-PMT optical module for IceCube Upgrade*. July 23, 2021. arXiv: 2107.11383[astro-ph].

[73] R. Abbasi et al. “D-Egg: a Dual PMT Optical Module for IceCube.” In: *Journal of Instrumentation* 18.4 (Apr. 1, 2023), P04014. ISSN: 1748-0221. DOI: 10.1088/1748-0221/18/04/P04014. arXiv: 2212.14526[astro-ph].

[74] Serap Tilav et al. *Atmospheric Variations as observed by IceCube*. Jan. 7, 2010. arXiv: 1001.0776[astro-ph].

[75] M. Wallraff. “Design, Implementation and Test of a New Feature Extractor for the IceCube Neutrino Observatory.” Diploma thesis. RWTH Aachen, 2010.

[76] Dmitry Chirkin. “Photon tracking with GPUs in IceCube.” In: *Nuclear Instruments and Methods in Physics Research Section A: Accelerators, Spectrometers, Detectors and Associated Equipment*. VLVνT 11, Erlangen, Germany, 12 - 14 October, 2011 725 (Oct. 11, 2013), pp. 141–143. ISSN: 0168-9002. DOI: 10.1016/j.nima.2012.11.170.

[77] Thorsten Glüsenkamp. “On the Detection of Subrelativistic Magnetic Monopoles With the IceCube Neutrino Observatory.” Diploma thesis. RWTH Aachen, 2010.

[78] N. J. Schmeißer. “Faint non-standard model particles in IceCube.” Master thesis. Bergische Universität Wuppertal, 2024.

[79] Jakob Böttcher. “Background Estimation for Sub-Relativistic Particles in IceCube.” Master thesis. RWTH Aachen, 2019.

[80] S. Zierke. “Verbesserung von Rekonstruktions- und Datenselektions-Methoden für die Messung subrelativistischer magnetischer Monopole mit IceCube.” Master thesis. RWTH Aachen, 2013.

[81] G. de Wasseige. “Solar Flare Neutrinos in the Multi-Messenger Era: Flux Calculations and a Search with the IceCube Neutrino Observatory.” PhD thesis. VUB, 2018.

[82] Aya Ishihara. *The IceCube Upgrade – Design and Science Goals*. Aug. 26, 2019. arXiv: 1908.09441[astro-ph].

Acknowledgements

This thesis would not have been possible without the support of many people.

I want to deeply thank Prof. Dr. Klaus Helbing who gave me the chance to work in this fascinating field of research. You let me explore the topic freely, while providing invaluable advice and support during crucial moments.

I am also grateful to the IceCube collaboration, particularly to those who contributed to bringing the trigger into production. Additionally, I want to thank the exceptional astroparticle physics group in Wuppertal, especially Dr. Anna Pollmann and Dr. Alexander Sandrock, who provided me indispensable feedback and advice throughout the years.

Lastly, I want to thank my friends and family for their enduring support, especially to my wonderful wife and adorable child, my constant sources of motivation. Without you, this journey would have been impossible.